University of California
Los Angeles

Positron Production by X-rays Emitted from Betatron Motion in a Plasma Wiggler

A dissertation submitted in partial satisfaction
of the requirements for the degree
Doctor of Philosophy in Electrical Engineering

by

Devon Kryle Johnson

2006

© Copyright by
Devon Kryle Johnson
2006

The dissertation of Devon Kryle Johnson is approved.

Warren B. Mori

Francis F. Chen

George Morales

Chandrashekhar J. Joshi, Committee Chair

University of California, Los Angeles

2006

Table of Contents

1 Introduction 1

2 Synchrotron Radiation due to Betatron Motion and Plasma Formation 4

2.1 Electron Betatron Motion in a Plasma Wiggler 4

2.2 Spontaneous Radiation Emission from Electron Betatron Motion . . . 7

2.3 The Saddle-Point Method for Betatron Spectrum Calculation 11

2.4 Total Radiated Power from an Electron Undergoing Betatron Oscillations 16

2.5 Plasma Formation by Field Ionization 20

2.5.1 Field Ionization 20

2.5.2 Estimation of Electrons in the Ion Column 24

3 Pair Production Theory 26

3.1 Schrödinger Equation 26

3.2 The Dirac Equation 27

3.3 Hole Theory 30

3.4 Positron Production 31

3.5 Pair Production Cross-Section and Screening 33

4 Experimental Setup and Diagnostics 39

4.1 Plasma Wakefield Experimental Diagnostics 39

4.1.1 X-ray Spectrometer 40

4.1.2 Optical Transition Radiation 42

4.1.3 Coherent Transition Radiation 43

4.1.4 Focusing Optics 45

4.1.5 Lithium (Li) Oven for Plasma Medium 46
4.1.6 Cherenkov Diagnostic 49
4.2 Positron Experimental Diagnostics 51
4.2.1 Photon Collimators 51
4.2.2 Target 53
4.2.3 Positron Spectrometer Magnet 53
4.2.4 Noise Reduction 56
4.2.5 Signal Detection and Calibration 56

5 Determination of Beam Parameters from Simulations and Experiment 58
5.1 Fraction of the Beam Electrons in the Ion Column 59
5.2 Wakefield Losses 66
5.3 Plasma Beam Focusing 67

6 Results 77
6.1 Introduction 77
6.2 Positron and Electron Measured Spectra Agreement 78
6.3 Comparison of Measured Positron Spectrum with Theory 79
6.4 Density Vs. Yield 85
6.5 Positron Spectral Variation 88
6.6 Yield vs. CTR Signal 89
6.7 Waist vs. Yield 94
6.8 Conclusion of Results 99

7 Future Work 101
7.1 Source Optimization 101
7.1.1 Charge in the Gaussian Beam 102

7.1.2 Bunch Length 103

7.1.3 Plasma Density 106

7.1.4 Scaling Laws 109

7.1.5 Experimental Observation of this Accelerating Effect 109

7.2 A Possible Source Design 110

7.3 Conclusion 117

8 Conclusion 118

References 122

List of Figures

2.1 Schematic of Coordinate Axis for Lienard-Wiechert Potentials (Equation (2.18)) 7

2.2 Axial radiation spectrum ($\theta = 0$) for one electron with $r_\beta = 10\mu m$, $n_{pe} = 1 \times 10^{14} cm^{-3}$ and $N_\beta = 4$; (a) The harmonic structure of the entire spectrum. (b) The 11th harmonic showing the expected dependence of the full-width at half maximum (FWHM $= \Delta\omega_n$), $\Delta\omega_n/\omega_o = 1/N_\beta = .25$ for our case. 10

2.3 Schematic of the Saddle-Point Method. $\vec{p}_1$ will not contribute to the spectrum at the far-field position determined by $\vec{k}$ since $\vec{k} \cdot \vec{p}_1$ is small. However, $\vec{p}_2$ will have a substantial contribution to the far-field at that point since $\vec{k} \cdot \vec{p}_2$ is large. 12

2.4 Solutions to equation (2.57) using the Saddle-Point method. This assumes an electron with $E = 28.5GeV$, $r = 10\mu m$ and $n_{pe} = 1 \times 10^{17} cm^{-3}$. The units of $d^2W/d\omega d\Omega$ are $eV \cdot s/\Omega$. (a) At $\phi = 0$ and $\theta = 0$. (b) At $\phi = 90$ with increasing θ. 15

2.5 Line-outs of the total radiated energy in the far-field using the Saddle-Point method. This assumes an electron with $E = 28.5GeV$, $r = 10\mu m$ and $n_{pe} = 1 \times 10^{17} cm^{-3}$. The units of $dW/d\Omega$ are eV/Ω; (a) Parallel to particle oscillation plane, x-axis ($\phi = 0$), $\theta_x = K/\gamma$ dependence. (b) Perpendicular to particle oscillation plane, y-axis ($\phi = 90$), $\theta_y = 1/\gamma$ dependence. 16

2.6 Contour plots of the total radiated energy in the far-field using the Saddle-Point method. This assumes an electron with $E = 28.5GeV$, $r = 10\mu m$ and $n_{pe} = 1 \times 10^{17} cm^{-3}$. The units of $dW/d\Omega$ are eV/Ω; (a) 3-D. (b) 2-D projection of (a). 17

2.7 Total radiated energy for a azimuthally symmetric "ring of electrons" with $\sigma_r = 10\mu m$. The units of $dW/d\Omega$ are eV/Ω; (a) 3-D contour plot with log scale for the amplitude ($dW/d\Omega$). (b) Line out at $\phi = 0$ for increasing θ with log scale for the amplitude ($dW/d\Omega$). 20

2.8 (a) A contour plot showing the electric field distribution within a Gaussian electron beam with $N_b = 1.2 \times 10^{10}$ electrons, $\sigma_z = 29\mu m$, and $\sigma_r = 11\mu m$. (b) Plot of the radial lineout of the electric field for $z = 0$, $z = \sigma_z$, and $z = 2\sigma_z$. The black horizontal line defines $E_{beam} = 6GV/m$. (c) The fractional percentage of ionized Li atoms after 10, 20 and 30 fs. 22

2.9 (a) An example longitudinal beam profile in the experiment (described later) for a Coherent Transition Radiation (CTR) detector signal of 150. The longitudinal sigma of the peak region is $\sigma_z = 29\mu m$ and the beam $\sigma_r = 11\mu m$. The right vertical axis plots the fractional ionization for E_{peak} (black line) and $.5E_{peak}$ (red line) for the given longitudinal beam location. (b) Computed charge in the ion column by integrating the charge $10\mu m$ downstream of the full ionization of the 50 percent of the peak electric field contour. 24

3.1 Schematic of pair production geometry [1]. 32

3.2 Vector diagram of momentum balance for pair production [1]. 33

3.3 Function $c(\mu)$ for the Bethe-Heitler cross-section [2]. 35

3.4 The Bethe-Heitler cross-section from Equations (3.38)-(3.41) for Tungsten. X-axis is the ratio of the positron energy, E_+, to the incident photon energy, k. (a) Y-axis is the Bethe-Heitler cross section, $d\sigma/dE_+$, multiplied by the incident photon energy, k, in MeV. (b) Y-axis is only the Bethe-Heitler cross-section, $d\sigma/dE_+$. 36

3.5 The Bethe-Heitler cross-section from Equations (3.38)-(3.41) for Tungsten. Y-axis is the Bethe-Heitler cross section, $d\sigma/dE_+$. X-axis is the positron energy, E_+ for (a) 5-10 MeV and (b) 5-30 MeV. 37

4.1 E-164/E-164X/E-167 Experimental Schematic 40

4.2 (a) Schematic of the X-ray Chicane. (b) Example of a data image from the X-ray Spectrometer. 41

4.3 Schematic of the OTR setup 43

4.4 Schematic of the CTR setup 44

4.5 Plot showing the correlation of the pyro signal to the peak current of the bunch as determined by the X-ray spectrometer [3]. 45

4.6 Schematic of the focusing setup of the FFTB at IP0, immediately upstream of the plasma entrance. [4]. 46

4.7 Schematic of the Li vapor oven. [3]. 48

4.8 Plot showing the measured Li neutral density profile and the curve fit to the measured profile. 49

4.9 (a) Plot showing the calibration of energy/pixel on the Cherenkov diagnostic. (b) Example false-color image on the Cherenkov after the electron beam traversed through the plasma. 50

4.10 Schematic of the positron experimental setup. 52

4.11 (a) Upstream phosphor image of 8mm collimated photon beam before collision with the positron target. A hole was cut in the TRIMAX phosphor to allow a He-Ne laser to propagate through for experimental alignment. (b) X-Lineout of the image. (c) Y-lineout of the image. 52

4.12 (a) Schematic of dipole imaging system for positron spectroscopy. Detectors are located in the Vertical Focal Plane of the positrons to maximize signal. The red x's plot the energy image plane. The 11 degree pole face rotation creates extra vertical focusing. (b) Photo of the region. 54

4.13 Magnet Calibration of B-field (T) versus current (A) with the semicircular pole pieces and a pole gap of 24.4mm. 55

5.1 QuickPIC simulation of a Gaussian electron beam with $N_b = 1.2 \times 10^{10}$ electrons, $\sigma_r = 11\mu m$, $\sigma_z = 22.5\mu m$ and $n_{pe} = 1 \times 10^{17} cm^{-3}$. (a) Portion of the Li vapor that is ionized. (b) The plasma electron density within the ionized portion of the vapor. (c) The longitudinal electric field (E_z) for four different beam radii. (d) Focusing force (E_r) at six longitudinal positions. All radial units are normalized by σ_r, and all longitudinal units are normalized by σ_z. 59

5.2 Example Cherenkov Image. (a) "Plasma out" case. (b) "Plasma in" case without median filter. (c) Same as (b) with a 4 by 4 median filter. Also, contains a vertical lineout of the beam. The horizontal axis (x) for all plots is the width of the beam. The vertical axis (energy) for all plots gives the energy spectrum of the beam. All images are taken with $n_{pe} = 1 \times 10^{17} cm^{-3}$. 64

5.3 Example Cherenkov Analysis. Each point represents a pyro bin of 50. (a) Average electron energy loss in Lower region (wakefield+radiation) versus CTR bin. Also, plotted is the peak energy loss for all electrons versus CTR bin. The black line specifies the lower edge of the Cherenkov diagnostic. (b) Head and Lower charge versus CTR bin. All images are taken with $n_{pe} = 1 \times 10^{17} cm^{-3}$. 66

5.4 Plot showing vacuum and plasma propagation for both X and Y planes as the beam waist is moved. (a) X-plane propagation with the waist set at $z = -10cm$ leading to a $\sigma_x = 8\mu m$ radiating spot size. (b) X-plane propagation with the waist set at $z = -6cm$ leading to a $\sigma_x = 6\mu m$ radiating spot size. (c) X-plane propagation with the waist set at $z = -3cm$ leading to a $\sigma_y = 5\mu m$ radiating spot size. (d) Y-plane propagation with the waist set at $z = -3cm$ leading to a $\sigma_y = 4\mu m$ radiating spot size. All plots assume a peak density $n_{pe} = 1 \times 10^{17} cm^{-3}$. 69

5.5 QuickPIC simulation showing the beam size within the peak density region of the plasma for the (a) Y-plane and (b) X-plane. Each plot shows the periodicity of the beam envelope by plotting two distributions after $\lambda_\beta/2$. The simulation assumed a Gaussian electron beam with $N_b = 1.2 \times 10^{10}$ electrons, $\sigma_r = 11\mu m$, $\sigma_z = 22.5\mu m$ and $n_{pe} = 1 \times 10^{17} cm^{-3}$. 70

5.6 Plot showing the radiated energy versus radius for (a) Y-plane ($\theta = 0^o$ and 180^o) and (b) X-plane ($\theta = 90^o$ and 270^o). Each has three cases plotted; case 1 $[(\sigma_x, \sigma_y) = (5,5)\mu m]$, case 2 $[(\sigma_x, \sigma_y) = (6,5)\mu m]$, and case 3 $[(\sigma_x, \sigma_y) = (8,5)\mu m]$. (c) Positron yield for all three cases. The last two are divided by 1.14 and 1.35 respectively to show the similarity of the spectral "shapes". The relative yield for case 1 = 1.0, case 2 = 1.13, and case 3 = 1.37. All cases assumes a peak density $n_{pe} = 1 \times 10^{17} cm^{-3}$. 71

5.7 Plots showing the plasma electron density from a QuickPIC simulation with an experimental ramped neutral density profile, (positions and neutral density are defined relative to those in Figure 5.4), with a Gaussian electron beam with $N_b = 1.2 \times 10^{10}$ electrons, $\sigma_r = 11\mu m$, $\sigma_z = 22.5\mu m$ and $n_{pe} = 1 \times 10^{17} cm^{-3}$. The plasma electron distribution at (a) $z = -5.0 cm$ and $n_{pe} = .01 n_{p,max}$, (b) $z = -1.3$ and $n_{pe} = .29 n_{p,max}$, (c) $z = 0.0 cm$ and $n_{pe} = .5 n_{p,max}$, and (d) $z = 4.1 cm$ and $n_{pe} = n_{p,max}$. All cases assumes a peak density $n_{p,max} = 1 \times 10^{17} cm^{-3}$. 74

5.8 Plot showing the beam density from a QuickPIC simulation (same as Figure 5.7) with an experimental ramped neutral density profile, (positions and neutral density are defined relative to those in Figure 5.4), with a Gaussian electron beam with $N_b = 1.2 \times 10^{10}$ electrons, $\sigma_r = 11\mu m$, $\sigma_z = 22.5\mu m$ and $n_{pe} = 1 \times 10^{17} cm^{-3}$. The plasma electron distribution at (a) $z = -5.0cm$ and $n_{pe} = .01 n_{p,max}$, (b) $z = -1.3$ and $n_{pe} = .29 n_{p,max}$, (c) $z = 0.0cm$ and $n_{pe} = .5 n_{p,max}$, and (d) $z = 4.0cm$ and $n_{pe} = n_{p,max}$. All cases assumes a peak density $n_{p,max} = 1 \times 10^{17} cm^{-3}$. 75

6.1 (a) Measured spectra for both electrons (e^-) and positrons (e^+) for $n_{pe} = 1 \times 10^{17} cm^{-3}$ with averages taken in 1 MeV energy bins. (b) CTR energy ($1/\sigma_z$) for the electrons and positrons for the same 1 MeV energy bins. 79

6.2 (a) Li Oven Full-width at Half Maximum (FWHM) for the oen cases discussed in this chapter. 80

6.3 Plot showing vacuum and plasma propagation for both X and Y planes as the beam waist is moved. (a) X-plane propagation with the waist set at $z = -5cm$ leading to a $\sigma_x = 4\mu m$ radiating spot size. (b) X-plane propagation with the waist set at $z = 0cm$ leading to a $\sigma_x = 4\mu m$ radiating spot size. This assumes $n_{p,max} = 1 \times 10^{17} cm^{-3}$. . . 81

6.4 (a)(c)(e) The average energy with plasma out (blue +), the average energy loss in the Lower region with plasma (blue circle), and the peak energy loss with plasma defined by the 1 percent charge contour (red x) versus CTR signal for $n_{pe} = 10$, 6.36, and $3.33 \times 10^{16} cm^{-3}$, respectively. (b)(d)(f) The charge in region (1) of the bunch (Head) and in region (3), the radiating portion of the bunch (Lower) versus the CTR signal for $n_{pe} = 10$, 6.36, and $3.33 \times 10^{16} cm^{-3}$, respectively.. 82

6.5 (a) Measured and calculated positron spectrum for $n_{pe} = 1{\times}10^{17} cm^{-3}$. (b) Measured and calculated positron spectrum for $n_{pe} = 6.4 \times 10^{16} cm^{-3}$. (c) Measured and calculated positron spectrum for $n_{pe} = 3.3 \times 10^{16} cm^{-3}$. (d) Integrated positron yield in the 4-20 MeV energy range versus the plasma density. The "variation" in the calculated value corresponds to the yield obtained using an rms electron beam spot size of $\pm 0.5 \mu m$ compared to its value used for the point marked by the red "x" (calculation). 84

6.6 (a)(c)(e) QuickPIC simulation showing the plasma electron density contours for the $n_{pe} = 10$, 6.36, and $3.33 \times 10^{16} cm^{-3}$ cases, respectively. (b)(d)(f) Lineout of the QuickPIC simulation at various longitudinal locations showing the focusing force as a function of radius. The pure ion column case is also plotted for reference (green dotted line). The simulation assumes a gaussian beam with $N_b = 1.2 \times 10^{10}$ electrons, $\sigma_{i:x,y} = 11 \mu m$ and $\sigma_z = 22.5 \mu m$. 87

6.7 Measured and calculated positron spectrum for $n_{pe} = 3.33{\times}10^{16} cm^{-3}$. (a) Curve fit with $\sigma_{i:x,y} = 7.5 \mu m$. (b) Curve fit with $\sigma_{i:x,y} = 8.0 \mu m$. (c) Curve fit with $\sigma_{i:x,y} = 8.5 \mu m$. All other parameters are equal between the cases. 89

6.8 (a) The charge in region (1) (Head) of the bunch, and in region (3) the radiating portion of the bunch (Lower) versus the CTR signal. (b) The integrated positron yield in the 4-20 MeV energy range versus CTR signal for $n_{pe} = 1 \times 10^{17} cm^{-3}$. Also plotted is the average beam energy loss for the radiating electrons within the 11cm plasma (wake+radiation). 91

6.9 Integrated positron yield in the 27-30 MeV energy range versus CTR signal for 3 different plasma lengths with $n_{pe} = 2.7 \times 10^{17} cm^{-3}$. Note that the CTR signal bins are different from those in figure 6.8. The data was taken with different experimental setups. 92

6.10 Plot of the experimentally measured charge in the ion column using the Cherenkov analysis versus X-waist locations of (a) -30 cm, (b) -15 cm, (c) the nominal 0 cm, (d) +15 cm and (e) +30 cm. The orange line denotes the average CTR energy for each run. (f) The measured integrated positron yield from 4-20 MeV for the five X-waist locations plotted in (a)-(e). 95

6.11 (a) Plot of the average beam energy without plasma (blue +) and the average energy loss with plasma for the 5 previously listed cases. All data was taken with $n_{p,max} = 6.4 \times 10^{16} cm^{-3}$. (b) A QuickPIC simulation with $n_{pe} = 6.4 \times 10^{16} cm^{-3}$,$N_b = 1.2 \times 10^{10}$, $\sigma_y = 11 \mu m$ and $\sigma_z = 22.5 \mu m$, showing the change of the longitudinal wakefield as σ_x of the beam is varied (i.e. as the X-waist is changed). 96

7.1 Plots the longitudinal and transverse fields in a field ionized plasma plasma of density $n_{pe} = 2 \times 10^{17} cm^{-3}$ from a $\sigma_r = 15 \mu m$ and $\sigma_z = 22.5 \mu m$ electron beam with three different N_b values. (a) Longitudinal fields for $N_b = 1 \times 10^{10}$. (b) Transverse fields for $N_b = 1 \times 10^{10}$. (c) Longitudinal fields for $N_b = 2 \times 10^{10}$. (d) Transverse fields for $N_b = 2 \times 10^{10}$. (e) Longitudinal fields for $N_b = 4 \times 10^{10}$. (f) Transverse fields for $N_b = 4 \times 10^{10}$. 104

7.2 Plots the longitudinal and transverse fields in a field ionized plasma of density $n_{pe} = 2 \times 10^{17} cm^{-3}$ with a $N_b = 4 \times 10^{10}$ electron beam with $\sigma_r = 12 \mu m$ and three different σ_z values. (a) Longitudinal fields for $\sigma_z = 22.5$. (b) Transverse fields for $\sigma_z = 22.5$. (c) Longitudinal fields for $\sigma_z = 27.5$. (d) Transverse fields for $\sigma_z = 27.5$. (e) Longitudinal fields for $\sigma_z = 32.5$. (f) Transverse fields for $\sigma_z = 32.5$. 105

7.3 Plots the longitudinal and transverse fields in a field ionized with four different n_{pe} values with a $N_b = 4 \times 10^{10}$ electron beam with $\sigma_r = 12\mu m$ and $\sigma_z = 35\mu m$ values. (a) Longitudinal fields for $n_{pe} = 1 \times 10^{17} cm^{-3}$. (b) Transverse fields for $n_{pe} = 1 \times 10^{17} cm^{-3}$. (c) Longitudinal fields for $n_{pe} = 1.5 \times 10^{17} cm^{-3}$. (d) Transverse fields for $n_{pe} = 1.5 \times 10^{17} cm^{-3}$. (e) Longitudinal fields for $n_{pe} = 2 \times 10^{17} cm^{-3}$. (f) Transverse fields for $n_{pe} = 2 \times 10^{17} cm^{-3}$. (g) Longitudinal fields for $n_{pe} = 3 \times 10^{17} cm^{-3}$. (h) Transverse fields for $n_{pe} = 3 \times 10^{17} cm^{-3}$. 107

7.4 Plots the (a) longitudinal fields, (b) transverse fields and (c) plasma density contours for a plasma with $n_{pe} = 1 \times 10^{17} cm^{-3}$ and an electron beam with $N_b = 1.2 \times 10^{10}$, $\sigma_r = 11\mu m$ and $\sigma_z = 22.5\mu m$. Plots the (a) longitudinal fields, (b) transverse fields and (c) plasma density contours for a plasma with $n_{pe} = 2 \times 10^{17} cm^{-3}$ and an electron beam with $N_b = 4 \times 10^{10}$, $\sigma_r = 12\mu m$ and $\sigma_z = 35\mu m$. 111

7.5 Schematic showing the proposed positron experiment. 112

7.6 (a) The positron spectrum from 1-50 MeV for the three different initial beam energy cases of $E_{beam} = 30$ GeV, $E_{beam} = 40$ GeV and $E_{beam} = 50$ GeV. (b) The number of positrons within each 10-MeV energy bin for the same three E_{beam} values. 114

7.7 (a) The positron spectrum from 1-50 MeV for the densities $n_{pe} = 2 \times 10^{17} cm^{-3}$ and $n_{pe} = 3 \times 10^{17} cm^{-3}$ with an initial beam energy cases of $E_{beam} = 50$ GeV. (b) The number of positrons within each 10-MeV energy bin for the same two densities. 116

LIST OF TABLES

2.1 The comparison of theoretical [5] and computed values for the total energy loss from one electron with $N_\beta = 4$. 19

3.1 The total integrated Bethe-Heitler Cross-Section for the k values plotted in Figures 3.4a and 3.4b. 36

3.2 The total integrated Bethe-Heitler Cross-Section (CS) for the k values plotted in Figures 3.5a and 3.5b. 38

6.1 This table lists the relative scaling for all different positron data cases. Magnet "on" assumes that 10 MeV positrons are being detected. The plasma density is $n_{pe} = 1 \times 10^{17} cm^{-3}$. 78

6.2 This table lists the pertinent simulation parameters for each of the cases in figure 6.5. 83

6.3 This table lists the plasma length, measured wakeloss, calculated e^+ yield, and the measured e^+ yield for the 175 CTR bin from figure 6.9. 93

6.4 This table lists the pertinent scaling values for the five X-waist positions discussed at $n_{pe} = 6.4 \times 10^{16} cm^{-3}$. The table lists the average CTR energy for each case. The wakeloss, N_{bi} and relative e^+ yield are quoted from this average CTR energy value for each case. 99

7.1 This table shows the scaling laws for various plasma parameters using a 3-D Gaussian electron beam in QuickPIC. 109

7.2 This table gives the values for the 5 bins in our positron source calculation with a 3-D Gaussian beam with $N_b = 4 \times 10^{10}$ electrons with $\sigma_r = 9 \mu m$, $\sigma_z = 35 \mu m$ and $n_{pe} = 3 \times 10^{17} cm^{-3}$. Negative wakeloss is an accelerating field. 113

7.3 This table gives the output from the simulation considering three different beam energies of $E_{beam} = 30$ GeV, $E_{beam} = 40$ GeV and $E_{beam} = 50$ GeV. All cases assume a 3-D Gaussian beam with $N_b = 4 \times 10^{10}$ electrons with $\sigma_r = 9\mu m$, $\sigma_z = 35\mu m$ and $n_{pe} = 3 \times 10^{17} cm^{-3}$. 115

7.4 This table gives the values for the 6 bins in our positron source calculation with a 3-D Gaussian beam with $N_b = 4 \times 10^{10}$ electrons with $\sigma_r = 9\mu m$, $\sigma_z = 35\mu m$ and $n_{pe} = 2 \times 10^{17} cm^{-3}$. Negative wakeloss is an accelerating field. 115

7.5 This table gives the output from the simulation for the densities $n_{pe} = 2 \times 10^{17} cm^{-3}$ and $n_{pe} = 3 \times 10^{17} cm^{-3}$ with an initial beam energy cases of $E_{beam} = 50$ GeV. All cases assume a 3-D Gaussian beam with $N_b = 4 \times 10^{10}$ electrons with $\sigma_r = 9\mu m$, $\sigma_z = 35\mu m$. 116

ACKNOWLEDGMENTS

Abstract of the Dissertation

Positron Production by X-rays Emitted from Betatron Motion in a Plasma Wiggler

by

Devon Kryle Johnson
Doctor of Philosophy in Electrical Engineering
University of California, Los Angeles, 2006
Professor Chandrashekhar J. Joshi, Chair

A new method for generating positrons has been proposed using betatron X-rays emitted by a high-K plasma wiggler. The plasma wiggler is an ion column produced by the head of the beam when the peak beam density exceeds the plasma density. The radial electric field of the beam blows out the plasma electrons, transversely, creating an ion column. The focusing electric field of the ion column, in turn, causes the beam electrons to execute betatron oscillations about the axis of the ion column. This betatron motion can give rise to synchrotron radiation in the 1-50 MeV range, if the beam energy and the plasma density are high enough. A significant amount of electron energy can be lost to radiated X-ray photons. These photons strike a thin ($.5X_o$), high-Z target and create e^+/e^- pairs. It is this new method of positron production by X-rays emitted from betatron motion in a plasma wiggler that is explored in this thesis.

The experiment was performed at the Stanford Linear Accelerator Center (SLAC) where a 28.5 GeV electron beam with $\sigma_r \approx 10\mu m$ and $\sigma_z \approx 25\mu m$ was propagated through a neutral Lithium vapor (Li). The radial electric field of the beam field ionized the Li vapor to form a plasma. Since the typical electron beam density of $4 \times 10^{17} cm^{-3}$ was greater than the plasma density of $3 \times 10^{17} cm^{-3}$, the plasma electrons were completely blown-out forming a pure ion column which led to electron betatron oscillations. The synchrotron radiation spectra from these oscillations had critical energies on the order of 50 MeV, ideal for positron production. The X-rays traveled 40m downstream of the plasma, were collimated and collided with a 1.7mm (.5X_o) Tungsten (W) target. The e^+/e^- pairs were imaged with a magnetic spectrometer and detected using silicon surface barrier detectors. Positrons were measured in the energy range of 2-30 MeV. The positron yield was measured as a function of plasma density, ion column length and electron beam pulse length. A computational model was written to match the experimental data with theory. The measured positron spectra are in excellent agreement with those expected from the calculated X-ray spectral yield from the plasma wiggler. After matching the model with the experimental results, the model was used to design a more efficient positron source, giving positron yields (per electron) comparable to those predicted from conventional low-K magnetic wigglers.

CHAPTER 1

Introduction

High energy physicists use electron-positron collisions to validate the predictions of various field theories. The positrons (e^+) needed for the collisions are currently produced by bombarding a high-Z, solid target that is several radiation lengths thick with a high energy electron beam [6]. The resulting interaction creates Bremsstrahlung photons which can interact with the atomic nuclei of the target producing electron-positron pairs. Positron beam requirements for future linear colliders suggest that this type of "thick-target", Bremsstrahlung e^+ source may fail from thermal stress since multiple scattering of the e^- beam deposits a large amount of energy into the target.

There have been several alternate designs for next generation positron sources. All of the methods considered produce positrons after colliding MeV X-rays with a thin, high-Z target. Here, "thick" and "thin" is relative to a radiation length. The source must also have a high conversion efficiency of drive beam energy to MeV X-ray photons since an average photon energy of 10-30 MeV is desired for efficient production of positrons [7]. Photo-production of positrons is seen as the solution for future linear colliders, but the methods for efficiently producing the X-rays are being studied. One proposal uses a helical undulator to produce polarized photons in the 5-10 MeV range [8]. Another proposed source uses Compton backscattering of an electron beam off a circularly polarized laser beam to produce polarized photons in this same energy range [9]. Both of these schemes are attractive because they can generate polarized positrons that are highly desirable for high energy particle physics. It has also been suggested that a Tungsten (W) crystal could be employed as an atomic undulator to produce MeV X-rays. In this scheme, the beam undulates within the crystal creating MeV photons near the entrance region and creates pairs towards the exit region of the crystal [10]. It is imperative that any new source overcomes the thermal stress and shock-wave issues associated with the aforementioned Bremsstrahlung source. In this thesis, we propose an alternative method of generating X-ray photons in the spectral range of interest to produce positrons and present results from an experiment conducted at the Stanford Linear Accelerator Center (SLAC) where a 28.5 GeV electron beam was used in a proof-of-principle of this scheme. Our scheme utilizes a plasma wiggler to wiggle the electrons via betatron oscillations. The plasma wiggler is an ion column produced by the beam itself. The radial electric field of the ion column causes an oscillating motion of the off-axis electrons (called betatron oscillations) as they propagate through the ion column. This wiggling motion creates a large broadband flux of MeV X-rays. These X-rays were collided with a thin, high-Z target to produce positrons.

In previous work, betatron motion of electrons in an ion column with a density $n_p \approx 10^{14} cm^{-3}$ was seen to generate $\sim 6 - 10$ keV X-rays in the direction of propagation of the electron beam [11]. Because of the low plasma density in that experiment, the effective wiggler strength was on the order of 1, comparable to modern magnetic undulator systems. However, for positron production, one needs X-rays in the 1-50 MeV energy range. To produce such high energy X-rays, the work here utilizes much higher plasma densities ($\sim 10^{17} cm^{-3}$), and effective wiggler strengths greater than 100. It is not practical to produce long uniform columns of such high density plasma using the UV photo-ionization technique of previous experiments. Therefore, the electric field of the electron beam was used to ionize the neutral gas. In order to exceed the field ionization threshold, the beam density must be high which in turn meant that the beam pulse length had to be on the order of $25 \mu m$ with a beam radius of roughly $10 \mu m$. Such short, dense electron beam pulses were available at the Stanford Linear Accelerator Center (SLAC), and the experimental work described in this thesis was carried out at the Final Focus Test Beam (FFTB) at SLAC.

The organization of the thesis is as follows. Chapter 2 will review the theory of synchrotron radiation in a plasma wiggler, and it will also discuss the theory of field ionization which is the method used in this experiment to produce the Li plasma source. Chapter 3 discusses positron production theory, and the cross-sections involved in pair production. Chapter 4 describes the experimental setup and has a brief theoretical explanation of each diagnostic. Chapter 5 explores the methods used to determine the electron beam parameters from the experiment. These beam parameters were used in a computational model designed for the purpose of matching many of our experimental results with theory. Chapter 6 will present the experimental results and, whenever possible, compare this data with calculations. Chapter 7 uses QuickPIC [12], a particle-in-cell simulation code for the study of beam-plasma interactions in tandem with the simulation model, to determine optimal beam and plasma parameters for a positron source. The results of this source design exercise will be presented. Chapter 8 presents the conclusion of the thesis.

CHAPTER 2

Synchrotron Radiation due to Betatron Motion and Plasma Formation

This chapter discusses the theory of synchrotron radiation for an off-axis electron propagating through a plasma. The derivation will be performed from first principles by inputting the betatron trajectories computed from the radial electric fields of a pure ion column into the Lienard-Wiechert potentials. Examples of the theoretical X-ray spectra and total radiated energy for an electron propagating through through this medium will be given. The theory of field ionization in a plasma will also be explored. The understanding of field ionization is critical for determining the number of electrons in the beam which actually reside within the ion column, and thus contribute to the X-ray spectrum. These two theories form the basis of a simulation package that has been written to compute the X-ray radiation from an electron beam propagating through a plasma. This result gives the necessary tools to match the measured positron spectra with theory.

2.1 Electron Betatron Motion in a Plasma Wiggler

The method for computing the radiated spectrum by an electron propagating through an ion column is outlined by Esarey et al. [13]. The following is from ref. [13] where the derivations are in CGS units. When an electron beam propagates through a plasma, there are two forces to consider that act on the beam. The transverse focusing force of the ion column and the focusing force on the beam due to self-fields. For an ultra-relativistic electron beam, the self-fields can be neglected if $n_p \gg n_b/\gamma^2$. This is known as the Budker condition [14] and is satisfied in our case. The evolution of the motion of a single electron in a plasma is governed by the relativistic Lorentz equation

$$\frac{d\vec{\mathbf{p}}}{dt} = \vec{\mathbf{F}}_{\mathbf{res}} = -e\nabla\Phi \tag{2.1}$$

where $\mathbf{F}_{\mathbf{res}}$ is the restoring force due to the transverse electric field of the plasma and Φ is the electrostatic potential of the focusing channel. Assuming the longitudinal electron trajectory to be in the z-direction and the betatron oscillation to reside in the r-direction, the relativistic Lorentz equations take the following form

$$\frac{1}{c}\frac{d(\gamma\beta_r)}{dt} = -\frac{\partial\hat{\Phi}}{\partial r}, \tag{2.2}$$

$$\frac{d(\gamma\beta_z)}{dt} = 0, \tag{2.3}$$

$$\frac{1}{c}\frac{d\gamma}{dt} = \beta_r\frac{\partial\hat{\Phi}}{\partial r} \tag{2.4}$$

where $\hat{\Phi} = e\Phi/mc^2$ is the normalized electrostatic potential and β_r and β_z are velocities normalized to c in their respectively directions. The electrostatic potential of the plasma is assumed to be

$$\hat{\Phi} = \hat{\Phi}_o(1 - r^2/r_o^2) \tag{2.5}$$

where $\hat{\Phi}_o$ and r_o are constants that will be determined below. The normalized radial electric field is $\hat{E}_r = -\partial\hat{\Phi}/\partial r = 2\hat{\Phi}_o r/r_o^2$.

To determine the radial beam evolution, we expand equation (2.2)

$$\frac{1}{c}\frac{(d\gamma\beta_r)}{dt} = \frac{1}{c}\left[\beta_r\frac{d\gamma}{dt} + \gamma\frac{d\beta_r}{dt}\right] = \frac{\partial\hat{\Phi}}{\partial r} = -\gamma k_\beta^2 r \tag{2.6}$$

where the betatron wavelength has been introduced as

$$k_\beta^2 = \frac{2\hat{\Phi}_o}{\gamma r_o^2} = -\frac{1}{\gamma}\frac{\partial\hat{\Phi}}{\partial r} \tag{2.7}$$

Substituting equation (2.4) and replacing the radial velocities with their spacial derivatives with respect to time, we get the following

$$\frac{d^2r}{dt^2} + w_b^2 r(1+\beta_r^2) = 0 \tag{2.8}$$

where $\omega_\beta = ck_\beta$. Assuming non-relativistic radial motion ($\beta_r \ll 1$), simple harmonic solutions result

$$r = \frac{K}{\gamma_{zo} k_\beta} sin(w_b t), \tag{2.9}$$

$$\beta_r = \frac{K}{\gamma_{zo}} cos(w_b t), \tag{2.10}$$

where

$$K = \gamma_{zo} k_\beta r_\beta \tag{2.11}$$

is the wiggler strength parameter.

Using the following initial conditions; $\gamma = \gamma_{zo}$, $\beta_r = 0$ and $\beta_z = \beta_{zo}$, we can solve for the axial motion. Integrating equation (2.4) with respect to time and solving for the constant with the initial condition $\gamma = \gamma_{zo}$ gives

$$\gamma = \gamma_{zo}\left(1 + \frac{K^2}{4\gamma_{zo}^2}\right) - \frac{K^2}{4\gamma_{zo}} cos(2w_b t) \tag{2.12}$$

This result is substituted into equation (2.3) and the equation is integrated with respect to time. Using the above initial condition, $\beta = \beta_{zo}$, we find

$$\beta_z = \frac{C_1}{\gamma} = \frac{\beta_{zo}}{1 + \frac{K^2}{4\gamma_{zo}^2}(1 - cos(2w_b t))} \tag{2.13}$$

Since $K^2/\gamma_{zo}^2 \ll 1$ for our parameters, the denominator can be expanded to yield

$$\beta_z = \beta_{zo}\left(1 - \frac{K^2}{4\gamma_{zo}^2}\right) + \beta_{zo}\left(\frac{K^2}{4\gamma_{zo}^2}\right) cos(2w_b t) \tag{2.14}$$

Integrating again with respect to time gives

$$z = z_o + \beta_{zo}\left(1 - \frac{K^2}{4\gamma_{zo}^2}\right)ct + \beta_{zo}\left(\frac{K^2}{8k_\beta \gamma_{zo}^2}\right) sin(2w_b t) \tag{2.15}$$

The constants $\hat{\Phi}_o$ and r_o^2 can be determined from the differential form of Gauss's Law

$$\nabla \cdot \vec{E} = -\nabla^2 \Phi = \frac{e}{\epsilon_o}(n_{pi} - n_{pe}) \tag{2.16}$$

or

$$\nabla^2 \hat{\Phi} = k_p^2 \left(\frac{n_{pe}}{n_{pi}} - 1\right) \tag{2.17}$$

where n_{pe} and n_{pi} are the plasma electron and ion densities, respectively. From $d\hat{E}_r/dr = 2\hat{\Phi}_o/r_o^2$, we see that $\hat{\Phi}_o/r_o^2 \leq k_p^2/4$. This value becomes a maximum in the

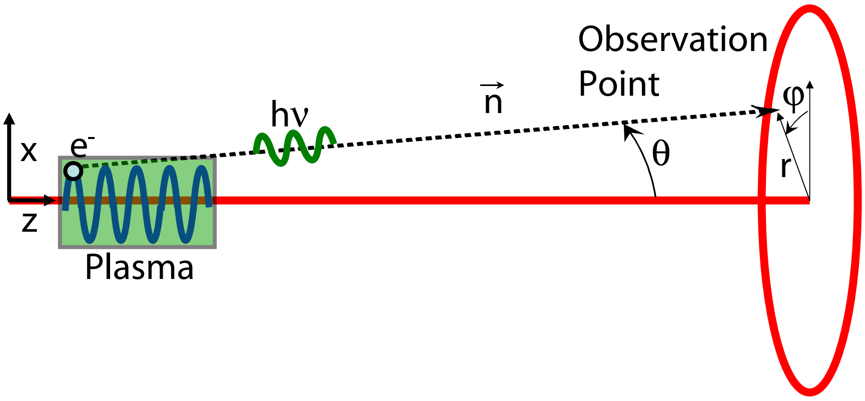

Figure 2.1: Schematic of Coordinate Axis for Lienard-Wiechert Potentials (Equation (2.18))

blowout regime where $n_{pe} = 0$, giving the familiar value of the betatron wavenumber, $k_\beta^2 = k_p^2/\sqrt{2\gamma}$. The physical implications of a quasi-blowout regime ($n_{pe} \neq 0$) will be addressed later.

2.2 Spontaneous Radiation Emission from Electron Betatron Motion

The synchrotron radiation emitted from an accelerated electron can be computed using the Lienard-Wiechert potentials [15]

$$\frac{d^2W}{d\omega d\Omega} = \frac{e^2\omega^2}{4\pi^2 c}\left|\int_{-\infty}^{\infty} \vec{\mathbf{n}} \times (\vec{\mathbf{n}} \times \vec{\beta}) e^{i\omega(t-\vec{\mathbf{n}}\cdot\vec{\mathbf{r}}(t)/c)} dt\right|^2 \tag{2.18}$$

This equation gives the energy radiated (W) per unit frequency (ω) per unit solid angle (Ω) for all times (t). $\vec{\mathbf{n}}$ is the unit vector pointing in the direction of observation downstream. The coordinate axes of the equation are illustrated in figure 2.1.

We now introduce spherical coordinates (r,ϕ,θ) making it convenient to calculate the individual photon polarizations, I_ϕ and I_θ. The spherical unit vectors are[1]

$$\hat{\mathbf{e}}_r = sin\theta cos\phi \hat{\mathbf{e}}_x + sin\theta sin\phi \hat{\mathbf{e}}_y + cos\theta \hat{\mathbf{e}}_z \tag{2.19}$$

$$\hat{\mathbf{e}}_\theta = cos\theta cos\phi \hat{\mathbf{e}}_x + cos\theta sin\phi \hat{\mathbf{e}}_y - sin\theta \hat{\mathbf{e}}_z \tag{2.20}$$

$$\hat{\mathbf{e}}_\phi = -sin\phi \hat{\mathbf{e}}_x + cos\phi \hat{\mathbf{e}}_y \tag{2.21}$$

---

[1] This assumes $x = rsin\theta cos\phi$, $y = rsin\theta sin\phi$, and $z = rcos\theta$

Defining $\hat{\mathbf{e}}_r = \hat{\mathbf{n}}$ and substituting equations (2.19), (2.20), and (2.21) into the Lienard-Wiechert potentials (2.18), we find

$$\vec{\mathbf{n}}\times(\vec{\mathbf{n}}\times\vec{\beta}) = -(\beta_x cos\theta cos\phi + \beta_y cos\theta sin\phi - \beta_z sin\theta)\hat{\mathbf{e}}_\theta + (\beta_x sin\phi - \beta_y cos\phi)\hat{\mathbf{e}}_\phi \quad (2.22)$$

$$\vec{\mathbf{n}}\cdot\vec{\mathbf{r}} = x sin\theta cos\phi + y sin\theta sin\phi - z cos\theta \quad (2.23)$$

By substituting equations (2.22) and (2.23) into equation (2.18), we arrive at our final result

$$\frac{d^2W_\theta}{d\omega d\Omega} = \frac{e^2\omega^2}{4\pi^2c^3}\left|\int_{-T_p/2}^{T_p/2}\left(\frac{dx}{dt}cos\theta cos\phi + \frac{dy}{dt}cos\theta sin\phi - \frac{dz}{dt}sin\theta\right)e^{i\Psi}dt\right|^2 \quad (2.24)$$

$$\frac{d^2W_\phi}{d\omega d\Omega} = \frac{e^2\omega^2}{4\pi^2c^3}\left|\int_{-T_p/2}^{T_p/2}\left(\frac{dx}{dt}sin\phi + \frac{dy}{dt}cos\phi\right)e^{i\Psi}dt\right|^2 \quad (2.25)$$

where

$$\Psi = (\omega/c)(ct - z cos\theta - x sin\theta cos\phi - y sin\theta sin\phi) \quad (2.26)$$

The integral from ±∞ has been replaced by a time, T_p. This represents the electron-plasma interaction time.

Assuming betatron motion in the x-z plane[2], equations (2.9), (2.10), (2.14), and (2.15) are input into equations (2.24), (2.25), and (2.26) to arrive at a final result.

Grouping the phase term (Ψ) in the x-z plane gives the following result

$$\Psi = (\alpha_o ct - z_o cos\theta)k - \alpha_x sin(w_b t) - \alpha_z sin(2w_b t), \quad (2.27)$$

$$\alpha_o = 1 - \beta_{zo}\left(1 - \frac{K^2}{4\gamma_{zo}^2}\right)cos\theta, \quad (2.28)$$

$$\alpha_x = \frac{kK}{\gamma_{zo}k_\beta}sin\theta cos\phi, \quad (2.29)$$

and

$$\alpha_z = \beta_{zo}\left(\frac{kK^2}{8\gamma_{zo}^2k_\beta}\right)cos\theta \quad (2.30)$$

where $k = \omega/c$. This result can be integrated over the electron-plasma interaction distance (i.e. $L_p = cT_p$) to give the spectral content at any observation location downstream.

---

[2] $r = x$ and $y = 0$

When $K \leq 1$, the majority of the radiation resides in the fundamental frequency. As $K \gg 1$, higher order harmonics begin to contribute far greater radiated energy to the far-field than the fundamental. The higher order harmonics are due to velocity fluctuations in the axial direction of the electron. This can be understood by examining equation (2.14). As K increases, the axial velocity fluctuations become large due to the K^2 dependence of the $sin(2\omega_\beta t)$ term. Small variations in $K = \gamma_{zo} k_\beta r_\beta$ will lead to changes in the fundamental resonant frequency for electrons of different radii. This causes the individual spectra of the electrons to overlap resulting in a broadband spectrum at all locations in the far-field.

The radiated energy in the far-field can be given a Bessel Function solution. This result provides some intuitive equations to further explain characteristics of the radiation field. The Bessel solution is

$$\frac{d^2W}{d\omega d\Omega} = \sum_{n=1}^{\infty} \frac{e^2k^2}{4\pi^2 c}\left(\frac{sin(\bar{k}L_p/2)}{\bar{k}}\right)^2 [C_x^2(1 - sin^2\theta cos^2\phi) + C_z^2 sin^2\theta - C_x C_z sin2\theta cos\phi] \tag{2.31}$$

where

$$C_x = k_\beta r_\beta \sum_{m=-\infty}^{\infty} J_m(\alpha_z)[J_{n+2m-1}(\alpha_x) + J_{n+2m+1}(\alpha_x)], \tag{2.32}$$

$$C_z = \beta_{zo} \sum_{m=-\infty}^{\infty} J_m(\alpha_z)[2(1+k_\beta^2 r_\beta^2/4)J_{n+2m}(\alpha_x) - (k_\beta^2 r_\beta^2/4)(J_{n+2m-2}(\alpha_x)+J_{n+2m+2}(\alpha_x))], \tag{2.33}$$

$$\alpha_z = \frac{n(k/k_n)(K^2/4)cos\theta}{(1+K^2/2)cos\theta + 2\gamma_{zo}^2(1-cos\theta)}, \tag{2.34}$$

$$\alpha_x = \frac{2n(k/k_n)\gamma_{zo} K sin\theta cos\phi}{(1+K^2/2)cos\theta + 2\gamma_{zo}^2(1-cos\theta)} \tag{2.35}$$

and

$$\bar{k} = \alpha_o k - n k_o \tag{2.36}$$

J_m are Bessel functions, n is the harmonic number, and k_o is the fundamental wavenumber of the electron.

Upon examining equation (2.31), the existence of harmonic content of the radiation field becomes evident due to the resonance function defined as

$$R_n(k) = \left(\frac{sin(\bar{k}L_p/2)}{\bar{k}}\right)^2 \tag{2.37}$$

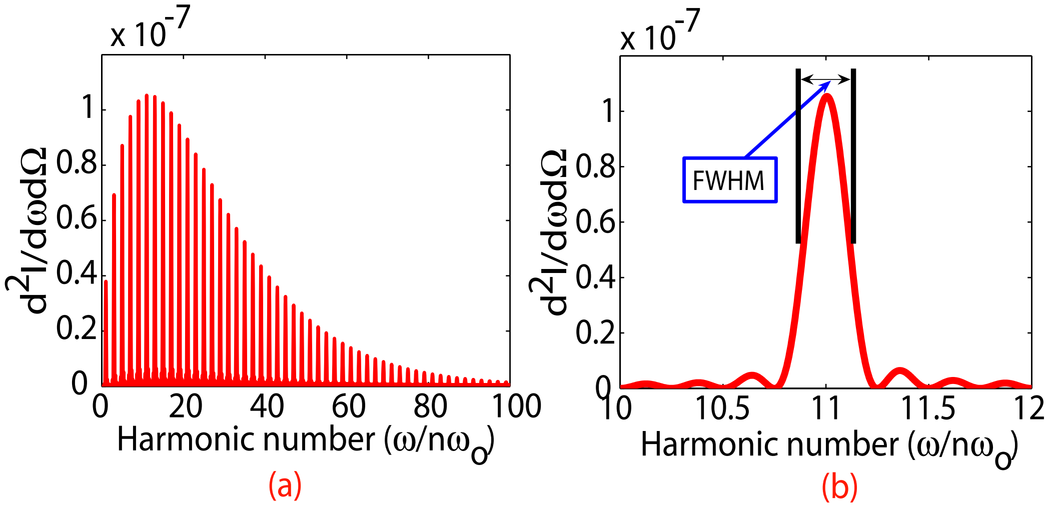

Figure 2.2: Axial radiation spectrum ($\theta = 0$) for one electron with $r_\beta = 10\mu m$, $n_{pe} = 1 \times 10^{14} cm^{-3}$ and $N_\beta = 4$; (a) The harmonic structure of the entire spectrum. (b) The 11th harmonic showing the expected dependence of the full-width at half maximum (FWHM $= \Delta\omega_n$), $\Delta\omega_n/\omega_o = 1/N_\beta = .25$ for our case.

This function peaks when the denominator is zero, giving the equation for the resonant wavenumber, $k_n = nk_\beta/\alpha_o$. Since $\gamma_z \gg 1$, equation (2.14) can be expanded to yield $\beta_z = 1 - 1/2\gamma^2$. This result is input into equation (2.28) to give

$$k_n = \frac{nk_\beta}{\alpha_o} \simeq \frac{2\gamma_{zo}^2 nk_\beta}{(1 + K^2/2)cos\theta + 2\gamma_{zo}^2(1 - cos\theta)} \tag{2.38}$$

For frequencies of interest, the radiation is confined to a cone of $\theta \ll 1$. Equation (2.38) can be approximated as

$$\omega_n \simeq \frac{n2\omega_\beta\gamma_{zo}^2}{1 + K^2/2 + (\gamma_{zo}\theta)^2} \tag{2.39}$$

The characteristic bandwidth of each harmonic is $\Delta\omega_n/\omega_o = 1/N_\beta$. This is illustrated in figure 2.2. For on-axis radiation, $\theta = 0$, and with $K \gg 1$, equation (2.38) can be expanded to yield

$$\omega_n \simeq \frac{n4\gamma_{zo}^2\omega_\beta}{K^2} \tag{2.40}$$

The spectrum can be defined by a critical frequency, ω_c. The critical frequency is defined as the frequency where half the radiated energy resides above and half resides below. It can be written in the following form

$$\omega_c = n_c\omega_o \tag{2.41}$$

where ω_o is the fundamental frequency as defined in equation (2.40) and n_c is the critical harmonic number for our conditions of $K \gg 1$ and $\theta \ll 1$. The critical harmonic number can be shown to be $n_c = 3K^3/8$ giving the following form for the critical frequency, $\omega_c = 3K\gamma_{zo}^2\omega_\beta/2$. The number of harmonics increases on the order of K^3. This gives a $n_{pe}^{3/2}$ dependence to the number of harmonics. It is clear that the number of harmonics that must be resolved becomes enormous as we reach densities on the order of $10^{17}cm^{-3}$. Also, the Bessel Functions (J_n) in equation (2.31) converge slowly at high harmonic numbers (n) making this computational method prohibitively expensive on a single-processor for the densities of interest. Due to computational limitations, $n_{pe} = 1 \times 10^{14}cm^{-3}$ was used for figure 2.2. This concludes the derivation of Esarey et al. [13].

2.3 The Saddle-Point Method for Betatron Spectrum Calculation

Due to the computational limitations of the Bessel solution for the Lienard-Wiechert potentials (2.31), it was necessary to formulate an approximate solution. This result was found in Kostyukov et al. [16]. Until further notice, the following derivation is adapted from that work.

It is understood that an accelerated charged particle radiates energy in a narrow cone angle ($\theta = 1/\gamma$) when propagating at relativistic velocities. For a particle undergoing betatron oscillations in a plasma, the radiation cone is centered around the instantaneous momentum vector ($\vec{p}$) of the particle. At different locations along the orbit, the cone angle points in different directions as illustrated in figure 2.3. It is clear that only the radiation emitted from certain phases along the betatron curve will give a contribution to a particular point in the far field defined by vector $\vec{k}$ (i.e. $\vec{k} \cdot \vec{p} \neq 0$). This allows the calculation of only the radiation from specific contributing phases along the betatron trajectory decreasing the computational time by orders of magnitude.

At some specific time, $\vec{k}$ and $\vec{p}$ are parallel, defining the "Saddle-Point" for this

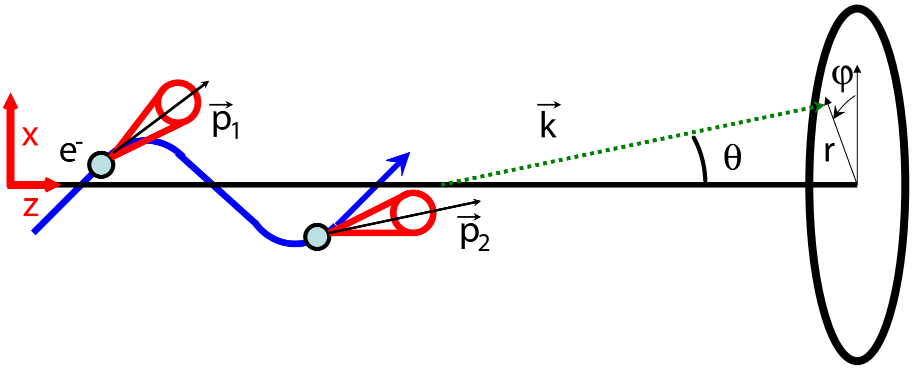

Figure 2.3: Schematic of the Saddle-Point Method. $\vec{p}_1$ will not contribute to the spectrum at the far-field position determined by $\vec{k}$ since $\vec{k} \cdot \vec{p}_1$ is small. However, $\vec{p}_2$ will have a substantial contribution to the far-field at that point since $\vec{k} \cdot \vec{p}_2$ is large.

particular $\vec{k}$. This result will be derived below. Equations (2.24) and (2.25) can be expanded around this moment in time and integrated to arrive at the desired result. The instantaneous radius of curvature at the "Saddle-Point" has a characteristic synchrotron-like spectrum. Thus, this method approximates the radiation field to that of a particle moving in a circular path. This eliminates the computational expense associated with the higher harmonic resolution issues. It should be noted that for this mathematical approach to remain physically accurate the electron deflection angle must be far greater than the angular spread of the spontaneous radiation[3]. Assuming the betatron orbit in the x-z plane, using equation (2.10), p_x and p_z become

$$p_x = \gamma_{zo} mc\beta_x(t=0) = Kmc \tag{2.42}$$

and

$$p_z = \gamma_{zo} mc. \tag{2.43}$$

This results in the following condition for the Saddle-Point method to be applicable, $K \gg 1$. This is the same high harmonic condition solved by Esarey et al. [13] and is the regime of our experiments.

Assuming a betatron orbit in the x-z plane, we expand the phase term in equations (2.24) and (2.25) around a moment in time, $\epsilon_n = \omega_\beta t_n$, to third-order giving

$$\Psi = \Psi_o + b_1(\epsilon - \epsilon_n) + \frac{b_2}{2}(\epsilon - \epsilon_n)^2 + \frac{b_3}{6}(\epsilon - \epsilon_n)^3, \tag{2.44}$$

---

[3] $p_x/p_z \gg 1/\gamma$ where p_x and p_z are the maximum momentum values in each respective direction

where

$$\Psi_o = \Psi(\epsilon_n) = \alpha_o\epsilon_n - \alpha_x sin(\epsilon_n) + \alpha_z sin(2\epsilon_n), \tag{2.45}$$

and

$$b_1 = \left.\frac{d\Psi}{d\epsilon}\right|_{\epsilon=\epsilon_n} = \alpha_o - \alpha_x cos(\epsilon_n) + 2\alpha_z cos(2\epsilon_n), \tag{2.46}$$

$$b_2 = \left.\frac{d^2\Psi}{d\epsilon^2}\right|_{\epsilon=\epsilon_n} = \alpha_x sin(\epsilon_n) - 4\alpha_z sin(2\epsilon_n), \tag{2.47}$$

$$b_3 = \left.\frac{d^3\Psi}{d\epsilon^3}\right|_{\epsilon=\epsilon_n} = \alpha_x cos(\epsilon_n) - 8\alpha_z sin(2\epsilon_n) \tag{2.48}$$

where α_o, α_x, and α_z are defined by equations (2.28), (2.35), and (2.34), respectively.

We now expand to first-order the terms before the exponential giving

$$\frac{dx}{dt}cos\theta cos\phi - \frac{dz}{dt}sin\theta = B_{\theta,n} + D_{\theta,n}(\epsilon - \epsilon_n), \tag{2.49}$$

and

$$\frac{dx}{dt}sin\phi = B_{\phi,n} + D_{\phi,n}(\epsilon - \epsilon_n), \tag{2.50}$$

where

$$B_{\theta,n} = cos\theta\frac{K}{\gamma_{zo}}cos(\epsilon_n)cos\phi - \beta_{zo}sin\theta + sin\theta\frac{\beta_{zo}K^2}{4\gamma_{zo}^2}cos(2\epsilon_n), \tag{2.51}$$

$$D_{\theta,n} = -cos\theta\frac{K}{\gamma_{zo}}sin(\epsilon_n)cos\phi - sin\theta\frac{\beta_{zo}K^2}{2\gamma_{zo}^2}sin(2\epsilon_n), \tag{2.52}$$

$$B_{\phi,n} = \frac{K}{\gamma_{zo}}cos(\epsilon_n)sin\phi, \tag{2.53}$$

$$D_{\phi,n} = -\frac{K}{\gamma_{zo}}sin(\epsilon_n)sin\phi. \tag{2.54}$$

The main contribution to the integral occurs near the Saddle-Points. These are determined when $d\Psi/d\epsilon$ is minimized. The first-order term in the phase expansion (2.46) can be written as follows

$$\left.\frac{d\Psi}{d\epsilon}\right|_{\epsilon=\epsilon_n} = 1 - \frac{p_z}{\gamma_{zo}}cos\theta = 1 - \frac{\vec{k}\cdot\vec{p}}{k\gamma_{zo}} \tag{2.55}$$

where $p_z = \beta_{zo}\gamma_{zo}$. It is clear that $d\Psi/d\epsilon$ is minimized when $\vec{k}$ and $\vec{p}$ are parallel, providing the largest contribution to the radiation field. This follows the logic discussed above.

To determine the values of the Saddle-Points (ϵ_n), we use the quantitative result that $d\Psi/d\epsilon$ is minimized when $d^2\Psi/d\epsilon^2 = 0$. Using equation (2.47), we define the Saddle-Points as

$$cos(\epsilon_n) = \frac{1}{\beta_{zo}}\frac{\gamma_{zo}}{K}tan\theta cos\phi. \tag{2.56}$$

There are two Saddle-Points per betatron oscillation. This gives $2N_\beta = \omega_\beta T/\pi$ as the total number of Saddle-Points where N_β is the number of betatron oscillations. In the phase expansion, b_2 (2.47) can be neglected due to the $sin(\epsilon_n)$ term, giving the following form for (2.24) and (2.25)

$$\frac{d^2W_j}{d\omega d\Omega} = \frac{e^2\omega^2}{4\pi^2c^3}|I_j|^2 \tag{2.57}$$

where

$$I_j = \frac{1}{\omega_\beta}\sum_{n=1}^{2N_\beta} exp(i\Psi_{o,n})R_{j,n} \tag{2.58}$$

and

$$R_{j,n} = \int_{-\infty}^{+\infty}(B_{j,n} + D_{j,n}s_n)exp\left(ib_{1,n}s_n + i\frac{b_{3,n}}{6}s_n^3\right)ds_n \tag{2.59}$$

where $j = \theta, \phi$ is the polarization, $s_n = (\epsilon - \epsilon_n)$, and n is the Saddle-Point index.

It is clear from equation (2.56) that for an individual electron the energy radiated to a specific $\vec{k}$ is equal at all Saddle-Points. Thus, we can remove the summation in equation (2.58) and replace it with $2N_\beta$.

We now integrate equation (2.59). Begin by splitting the function into real and imaginary parts

$$R_j = \int_{-\infty}^{+\infty} B_j cos\left(b_1 s + \frac{b_3}{6}s^3\right)ds + i\int_{-\infty}^{+\infty} sD_j sin\left(b_1 s + \frac{b_3}{6}s^3\right)ds \tag{2.60}$$

The other two terms integrate to zero since they are odd functions integrated over infinite time. The following identities are used

$$\frac{2}{\sqrt{3}}K_{1/3}(\xi) \equiv \int_{-\infty}^{+\infty} cos\left[\frac{3}{2}\xi\left(x + \frac{1}{3}x^3\right)\right]dx = \int_{-\infty}^{+\infty} cos\left(b_1 s + \frac{b_3}{6}s^3\right)ds, \tag{2.61}$$

$$\frac{2}{\sqrt{3}}K_{2/3}(\xi) \equiv \int_{-\infty}^{+\infty} xsin\left[\frac{3}{2}\xi\left(x + \frac{1}{3}x^3\right)\right]dx = \int_{-\infty}^{+\infty} (s)sin\left(b_1 s + \frac{b_3}{6}s^3\right)ds \tag{2.62}$$

where $K_{1/3}$ and $K_{2/3}$ are modified Bessel Functions. Set $s = \alpha x$, $3\xi/2 = b_1 s$, and $1/2\xi x^3 = b_3 s^3/6$ where α is a constant that will be determined. Solving the

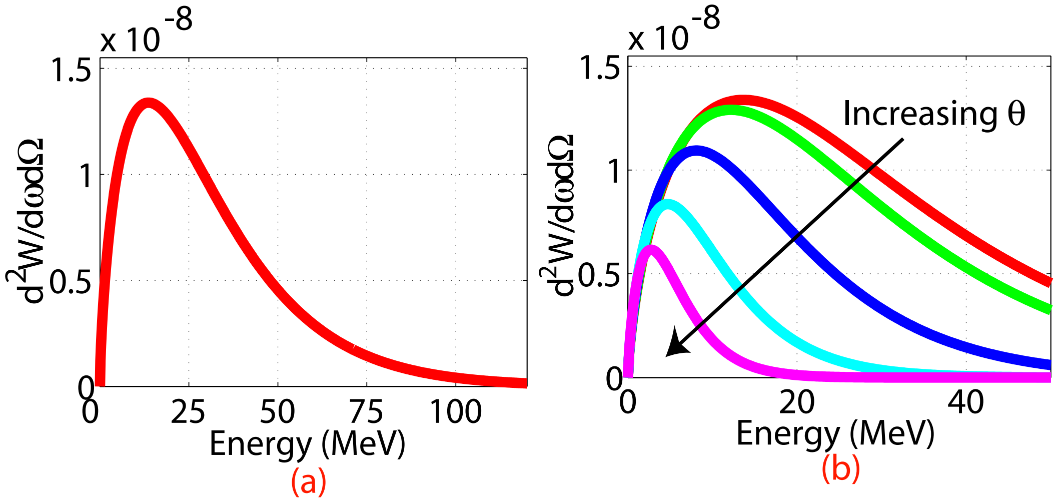

Figure 2.4: Solutions to equation (2.57) using the Saddle-Point method. This assumes an electron with $E = 28.5GeV$, $r = 10\mu m$ and $n_{pe} = 1 \times 10^{17} cm^{-3}$. The units of $d^2W/d\omega d\Omega$ are $eV \cdot s/\Omega$. (a) At $\phi = 0$ and $\theta = 0$. (b) At $\phi = 90$ with increasing θ.

equations, we find $\alpha = \sqrt{\frac{2b_1}{3}}$ and $\xi = \sqrt{\frac{8b_1^3}{9b_3}}$ giving the following result for equation (2.59)

$$R_j = \sqrt{\frac{8b_1}{3b_3}} \left[B_j K_{1/3} \left(\sqrt{\frac{8b_1^3}{9b_3}} \right) + iD_j \sqrt{\frac{2b_1}{b_3}} K_{2/3} \left(\sqrt{\frac{8b_1^3}{9b_3}} \right) \right] \tag{2.63}$$

This gives the final result

$$I_j = \frac{2N_\beta}{\omega_\beta} exp(i\Psi_o) R_j \tag{2.64}$$

that can be plugged into (2.57) to get a solution that can be easily computed. This concludes the derivation found in Kostyukov et. al. [16].

FORTRAN90 and MATLAB codes were written to perform this function and postprocess the results. The following data consists of the spectrum from an electron with $E = 28.5GeV$, $r = 10\mu m$ and $N_{pe} = 1 \times 10^{17} cm^{-3}$.

At each location in the far-field (θ, ϕ, z), equation (2.57) is solved for both θ and ϕ. An example of the radiation spectrum on axis $(\theta = 0, \phi = 0)$ is given in figure 2.4. The synchrotron-like shape is evident. Figure 2.4a gives the axial spectrum while figure 2.4b gives the spectra at $\phi = 90$ with increasing θ. This shows the evolution of the spectra as $\vec{k}$ moves off axis. As expected, the total radiated energy decreases as θ increases.

Using a Simpsons 3/8 rule, the spectra can be integrated over frequency $(d\omega)$ to

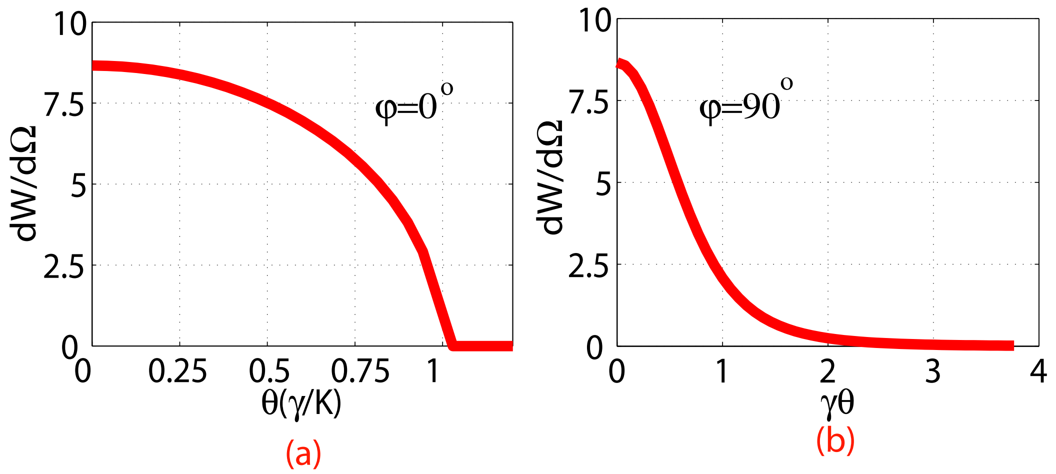

Figure 2.5: Line-outs of the total radiated energy in the far-field using the Saddle-Point method. This assumes an electron with $E = 28.5GeV$, $r = 10\mu m$ and $n_{pe} = 1 \times 10^{17} cm^{-3}$. The units of $dW/d\Omega$ are eV/Ω; (a) Parallel to particle oscillation plane, x-axis ($\phi = 0$), $\theta_x = K/\gamma$ dependence. (b) Perpendicular to particle oscillation plane, y-axis ($\phi = 90$), $\theta_y = 1/\gamma$ dependence.

compute the total energy radiated to each far-field location ($\vec{k}$). This is shown in figure 2.5. The dependence on radiated power is: $\theta_x = K/\gamma$ parallel to the oscillation plane and $\theta_y = 1/\gamma$ perpendicular to the oscillation plane as expected. The contour plots in figures 2.6a and 2.6b verify this dependence. Since in our case $K = 99.5$, the angular spread of radiation in the oscillation plane ($\theta = K/\gamma$) is far greater than the characteristic spread of a radiating particle ($\theta = 1/\gamma$). This provides further verification that we were justified in using the Saddle-Point method.

2.4 Total Radiated Power from an Electron Undergoing Betatron Oscillations

The total radiated power by a single relativistic electron (P_e) in an arbitrary orbit can be computed from the Larmor formula [13]

$$P_e = \frac{2e^2}{3m^2c^3}\gamma^2\left[\left(\frac{d\vec{p}}{dt}\right)^2 - m^2c^2\left(\frac{d\gamma}{dt}\right)^2\right] \tag{2.65}$$

where $\vec{p}$ is the electron momentum and is defined as $\vec{p} \equiv \gamma m\vec{v}$. It is clear from equation (2.12) that if $K \ll \gamma$ as in our case that $\gamma \approx \gamma_{zo}$ and $d\gamma/dt = 0$. For

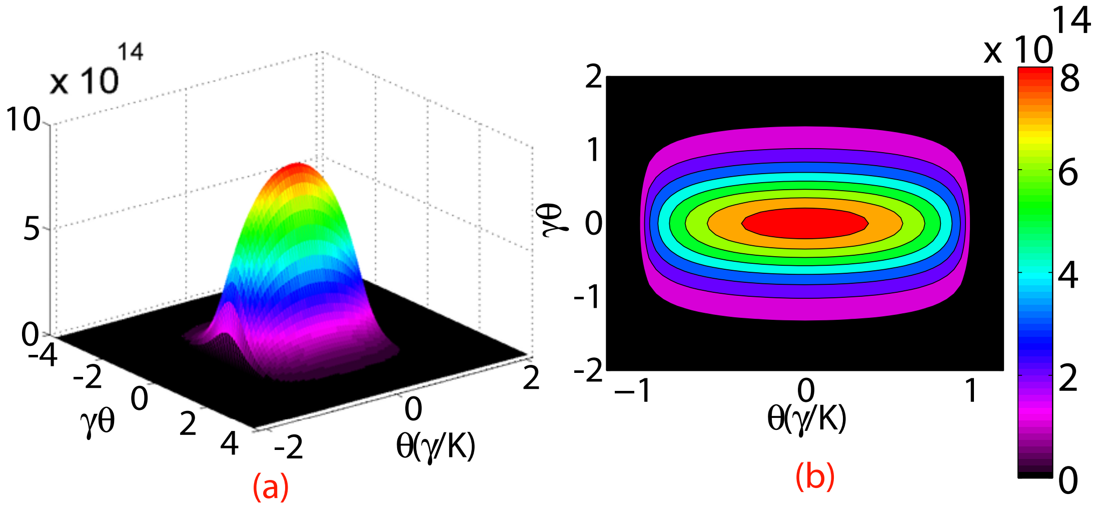

Figure 2.6: Contour plots of the total radiated energy in the far-field using the Saddle-Point method. This assumes an electron with $E = 28.5GeV$, $r = 10\mu m$ and $n_{pe} = 1 \times 10^{17} cm^{-3}$. The units of $dW/d\Omega$ are eV/Ω; (a) 3-D. (b) 2-D projection of (a).

the same reason, the axial velocity is roughly unchanged leaving only dp_x/dt to contribute to equation (2.65)

$$\frac{d\vec{p}}{dt} = \gamma m \frac{du_x}{dt} = -\gamma m \omega_\beta^2 x \tag{2.66}$$

where x is defined by setting $r = x$ in equation (2.9). Plugging this result into equation (2.65) defines the electron power loss in an ion column as

$$P_e \approx \frac{2}{3} e^2 c \gamma_{zo}^4 k_\beta^4 r_\beta^2 cos^2(\omega_\beta t) \tag{2.67}$$

Integrating this result over a betatron period for one electron gives the average radiated power per betatron period as

$$\bar{P}_e \approx \frac{1}{3} e^2 c \gamma_{zo}^4 k_\beta^4 r_\beta^2 = \frac{1}{3} e^2 c \gamma_{zo}^2 k_\beta^2 K^2 \tag{2.68}$$

The total electron energy loss per unit length is given by $W_{loss}/dz = \bar{P}_e/c$ becoming

$$\frac{dW_{loss}}{dz} = \frac{1}{3} r_e m_e c^2 \gamma_{zo}^2 k_\beta^2 K^2 \tag{2.69}$$

where $r_e = e^2/m_e c^2$ is the classical electron radius. This is the same result derived by Wiedemann [5]. The Wiedemann result was derived for a magnetic wiggler.

Our "plasma wiggler" utilizes the electrostatic potential (Φ) from the ion column to "wiggle" the beam. An important difference should be noted. In a magnetic wiggler, electrons at all radii have the same K due to the constant B-field whereas in the "plasma wiggler" electrons at different radii experience a different wiggler strength ($K = \gamma k_\beta r$) due to the radial dependence of the electrostatic potential. Equation (2.69) applies to both scenarios, but must be computed for all electron radii within a beam when referring to energy loss within an ion column.

Equation (2.69) states that the radiated energy is a function of γ^2, N_{pe}^2 and r_β^2. An electron at $2\sigma_r$ radiates 4 times as much energy as an electron at σ_r. It may seem incredible to note that a $E = 28.5GeV$ electron with $\sigma_r = 10\mu m$ and $n_{pe} = 3 \times 10^{17} cm^{-3}$ radiates about 4.25 GeV/m! Moreover, it may seem logical to assume that an electron at $r = 3\sigma_r$ with the same parameters would radiate 9 times as much energy (38.2 GeV/m). On the cm scale, this is accurate, but it obviously fails at longer plasma lengths. The failure comes from the initial assumptions in equations (2.3) and (2.4). They state that $d\beta_z/dt = 0$ and $d(\gamma - \Phi)/dt = 0$ over the entire betatron oscillation. At high K, the radiation loss is so large that extra terms need to be added to equations (2.3) and (2.4) to conserve energy. This will account for the changes in γ and β_z in time making $d\gamma/dt$ and $\gamma^2(t)$ important terms in equation (2.65). This results in a decrease in the energy loss gradient as the electron propagates farther into the plasma. However, for the results quoted in this chapter assuming 4 betatron oscillations with $n_{pe} = 1 \times 10^{17} cm^{-3}$, the assumptions used are valid. This equates to an energy loss gradient of 472 MeV/m and about 66.5 MeV of energy loss for a $\sigma_r = 10\mu m$ or 4.25 GeV/m and 600 MeV of energy loss for $3\sigma_r$ electrons.

To verify that the Saddle-Point method gives an accurate result for the electron energy loss, equation (2.57) was integrated using the Simpson's 3/8 Rule for $d\omega$ as noted earlier. The resulting energy per solid angle was integrated in θ and ϕ using the Trapezoid Rule. The results between theory and computation for a single electron are shown in table 2.1. The results match to high precision with the errors being less than 1 percent. The small error is due to the numerical errors associated

$n_{pe}(1/cm^3)$	$WiedemannFormula(MeV)$	$Calculated(MeV)$	$Error$
1×10^{17}	66.5	66.0	.00752
2×10^{17}	188.1	187.8	.00159
3×10^{17}	346	348	.00578

Table 2.1: The comparison of theoretical [5] and computed values for the total energy loss from one electron with $N_\beta = 4$.

with the numerical integration. These errors decrease as the number of θ points and ϕ points increase helping to eliminate aliasing issues, but the computational time increases with added grid points (θ, ϕ) in the far-field. The acceptable errors must be determined by the user.

The code takes a few extra steps for a beam of electrons. The user inputs a radial distribution ($w_e(r)$) and a total number of electrons (N_e) for the beam. Each radial distribution point corresponds to a betatron radius. The radiation field ($d^2W_r/d\omega d\Omega$) is computed for each betatron radius at all far-field locations (θ, ϕ) and multiplied by the total number of electrons in that radial bin defined by $d^2W_r/d\omega d\Omega \cdot w_e(r) \cdot N_e$. This gives the spectrum at each location in the far-field from all electrons in the r-z plane specified. The beam is assumed to have azimuthal symmetry. This assumption is justified since the pair production target and detectors also contain that symmetry. The spectrum from the specific r-z plane is mirrored and added at all ϕ points to simulate electrons in all r-z planes. This decreases the computational time by a large degree since all r-z planes give the same spectrum. The result of a azimuthally symmetric ”ring of electrons” with $\sigma_r = 10\mu m$ is shown in figure 2.7a. The amplitude is large $\theta < 1/\gamma$ and drops quickly as $\theta > 1/\gamma$. This is due to the fact that for all ϕ there is radiation out to at least $\theta = 1/\gamma$. However, there is only radiation near $\theta = K/\gamma$ in the plane of the oscillating electron as seen in figure 2.6. The line-out of the amplitude can be seen in figure 2.7b. The radiation drops nearly to zero at $\theta = K/\gamma$ as expected.

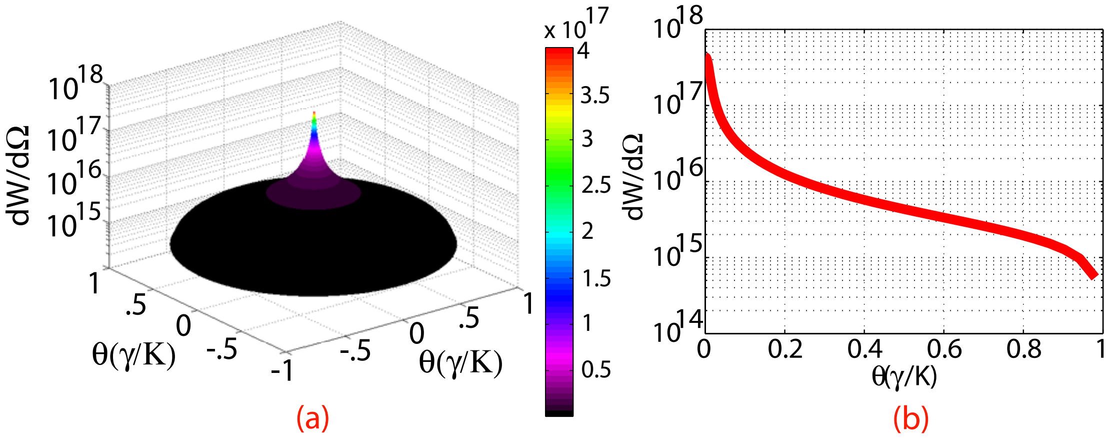

Figure 2.7: Total radiated energy for a azimuthally symmetric ”ring of electrons” with $\sigma_r = 10\mu m$. The units of $dW/d\Omega$ are eV/Ω; (a) 3-D contour plot with log scale for the amplitude ($dW/d\Omega$). (b) Line out at $\phi = 0$ for increasing θ with log scale for the amplitude ($dW/d\Omega$).

2.5 Plasma Formation by Field Ionization

Up to this point, it has been discussed how oscillating or betatron motion of the beam electrons in a plasma wiggler leads to a synchrotron-like X-ray spectrum in the forward direction. In this section, it will be discussed how to generate perfectly uniform and dense plasmas that are needed to produce this radiation. The process is called field-ionization (sometimes referred to as tunnel ionization).

2.5.1 Field Ionization

For a given n_{pe}, the three most important parameters for determining the X-ray spectrum and the ultimate positron yield are the number of radiating electrons in the ion column N_{bi}, the energy of the radiating electrons γ, and the radius of the electron beam in the ion column $\sigma_{i:x,y}$. One of the most challenging aspects of this experiment was determining the number of particles radiating in the ion column. With a pre-formed ion column, that number is the total number of electrons in the beam, however, due to the field ionization process, the incoming beam density will determine the location of ionization within the longitudinal extent of the electron beam. This ultimately will determine the number of particles in the ion column.

Field ionization has important implications for the experiment. It allows the beam-plasma system to be self-guiding, offering large advantages over conventional UV laser ionization of a gas which suffers from difficult uniformity and alignment issues. However, it is challenging to compute the distribution of particles in the ion column in the field ionization regime.

We begin with a qualitative ion column analysis to understand the challenging aspects of modeling the X-ray radiation from a field ionized plasma. The electron distribution for a 3-D Gaussian beam is

$$n_b(x,y,z) = n_{bo} e^{-x^2/2\sigma_x} e^{-y^2/2\sigma_y} e^{-z^2/2\sigma_z} \tag{2.70}$$

where n_{bo} is the peak bunch density. This distribution can be integrated using Gauss's Law to find the peak electric field E_{peak} of the bunch. The peak field occurs at $r = 1.6\sigma_r$ as shown in Figure 2.8b, and it can be described using the following engineering formula [4]

$$E_{peak}[GV/m] \approx 40\left(\frac{N}{2\times 10^{10}}\right)\left(\frac{15\mu m}{\sigma_r[\mu m]}\right)\left(\frac{20\mu m}{\sigma_z[\mu m]}\right) \tag{2.71}$$

If the electric field at any point within the electron beam E_{beam} is large enough, the plasma will field ionize. The theory of field ionization is summarized briefly below, but for detailed analysis, please refer to Caolionn O'Connell's thesis [4].

The Ammosov-Delone-Krainov (ADK) model [17, 18] gives a formula for the ionization rate of a gas in a given electric field

$$W \approx 1.54\times 10^{15} \frac{4^n \zeta[eV]}{n\Gamma(2n)} \left(20.5\frac{\zeta^{3/2}[eV]}{E[GV/m]}\right)^{2n-1} exp\left(-6.83\frac{\zeta^{3/2}[eV]}{E[GV/m]}\right) \tag{2.72}$$

where W is the ionization rate per second, ζ is the ionization potential of the outermost Li electron, $n \approx 3.69Z/\sqrt{\zeta}[eV]$ is the principal quantum number and Z is the ionization state. Li is a good choice for the plasma because the ionization potential of the outermost electron is 5.4 eV while the ionization potential of the second electron is 75 eV. This energy gap between the two states makes it difficult for ionization of the second electron to occur. For the outermost Li electron (Z=1), equation 2.72 can be simplified using the Li ionization potential of $\zeta = 5.4eV$ to give

$$W_{Li} \approx \frac{3.6\times 10^{21}}{E^{2.18}[GV/m]} exp\left(-6.83\frac{-85.5}{E[GV/m]}\right) \tag{2.73}$$

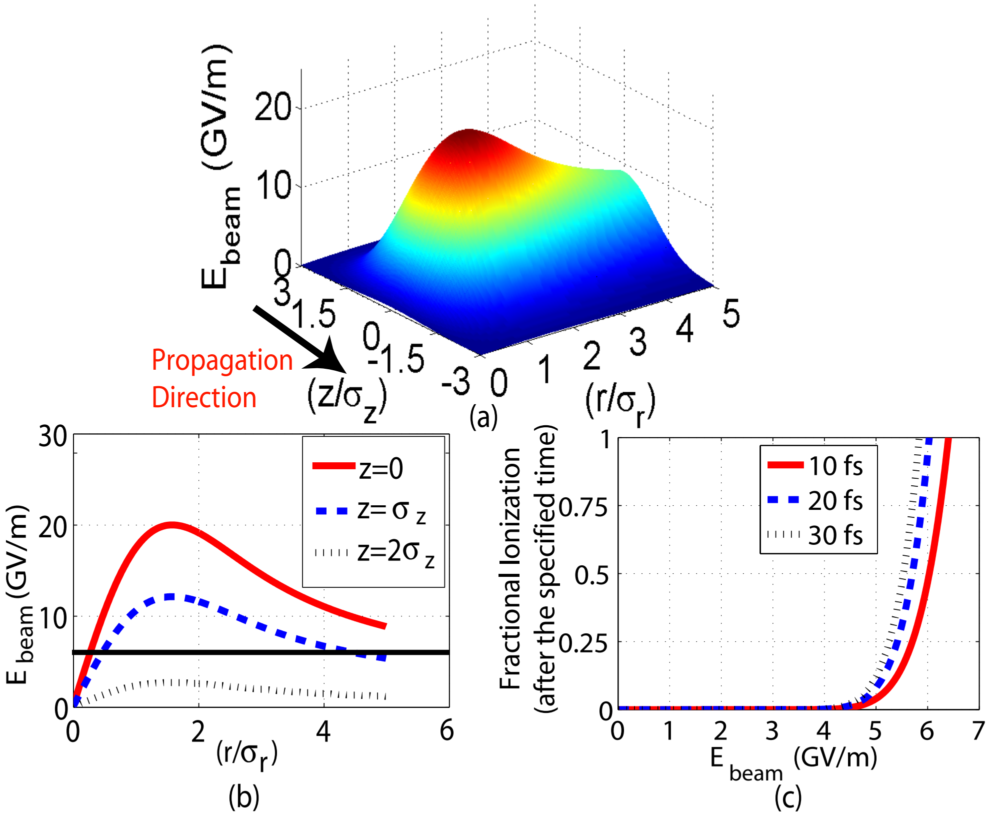

Figure 2.8: (a) A contour plot showing the electric field distribution within a Gaussian electron beam with $N_b = 1.2 \times 10^{10}$ electrons, $\sigma_z = 29\mu m$, and $\sigma_r = 11\mu m$. (b) Plot of the radial lineout of the electric field for $z = 0$, $z = \sigma_z$, and $z = 2\sigma_z$. The black horizontal line defines $E_{beam} = 6GV/m$. (c) The fractional percentage of ionized Li atoms after 10, 20 and 30 fs.

Equation 2.73 has physical values between 0 and unity. Once $W_{Li} > 1$, the Li vapor is fully field ionized.

Figure 2.8a shows the electric field contours for a Gaussian beam with $N_b = 1.2 \times 10^{10}$ electrons, $\sigma_z = 29\mu m$, and $\sigma_r = 11\mu m$. Figure 2.8b plots radial lineouts of Figure 2.8a at positions $z = 0$,$z = \sigma_z$, and $z = 2\sigma_z$, and Figure 2.8c shows the fractional ionization of the Li vapor after 10 fs, 20 fs and 30 fs versus E_{beam}. It is clear from this plot that full ionization in Li occurs almost instantaneously when $E_{beam} = 6GV/m$ (20 fs curve). The black horizontal line in Figure 2.8b shows the radial distribution of electrons that reside in this region where $E_{beam} > 6GV/m$. This figure states that at the peak electron beam density (i.e. $z = 0$), the majority of the radial bins are above the threshold of 6 GV/m. However, at $z = 2\sigma_z$, no electrons reside above this threshold. This means that only electrons longitudinally downstream of $z = 2\sigma_z$ can physically reside in the ion column, simply because prior to this beam location, there is no plasma.

From this simplistic model, determining an accurate quantitative number of electrons in the ion column is not possible. However, this does give a qualitative benchmark that the more quantitative methods described in the results chapter can be compared against. One may think that the number of electrons radiating in the ion column is simply the total number of electrons residing behind the longitudinal position of ionization, z_i. However, there are two physical effects that cause the ion column to begin at a longitudinal position downstream of z_i. The first effect occurs while vapor ionization is taking place. During this time, the electron beam is still propagating at roughly the speed of light c. This means that for this example, during the 20 fs that it takes for ionization to occur, the beam has already moved forward $6\mu m$ in z. At best, no electrons before $z = z_i - 6\mu m$ can begin to radiate. The second reason is that even after the plasma is created, a total blowout of the plasma electrons still needs to occur to create the ion column for the ensuing electrons to wiggle and radiate. This takes a finite amount of time. In the reference frame of the beam, the plasma electrons blowout at the speed of light. This means that the plasma electrons will travel at a 45 degree angle relative to the beam in the beam reference frame. Thus, by the time a plasma electron has moved out of the central plasma region a distance of $r = \sigma_r$, the beam has already propagated forward a distance $z = \sigma_r$. These two effects give a relative scaling for the effective beginning of the ion column. This qualitative picture suggests that the ion column can at the earliest begin at $\sim z = z_i - \sigma_r - 6\mu m$ behind the location of $E_{beam} > 6GV/m$ where full ionization begins.

Furthermore, for a pure ion column, Gauss's Law defines the focusing force as

$$E_r = \frac{en_{pe}}{2\epsilon_o} r_\beta \tag{2.74}$$

However, due to the small electric fields near the center of the electron beam (i.e. $r = 0$), initially we may not have a pure ion column. This is illustrated in the $z = \sigma_r$

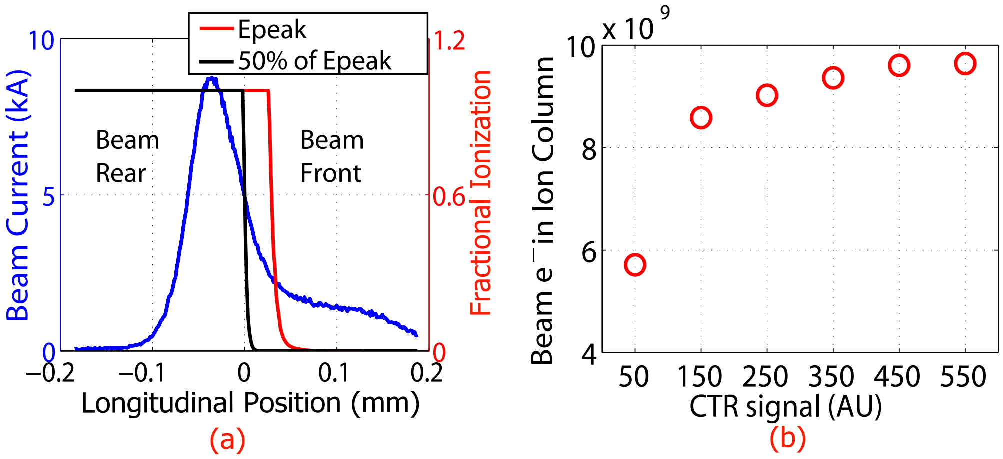

Figure 2.9: (a) An example longitudinal beam profile in the experiment (described later) for a Coherent Transition Radiation (CTR) detector signal of 150. The longitudinal sigma of the peak region is $\sigma_z = 29\mu m$ and the beam $\sigma_r = 11\mu m$. The right vertical axis plots the fractional ionization for E_{peak} (black line) and $.5E_{peak}$ (red line) for the given longitudinal beam location. (b) Computed charge in the ion column by integrating the charge $10\mu m$ downstream of the full ionization of the 50 percent of the peak electric field contour.

case in Figure 2.8b. For this case, Gauss's Law becomes

$$E_r = \frac{en_{pe}}{2\epsilon_o}\left(\frac{r_\beta^2 - r_i^2}{r_\beta}\right) \tag{2.75}$$

where r_i is the radius of the neutral vapor column that has not ionized in the center of the plasma channel. The result is that this reduces the focusing force and thus the K of all the radiating electrons in the outer column. Qualitatively, this is equivalent to an electron with a smaller radius in a pure ion column. Due to the r_β^2 dependence on the radiated power, and the r_β dependence on photon critical energy ω_c, this electron will radiate less energy with a spectrum defined by a smaller ω_c. This will reduce the positron yield.

2.5.2 Estimation of Electrons in the Ion Column

The analysis above can be used in tandem with the the 2-d (z,p_z) simulation code LITRACK [19] to determine a rough number of particles in the ion column. We are able to match the energy spectra measured on the X-ray spectrometer in the FFTB with LITRACK to determine the electron beam phase space and longitudinal profile [3]. Figure 2.9a plots a longitudinal beam profile for a given CTR signal using this method assuming a typical number of beam electrons measured in the experiment $N_{bo} = 1.7 \times 10^{10}$. The resulting longitudinal electron beam profile has a $\sigma_z = 29\mu m$. This is the reason for σ_z in our field ionization example above. The above example also assumed a gaussian beam with $N_b = 1.2\times10^{10}$ (parameters listed above). This is because the longitudinal profile has a "trunk" of charge of roughly 30 percent of the beam. This result has been verified numerous publications [3,4,20]. Figure 2.9a also plots on the right vertical axis the fractional ionization for E_{peak} (black line) and for $.5E_{peak}$ (red line) for the given longitudinal position of the beam. In general, $.5E_{peak}$ offers a good metric to determine the longitudinal position of the beginning of the ion column plus the $\sigma_r + 6\mu m$ distance described above. Using this qualitative reasoning, we can determine an approximate number of particles expected in the ion column. The result of this is shown in Figure 2.9b.

CHAPTER 3

Pair Production Theory

When X-rays with energies greater than 10 MeV collide with a thin, high-Z target, they predominantly decay into electron/positron pairs. The positrons exiting the rear of the target can be captured, collimated and accelerated in linear accelerators to collide with electrons to validate various field theories. This chapter discusses the quantum theory of positron creation in materials. Pair production cross-sections and electron/positron energy distributions after photon decay will also be discussed.

3.1 Schrödinger Equation

The fundamental basis of quantum mechanics begins with the Schrödinger equation [21]

$$i\hbar\frac{\partial\Psi(\vec{r},t)}{\partial t} = -\frac{\hbar^2}{2m}\nabla^2\Psi(\vec{r},t) + V(\vec{r},t)\Psi(\vec{r},t) \tag{3.1}$$

where $\hbar$ is Planck's constant normalized by 2π, $V(\vec{r},t)$ is an energy potential, and $\Psi(\vec{r},t)$ is the particle wave function[1]. The magnitude of the wave function

$$\rho(\vec{r},t) = \mid \Psi(\vec{r},t) \mid^2 = \Psi^*(\vec{r},t)\Psi(\vec{r},t) \tag{3.2}$$

is a probability density[2] for a particle at time t. Integrating $\rho(\vec{r,t})$ over a finite space

$$P = \int \rho(\vec{r},t)d^3\vec{r} \tag{3.3}$$

determines the probability, P, of finding a particle between positions specified by the integral at time t. The probability density function, $\rho(\vec{r},t)$, must be normalized so that the following condition applies

$$\int \rho(\vec{r},t)d^3\vec{r} = 1 \tag{3.4}$$

---

[1] The spatial vector is $\vec{r} = (x, y, z)$ with time t and $\nabla^2 = \frac{\partial^2}{\partial x} + \frac{\partial^2}{\partial y} + \frac{\partial^2}{\partial z}$ is the Laplacian.

[2] $\Psi^*(\vec{r},t)$ is the complex conjugate of $\Psi(\vec{r},t)$.

when the integral is taken over all space.

$$\left[-\frac{\hbar^2}{2m}\nabla^2 + V(\vec{r})\right]\psi(\vec{r}) = E\psi(\vec{r}) \tag{3.5}$$

In classical mechanics, the Hamiltonian is the total energy of a classical system (KE+PE) as defined by

$$H(\vec{r},\vec{p}) = \frac{\vec{p}^2}{2m} + V(\vec{r}) \tag{3.6}$$

This form can be recovered in the Schrödinger equation by assuming that momentum is $\vec{p} = -ih\nabla$. If we take the energy potential, $V(\vec{r},t)$, to be only a function of position, $V(\vec{r})$, separation of variables can be used to yield

$$\Psi_n(\vec{r},t) = \psi_n(\vec{r})e^{-iE_nt/\hbar} \tag{3.7}$$

where $\psi_n(\vec{r})$ is determined by the time-independent Schrödinger equation

$$\left[-\frac{\hbar^2}{2m}\nabla^2 + V(\vec{r})\right]\psi(\vec{r}) = E\psi(\vec{r}) \tag{3.8}$$

This states that there is a specific wave function from the time-independent Schrödinger equation, ψ_n, for each allowed energy, E_n. In certain situations, there can be two or more distinct wave functions for a given energy. These states are degenerate.

A special solution to the time-independent Schrödinger equation arises for a free particle. In this case, the energy potential, $V(\vec{r})$, vanishes from equation (3.8), giving $\psi = e^{i\vec{k}\cdot\vec{r}}$, where $k \equiv \sqrt{2mE}/\hbar$. The resulting solution is

$$\Psi_{jn}(\vec{r},t) = e^{i(\hbar\vec{k}_n\cdot\vec{r}-E_nt/\hbar)}\phi_j \tag{3.9}$$

where ϕ_j are two-component spinors corresponding to the two possible spin states. This solution gives the wavefunction for a free-particle of spin 1/2 with a *non-relativistic* energy. The spin states account for two independent solutions only. In order to include the probability of positrons, modifications need to be made to create a *relativistic* theory.

3.2 The Dirac Equation

The Schrödinger equation applies to *non-relativistic* particles. When special relativity is considered, some corrections to the Schrödinger equation are necessary [22]. It is well-known from the theory of special relativity that the speed of light is constant in all inertial reference frames. This invariance can be stated mathematically with the following relation

$$\sum_{j=1}^{3} x_j^2 - c^2t^2 = \sum_{j=1}^{3} x_j'^2 - c^2t'^2 \tag{3.10}$$

This leads to the famous Lorentz transformations. With $\gamma = 1/\sqrt{1 - v^2/c^2}$, we find

$$x_1' = \gamma(x_1 - vt) \tag{3.11}$$

$$x_2' = x_2 \tag{3.12}$$

$$x_3' = x_3 \tag{3.13}$$

$$t' = \gamma(t - vx_1/c^2) \tag{3.14}$$

where v is the relative velocity in the x_1-direction. The time dilation effect is derived from equation (3.14). If you consider a clock fixed at a location x_1 for two events, the change in time is

$$\Delta t' = t(2) - t(1) = \gamma \Delta t \tag{3.15}$$

To find the proper time, τ, of the system, set $\Delta t = \Delta\tau$. The proper time is always the minimum measurable time between two events, and is defined as the time interval for a stationary object in a given reference frame.

The momentum of the particle is defined as

$$\vec{p} = m\frac{d\vec{x}}{d\tau} = m\frac{d\vec{x}}{dt}\frac{dt}{d\tau} = \gamma m\vec{u} \tag{3.16}$$

where $\vec{u} = d\vec{x}/dt$ is the classical velocity. The total energy of the system (KE+PE) is defined as

$$E = \gamma mc^2 \tag{3.17}$$

A useful kinematic relationship, relating the total energy of the particle to its rest energy and momentum, can be derived from equations (3.16) and (3.17) as

$$E^2 = \gamma^2 m^2 c^4 = p^2c^2 + m^2c^4 \tag{3.18}$$

Equation (3.18) is the foundation for the Klein-Gordon equation [23]. The Klein-Gordon equation is the relativistic version of the free-particle Schrödinger equation.

It is found by defining the Hamiltonian from equation (3.18), $H^2 = p^2c^2 + m^2c^4$. Using the momentum operator, we arrive at

$$-\hbar^2\frac{\partial^2}{\partial t^2}\Psi(\vec{r},t) = [-c^2\hbar^2\nabla^2 + m^2c^4]\Psi(\vec{r},t) \tag{3.19}$$

It is important to note that by using H^2 we have introduced a *negative-energy* root. This will be discussed further below.

In order to have positive-definite probability densities, the Klein-Gordon equation is linearized into a group of N coupled first-order equations [24], giving the famous Dirac equation for spin 1/2 particles. Following Das [24], the momentum operator, $\vec{p} = -i\hbar\nabla$, the Dirac equation is given by

$$i\hbar\frac{\partial\Psi_n(\vec{r},t)}{\partial t} = (c\vec{\alpha}\cdot\vec{p} + \beta mc^2)\Psi_n(\vec{r},t) \tag{3.20}$$

where

$$\Psi_n = \begin{bmatrix} \Psi_1 \\ \Psi_2 \\ . \\ . \\ \Psi_N \end{bmatrix} \tag{3.21}$$

and $\vec{\alpha}$ and β are the NxN Dirac matrices. Two requirements on the Dirac equation are necessary to determine $\vec{\alpha}$ and β. The first is that one should be able to obtain the Klein-Gordon equation from the Dirac equation, and the second is that the probability current densities should satisfy the continuity equation. These two conditions are satisfied if N=4, giving

$$\alpha_i = \begin{bmatrix} 0 & \sigma_i \\ \sigma_i & 0 \end{bmatrix} \tag{3.22}$$

and

$$\beta = \begin{bmatrix} I & 0 \\ 0 & -I \end{bmatrix} \tag{3.23}$$

where I is the N/2 dimensional unit matrix and σ_i are the familiar 2x2 Pauli matrices.

Equation (3.9) is the solution to the Schrödinger equation for *non-relativistic* free particles. Thus, for a *relativistic* free particle, we would expect a solution of the following form

$$\Psi(\vec{r},t) = e^{i(\hbar\vec{k}\cdot\vec{r}-\varepsilon t/\hbar)}U(\vec{p}) \tag{3.24}$$

where $U(\vec{p})$ is a four-component spinor. For the non-relativistic case, we had a two-component spinor, representing the two particle spin states. For the relativistic case, we expect the four-component spinor, $U(\vec{p})$, due to the two particle spin states for both the positive and negative energy states. $U(\vec{p})$ can be conveniently split into two-component spinors of the form

$$U(\vec{p}) = \begin{bmatrix} U_h \\ U_l \end{bmatrix} \tag{3.25}$$

Plugging $U(\vec{p})$ into the Dirac equation (3.24), we find

$$\varepsilon U_h = c(\vec{\sigma}\cdot\vec{p})U_l + mc^2 U_h \tag{3.26}$$

and

$$\varepsilon U_l = c(\vec{\sigma}\cdot\vec{p})U_h + mc^2 U_l \tag{3.27}$$

These two equations can be solved to yield

$$\varepsilon = \pm(c^2p^2 + m^2c^4)^{1/2} = \pm E \tag{3.28}$$

This result validates the existence of negative-energy states in the Dirac equation. Since the Dirac equation must satisfy the Klein-Gordon equation, this result is not surprising. For a given $\vec{p}$, there are four possible solutions: two positive energy spin states and two negative energy spin states. The consequences will be discussed below.

3.3 Hole Theory

From equation (3.28), we see that for free-particles, the allowed energies extend from $+mc^2$ to $+\infty$ and from $-mc^2$ to $-\infty$. The negative energy states create the possibility that positive energy electrons could jump to negative energies, leading to a resultant negative infinite energy of the system. This is obviously not physical and was resolved by Dirac in his "hole theory". He proposed that in vacuum the positive energy states are all empty, but the negative energy states are all filled by electrons of *negative energy*. Thus, it becomes possible for a *negative energy* electron to absorb a photon and be excited to a *positive energy* state! This leads to an electron of charge $-e$ and energy $+E$ and a "hole" in the negative energy state. This hole refers to the absence of an electron with charge $-e$ and energy $-E$ which is observed as an positron of charge $+e$ and energy $+E$. This is pair creation. In the reverse, the hole can trap *positive energy* electrons. In this case, the electron goes from energy $+E$ to $-E$, and a photon of energy $2E$ is emitted. This is pair annihilation [23].

3.4 Positron Production

Equation (3.28) sets a lower energy limit of $2mc^2$ for pair creation. This energy can come from a photon or a collision with a particle of kinetic energy greater than $2mc^2$. However, in order for momentum and energy to be conserved, another particle must be present (generally an atomic nucleus). Thus, pairs are created by γ-photons or relativistic particles in matter [25]. In this section, only the γ-photon case will be discussed.

Momentum and energy must be conserved in pair production. Figure 3.1 shows a schematic of the pair production geometry considered by Motz [1]. Energy conservation gives

$$k = (T_+ + 1) + (T_- + 1) + T_r \tag{3.29}$$

where k is the incident photon energy, T_+ and T_- are the positron and electron kinetic energy, respectively, and T_r is the recoil energy of the extra particle (nucleus, in our case). All energies are normalized by $m_e c^2$. For momentum conservation, we find

$$\vec{k} = \vec{p}_+ + \vec{p}_- + \vec{q} \tag{3.30}$$

where $\vec{k}$ is the incident photon momentum, $\vec{p}_+$ and $\vec{p}_-$ are the positron and electron

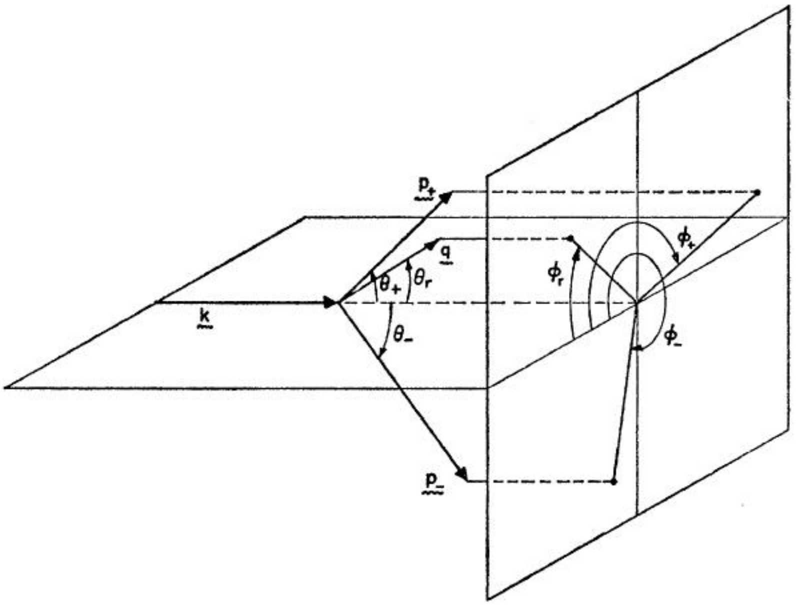

Figure 3.1: Schematic of pair production geometry [1].

momenta, respectively, and $\vec{q}$ is the recoil momentum of the particle involved (nuclei or electron). All momenta are normalized by $m_e c$. From equation 3.30 and figure 3.1, the momentum balance is

$$q^2 = k^2+p_+^2+p_-^2+2p_+p_-[cos\theta_+cos\theta_-+sin\theta_+sin\theta_-cos(\phi_+-\phi_-)]-2p_+kcos\theta_+-2p_-kcos\theta_- \tag{3.31}$$

From equation 3.28, the recoil energy is

$$E_r = \sqrt{q^2 + \frac{m_r^2}{m_e^2}} - \frac{m_r}{m_e} \tag{3.32}$$

where m_r is the mass of the recoiling nucleus, and m_e is the mass of the electron. The minimum recoil momentum is found from equation (3.31) when $\theta_+ = \theta_- = 0$. Plugging this result into equation (3.32) gives

$$k + \frac{m_r}{m_e} = (T_+ + 1) + (T_- + 1) + \sqrt{q_{min}^2 + \frac{m_r^2}{m_e^2}} \tag{3.33}$$

It is clear that the absolute minimum occurs when the electron and positron energies are equal, $T_+ = T_-$. For the nuclear case ($m_r \gg m_e$), we find

$$q_{min} = k - (k^2 - 4)^{1/2} \tag{3.34}$$

The minimum recoil momentum for a given positron momentum, $q_{min}(\vec{p}_+)$, can

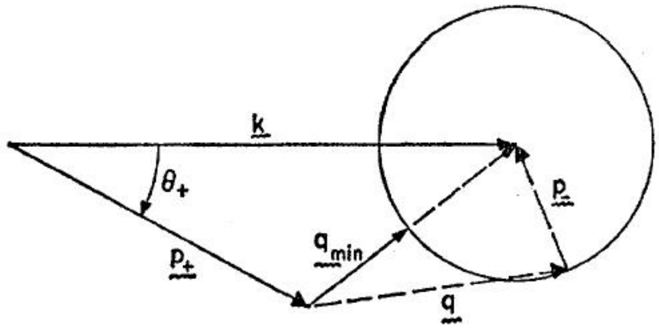

Figure 3.2: Vector diagram of momentum balance for pair production [1].

be shown to occur when the electron momentum, $\vec{p}_-$ is parallel to and lies in the same plane as q, $\phi_r = \phi_+ = \phi_-$. This is illustrated in Figure 3.2.

3.5 Pair Production Cross-Section and Screening

The minimum momentum transfer to the recoiling nucleus is related to the maximum impact parameter [25], r_{max}, by the equation

$$r_{max} = 1/q_{min}(\vec{p}_+) \tag{3.35}$$

The maximum impact parameter determines an effect known as screening. If r_{max} is larger than the radius of the atom, the outer electrons will "screen" the nuclear field, making the Coulomb collision between the pairs and the nucleus small, resulting in a small recoil momentum for the nucleus. This decreases the pair production cross-section dramatically, as will be shown below.

The screening parameter, μ, is

$$\mu = \frac{100}{k} \frac{1}{\nu(1-\nu)Z^{1/3}} \tag{3.36}$$

where $\nu = E_+/k$ and E_+ and E_- are the total (KE+PE) positron and electron energies, respectively [26]. If $\mu >> 1$, screening is negligible, but screening becomes important if $\mu \leq 1$. "Complete screening" occurs when $\mu = 0$.

The Bethe-Heitler cross-section, $\frac{d\sigma}{dE_+}(k, E_+)$, is defined as the probability of producing a positron of energy between (E_+) and $(E_+ + dE_+)$ from a photon of energy

k. The Bethe-Heitler formulas for a screened point-nucleus with extreme relativistic energies ($k \gg m_e c^2$) are [27]

$$\frac{d\sigma}{dE_+}(k, E_+) = \frac{4Z^2 r_e^2}{137k^3} G(k, \mu) \tag{3.37}$$

with $G(k, \mu)$ defined by the following:

1) No screening ($\mu \gg 1$)

$$G(k, \mu) = \left[E_+^2 + E_-^2 + \frac{2}{3}E_+E_-\right]\left[ln\left(\frac{2E_+E_-}{k}\right) - \frac{1}{2}\right] \tag{3.38}$$

2) Complete Screening ($\mu \approx 0$)

$$G(k, \mu) = \left[E_+^2 + E_-^2 + \frac{2}{3}E_+E_-\right] ln\left(\frac{183}{Z^{1/3}}\right) - \frac{1}{9}E_+E_- \tag{3.39}$$

3) Intermediate Screening ($0 < \mu < 2$)

$$G(k, \mu) = (E_+^2 + E_-^2)\left[\frac{\Phi_1(\mu)}{4} - \frac{1}{3}lnZ\right] + \frac{2}{3}E_+E_-\left[\frac{\Phi_2(\mu)}{4} - \frac{1}{3}lnZ\right] \tag{3.40}$$

4) ($2 < \mu < 15$)

$$G(k, \mu) = \left[E_+^2 + E_-^2 + \frac{2}{3}E_+E_-\right]\left[ln\left(\frac{2E_+E_-}{k}\right) - \frac{1}{2} - c(\mu)\right] \tag{3.41}$$

where $\Phi_1(\mu)$ and $\Phi_2(\mu)$ are determined by the following analytical expressions [28]. The variable G is defined as

$$G = \frac{136}{k}\frac{1}{\nu(1-\nu)Z^{1/3}} \tag{3.42}$$

For $G \leq 1$, we find

$$\Phi_1(\mu) = 20.868 - 3.242G + 0.625G^2 \tag{3.43}$$

$$\Phi_2(\mu) = 20.209 - 1.930G + 0.086G^2 \tag{3.44}$$

and for $G > 1$, we find

$$\Phi_1(\mu) = 21.12 - 4.184ln(G + .952) \tag{3.45}$$

$$\Phi_2(\mu) = \Phi_1(\mu) \tag{3.46}$$

$c(\mu)$ is evaluated from Figure 3.3.

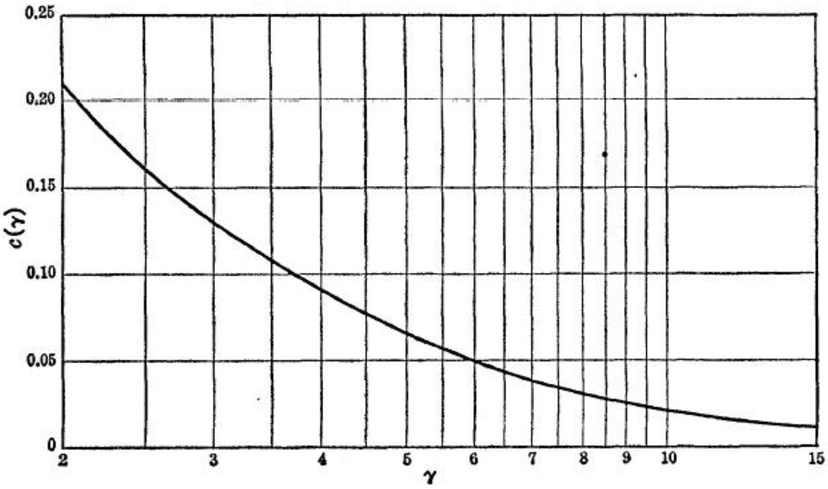

Figure 3.3: Function $c(\mu)$ for the Bethe-Heitler cross-section [2].

Equations (3.38)-(3.41) are plotted for various energies in Figure 3.4a. This plot defines the probability of producing a pair with the positron-to-incident photon energy ratio of E_+/k. At low energies, the probability for each energy ratio is roughly equal from $k = 0.2E_+ - 0.8E_+$. The probability for equal positron and electron energies decreases as the energy increases. As $k \to \infty$, antisymmetric energy distributions dominate.

Figure 3.4b plots the cross-section only on the vertical axis. This validates the scaling laws dictated by equation (3.36). As k increases, the screening parameter μ decreases. For a given $\nu = E_+/k$, screening is more prevalent as k increases. Thus, the cross-section for a given ν also decreases. If the curves in Figure 3.4b are integrated over energy, the result in tabulated in table 3.1. As k increases, the cross-section for a given ν decreases, but the total integrated cross-section increases.

For an ideal positron source for high energy physics applications, positrons in the energy range of $E_+ = 5 - 30MeV$ are optimal. They have a high enough energy to escape the target, but have a low enough energy to be collected so that they can be further accelerated with a narrow energy spread using a linear accelerator [7]. For the photon energy distributions of the X-ray betatron radiation (10-100 MeV), the probabilities are roughly equal for most energy ratios E_+/k as seen in Figure 3.4. This has important implications for a positron source. It states that a monochro-

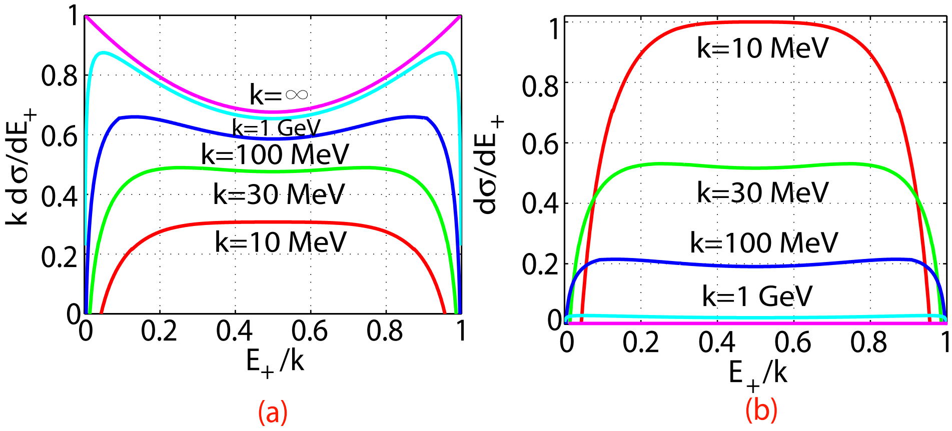

Figure 3.4: The Bethe-Heitler cross-section from Equations (3.38)-(3.41) for Tungsten. X-axis is the ratio of the positron energy, E_+, to the incident photon energy, k. (a) Y-axis is the Bethe-Heitler cross section, $d\sigma/dE_+$, multiplied by the incident photon energy, k, in MeV. (b) Y-axis is only the Bethe-Heitler cross-section, $d\sigma/dE_+$.

k (MeV)	Total Relative Cross-Section
10	.3061
30	.5536
100	.7640
1000	.9485
∞	1.000

Table 3.1: The total integrated Bethe-Heitler Cross-Section for the k values plotted in Figures 3.4a and 3.4b.

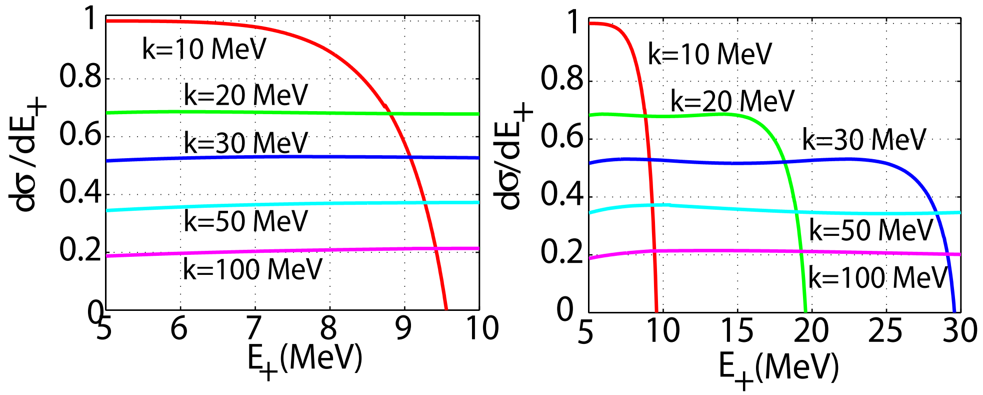

(a)

(b)

Figure 3.5: The Bethe-Heitler cross-section from Equations (3.38)-(3.41) for Tungsten. Y-axis is the Bethe-Heitler cross section, $d\sigma/dE_+$. X-axis is the positron energy, E_+ for (a) 5-10 MeV and (b) 5-30 MeV.

matic magnetic undulator source ($K_u \approx 1$) is not necessarily any more efficient than a broadband source of betatron X-rays from a plasma wiggler ($K_w \gg 1$) for the energies of interest. Figure 3.5a shows that if you begin with the same number of incident photons over all energies, a 10 MeV source from a low-K magnetic undulator will have a larger positron yield in the range of 5-10 MeV than a broadband photon source from 10-100 MeV . However, if you include all positrons from 5-30 MeV, the yield increases substantially for the broadband case. Relative theoretical calculations for the total integrated cross section from a given energy range are shown in Table 3.2. As long as the thermal stress on the target does not lead to failure, the broadband source appears to give a better yield to zeroth-order. An end-to-end betatron source will be designed in a later chapter and will take divergence angle and collection efficiency into account.

k (MeV)	Total Relative CS (*5-10 MeV*)	Total Relative CS (*5-30 MeV*)
10	1.000	1.000
20	.8761	2.389
30	.6773	3.154
50	.4677	2.270
100	.2623	1.341

Table 3.2: The total integrated Bethe-Heitler Cross-Section (CS) for the k values plotted in Figures 3.5a and 3.5b.

CHAPTER 4

Experimental Setup and Diagnostics

The experimental work described in this thesis was carried out parasitically to two major experiments on Plasma Wakefield Acceleraion (PWFA), E-164 and E-164X, at the Stanford Linear Accelerator Center (SLAC). As such, the beam and plasma parameters were not optimized for generating the maximum possible positron yield as shall be presented later. Therefore, the experimental results obtained here should be regarded as a demonstration of a proof-of-principle concept of this scheme. For details of the PWFA experiment, the reader is referred to references [4, 20, 29].

The E-164 and E-164X experiments at the Stanford Linear Accelerator Center (SLAC) had a large number of experimental diagnostics. Here we discuss each diagnostic and its relevance to the experiment. The first half of this chapter will discuss the group diagnostics used by both the acceleration experiment and the positron experiment, and the second half will discuss the diagnostics used solely for the positron experiment.

4.1 Plasma Wakefield Experimental Diagnostics

The setup for the Plasma Wakefield experiment is shown in Figure 4.1. An electron beam of $\sim N_b = 1.8 \times 10^{10}$ electrons with a $\sigma_z = 20 - 50\mu m$ is created in the accelerator and sent into the FFTB. The electron beam is dispersed in energy and sent through a series of dipole magnets causing the electrons to radiate X-rays in the keV range. These X-rays are used to determine the energy spectrum of the beam entering the plasma. After this, the beam propagates through a $1\mu m$ Ti foil. The Coherent Transition Radiation (CTR) emitted from the foil is detected using pyroelectric detectors. This is used as a relative bunch-length measurement. The

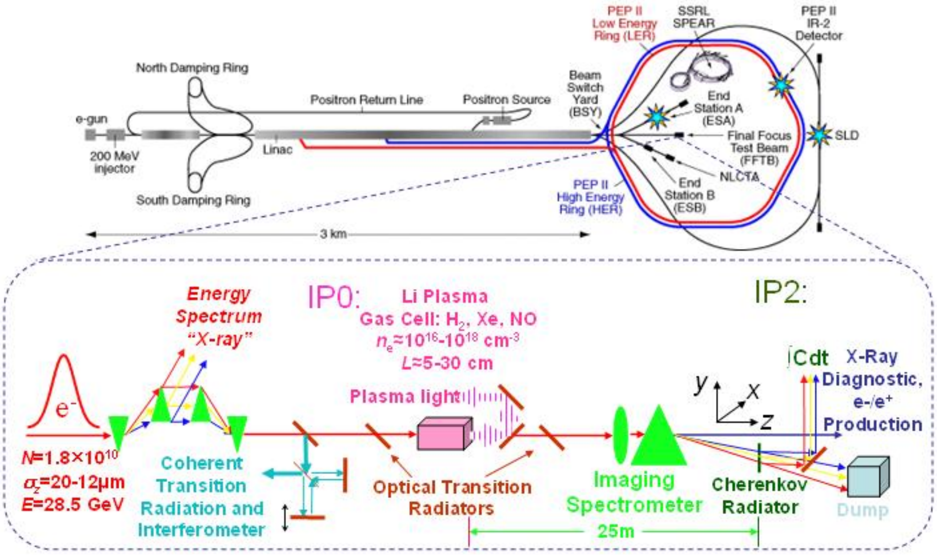
PEP II Low Energy Ring (LER)
SSRL SPEAR
PEP II IR-2 Detector
North Damping Ring
Beam Switch Yard (BSY)
Positron Return Line
Positron Source
End Station A (ESA)
e-gun
Final Focus Test Beam (FFTB)
SLD
200 MeV injector
Linac
NLCTA
End Station B (ESB)
PEP II High Energy Ring (HER)
South Damping Ring
3 km
Energy Spectrum "X-ray"
IP0:
Li Plasma
Gas Cell: H2, Xe, NO
ne≈10¹⁶-10¹⁸ cm⁻³
L≈5-30 cm
IP2:
Cdt
X-Ray Diagnostic, e-/e+ Production
Plasma light
y
x
z
e-
N=1.8×10¹⁰
σz=20-12μm
E=28.5 GeV
Coherent Transition Radiation and Interferometer
Optical Transition Radiators
Imaging Spectrometer
Cherenkov Radiator
Dump
25m

Figure 4.1: E-164/E-164X/E-167 Experimental Schematic

beam is focused using two quadrupoles immediately upstream of the plasma. After the focusing magnets, the beam propagates through another $1\mu m$ Ti foil. Here, the Optical Transition Radiation (OTR) created from the beam interaction with the foil is detected. The beam focuses into the plasma with an approximate waist size of $\sigma_r = 10\mu m$. The plasma source was generally (Li) with a variable length of $6 - 30cm$ and a variable density from $n_{pe} = 1 - 30 \times 10^{16} cm^{-3}$ [30]. The optical recombination light emitted as the plasma relaxes back to a neutral gas is extracted using another $1\mu m$ Ti foil downstream of the plasma. This light is collected in an imaging spectrometer. The electron beam at the exit of the plasma is imaged to the Cherenkov radiator, 25m downstream, using a series of quadrupoles, and it is dispersed in energy using permanent dipole magnets. The Cherenkov diagnostic is the main diagnostic for energy gain in the experiment. The betatron X-rays radiated as the beam electrons oscillate within the plasma are sent 40m downstream and collide with a 1.7mm W target to create electron/positron pairs.

4.1.1 X-ray Spectrometer

The first diagnostic in Figure 4.1 is the X-ray spectrometer. This device was modified from an earlier design that was implemented on the SLC experiments at SLAC [31]. The schematic of the device is shown in Figure 4.2a. The wiggler magnet was

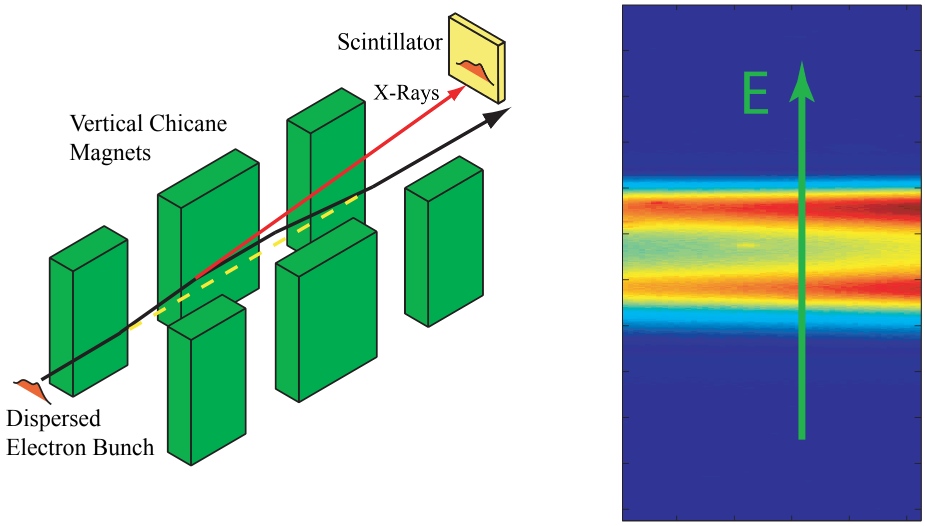

(a) (b)

Figure 4.2: (a) Schematic of the X-ray Chicane. (b) Example of a data image from the X-ray Spectrometer.

installed in a region of horizontal dispersion in the FFTB. At this location, the beam is sent through a 1/2 betatron period wiggler magnet. The beam betatron motion is not large enough to effect the emittance of the beam. However, the motion does cause the electrons to radiate X-rays with a critical energy in the range of 200-400 keV[1]. The X-rays collide with a Ce:YAG scintillating crystal, and the resulting optical light is imaged to a Photometrics Sensys 12-bit CCD camera. Due to the horizontal dispersion of the incident electron beam, the resulting camera image shows the beam energy as a function of position, and the relative intensity at each position determines the number of beam electrons at that specific energy. A typical X-ray spectrometer image is shown in Figure 4.2b.

The camera resolution for this diagnostic is roughly 5.5 MeV/pixel. However, at the location of the wiggler magnet, the electron beam is not at a transverse betatron focus. Thus, there is a bit of energy smearing across the camera image. For data analysis, an average is taken over 10 pixels, resulting in an total energy resolution of 55 MeV [3].

---

[1] The magnetic field varies longitudinally. This accounts for the range of critical energies.

The energy spectrum of the electron beam measured from this diagnostic is fitted to one computed in LITRACK to obtain the γ versus z and I versus z beam phase space distributions such as that shown in figure 2.9a in chapter 2.

4.1.2 Optical Transition Radiation

Transition Radiation occurs when a charge moves from a medium of one dielectric constant (ϵ_1) to a medium of another dielectric constant (ϵ_2). Inside each media, the charge has certain fields associated with its velocity and the properties of the individual media. However, as the particle approaches and crosses into the second media, the fields shift and release radiation known as "Transition Radiation" [15].

For normal incidence relative to the boundary plane, the radiated energy W of a single electron into the backward direction at an angle θ with respect to the path of the particle is [32]

$$\frac{d^2W}{d\omega d\Omega} = \frac{r_e m_e c\beta^2}{\pi^2}\sqrt{\epsilon_1} sin^2\theta cos^2\theta \frac{F_n^2}{F_d^2} \tag{4.1}$$

where

$$F_n = (\epsilon_2 - \epsilon_1)(1 - \beta^2\epsilon_1 + \beta\sqrt{\epsilon_2 - \epsilon_1 sin^2\theta}) \tag{4.2}$$

and

$$F_d = (1 - \beta^2\epsilon_1 cos^2\theta)(1 + \beta\sqrt{\epsilon_2 - \epsilon_1 sin^2\theta})(\epsilon_2 cos\theta + \sqrt{\epsilon_1\epsilon_2 - \epsilon_1^2 sin^2\theta}) \tag{4.3}$$

For our case, with a 28.5 GeV electron beam traversing from a low density He buffer gas to a 1μm Ti foil, the following assumptions are made to Equation (4.1): $\epsilon_1 = 1$, $\epsilon_2 = \infty$, $sin\theta = \theta$, $\beta = 1$, and $cos\theta = 1$. These reduce Equation (4.1) to

$$\frac{d^2W}{d\omega d\Omega} = \frac{r_e m_e c}{\pi^2}\frac{\theta^2}{(1 - \beta^2 cos^2\theta)^2} \tag{4.4}$$

Integration over solid angle Ω gives the radiated energy per unit frequency

$$\frac{d^2W}{d\omega} \approx \frac{2r_e m_e c}{\pi\beta} ln(\gamma) \tag{4.5}$$

It is interesting to note that the radiated energy per frequency is independent of frequency for the case of a vacuum medium entering a perfectly conducting metal.

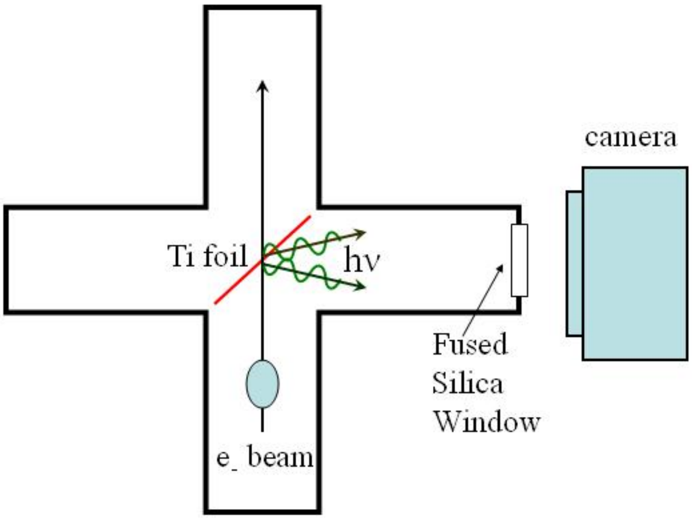

Figure 4.3: Schematic of the OTR setup

Optical Transition Radiation (OTR) is a powerful diagnostic that is used to document the transverse profile of the electron beam as it transports through the experiment. For a beam of electrons in the optical regime, the electron bunch length ($\approx 25\mu m$) is far longer than the optical radiation. Thus, the radiation is incoherent and the total radiation from a beam of electrons can be determined by simply multiplying the single electron case by the number of particles in the bunch.

The OTR foils were placed immediately upstream and downstream of the plasma. The 1 μm Ti OTR foil is set at 45^o relative to the beam axis as seen in Figure 4.3. This allows for the extraction of the OTR light. The light exits the vacuum chamber through a fused silica window, and the light is detected using a Photometrics Sensys 12-bit CCD camera with a pixel size is 9x9 μm and total array of 768x512.. A Nikon AF Micro-Nikkor lens was used, and it was set in 1:1 imaging mode to allow for the best possible resolution.

4.1.3 Coherent Transition Radiation

In principal, this diagnostic is similar to the optical transition radiation diagnostic in the sense that they both involve ”Transition Radiation”. There is one major difference. When the radiation wavelength is small in comparison to the bunch length, as is the case for optical transition radiation, the fields of the radiated

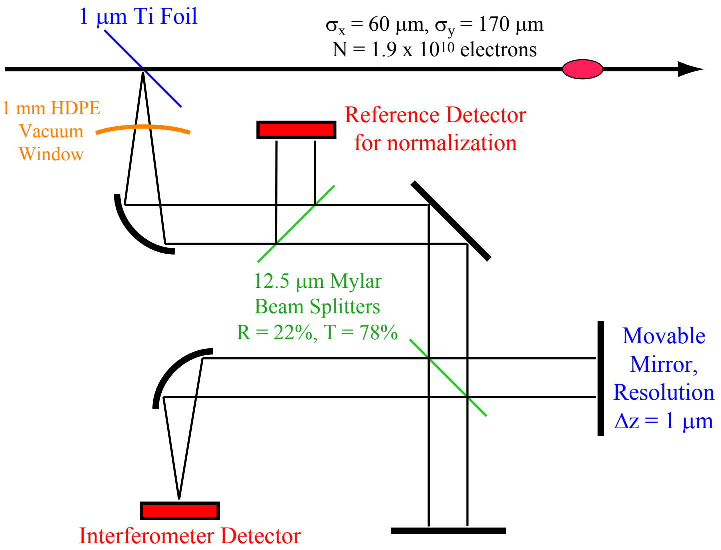
1 μm Ti Foil
σx = 60 μm, σy = 170 μm
N = 1.9 x 10¹⁰ electrons
1 mm HDPE Vacuum Window
Reference Detector for normalization
12.5 μm Mylar Beam Splitters R = 22%, T = 78%
Movable Mirror, Resolution Δz = 1 μm
Interferometer Detector

Figure 4.4: Schematic of the CTR setup

photons add incoherently. However, at wavelengths where the transition radiation is longer than the bunch length, the fields of the radiated photons add coherently, and a beam of electrons will emit an intensity that is proportional to the square of the number of particles.

Coherent transition radiation (CTR) can be used to measure the bunch length [33, 34]. The schematic for our experiment is shown in Figure 4.4. The CTR is created as the beam transports through a 1 μm Ti foil set at 45^o relative to the beam axis. It exits the beam line through a 12.5 μm Mylar window. The beam is collected by a gold-plated off-axis parabolic mirror. A 12.5 μm Mylar foil with 22 percent reflectance and 78 percent transmittance is used as a beam splitter to extract a reference beam. The reference beam is used as a normalization of the total signal. The remaining CTR enters a Michelson-Morley interferometer containing another 12.5 μm Mylar beamsplitter. An autocorrelation is taken over many shots. The signal gives information about the bunch length and shape. The ultra-short bunch lengths produced at SLAC have been measured. The autocorrelation trace showed a weak dependence on bunch length in the region of $\sigma_z = 20\mu m$ [34]. The CTR is detected using Molectron P1-45-CC pyroelectric detectors.

In the future, there are plans to implement a new design that will allow for single-shot autocorrelations, thus reducing errors due to shot-to-shot variations in

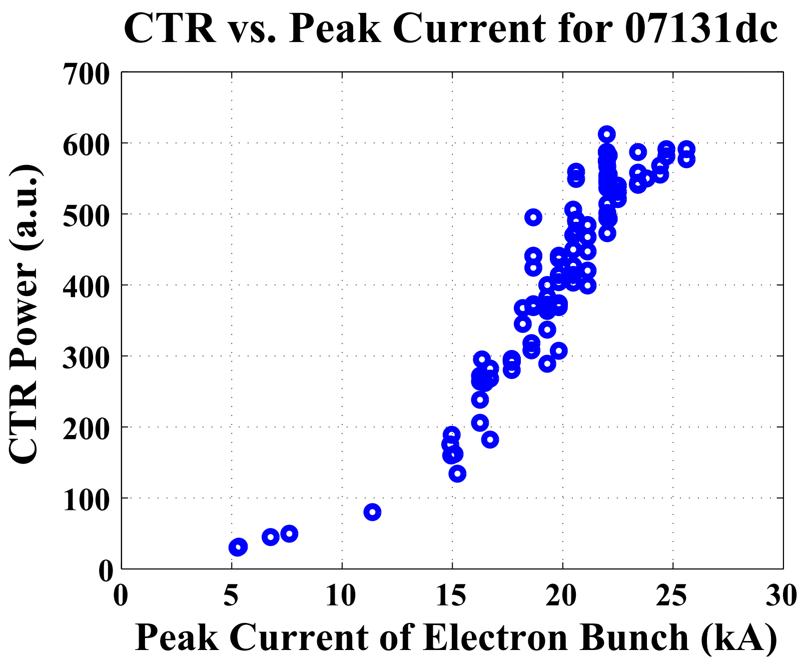

Figure 4.5: Plot showing the correlation of the pyro signal to the peak current of the bunch as determined by the X-ray spectrometer [3].

the electron beam. Also, material tests have shown that a Silicon window will serve as a better transmitting medium than the Mylar. This will produce more accurate autocorrelation signals that have less etalon filtering and material absorption effects [35].

It is known that for a Gaussian bunch with a fixed number of electrons, the CTR energy scales as $1/\sigma_z$. Thus, even without the autocorrelator, the CTR offers a great relative bunch length measurement which utilizes the reference beam extracted upstream of the Michelson interferometer. When the electron bunch is at peak compression, the pyro signal is maximized. The pyro signal has been shown to correlate with the wakefields created in the linac, and it correlates with the peak current determined from the X-ray spectrometer as shown in Figure 4.5.

4.1.4 Focusing Optics

The FFTB optics are set to create small electron beam spot sizes at the entrance of the Li vapor oven. Figure 4.4 shows a schematic of the waist location change in one transverse plane. By adjusting the focusing strength of the quadrupoles

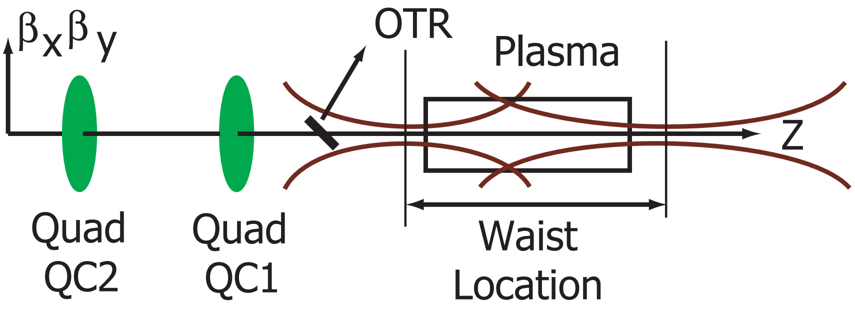

Figure 4.6: Schematic of the focusing setup of the FFTB at IP0, immediately upstream of the plasma entrance. [4].

QC1 and QC2 located about 170 cm and 300 cm upstream of the plasma entrance, respectively, the waist position within the individual transverse planes could be altered. Moving the waist led to a different beam size (i.e. beam density) at the fixed location of the plasma entrance.

The beam spot sizes for this experiment were measured using wire scanners at the location of the plasma entrance before the Li oven was placed in the FFTB beamline. The electron beam spot sizes were measured at $\sim \sigma_{x,y} = 10\mu m$ at the plasma entrance. These numbers have a large effect on the ultimate positron yield which will be discussed in Chapter 5.

An important note is that $\beta_y \approx 7\beta_x$ in our experiment. Thus, small waist position changes in X, create large beam density changes at the plasma entrance. However, due to $\beta_y >> \beta_x$, the waist position changes in Y have little effect on the beam density at the plasma entrance. Thus, the data that addresses the positron yield as a function of waist position is only performed by changing the X focusing conditions.

4.1.5 Lithium (Li) Oven for Plasma Medium

The plasma used in this experiment is a singly-ionized Li vapor of variable length of $L_p = 6 - 30cm$ and variable neutral density $n_n = 1 - 30 \times 10^{16} cm^{-3}$. Lithium is a perfect gas for the experiment as it has a low ionization potential of 5.4 eV for the first electron and a high ionization potential of 75 eV for the second electron. Thus, the first electron can be easily ionized with a 192 nm (6.48 eV) UVB ArF laser or field ionized with the electric field of the electron beam with little chance of ionizing the second electron. Initially, a 100 mJ 192nm ArF laser was used to ionize the neutral Li vapor. However, the 100 mJ of energy available was only acceptable for densities $n_p < 4 \times 10^{16} cm^{-3}$. Beyond this, for the 10cm neutral vapor lengths used at that time, the laser beam would begin to lose fluence within the vapor, leading to a non-uniform plasma density, longitudinally. Thus, when the experiment moved to $n_p > 1 \times 10^{17} cm^{-3}$, field ionization was used to ionize the Li vapor.

It is important to understand the physics of the metal vapor oven [36]. This will provide pertinent information to understand the longitudinal profile of the plasma. Figure 4.7 shows a schematic of the Li vapor oven. The Li is containing inside a 1.5" stainless steel pipe, and is isolated from the FFTB vacuum using $75 \mu m$ Be windows on both sides of the assembly. A wire with a large resistance is wound around the 1.5" stainless steel pipe. When current is run through this wire, the Ohmic losses conduct heat into the Li solid inside the stainless pipe. Helium (He) acts as a buffer gas in the assembly. The pressure of the He is set to balance the pressure of the Li to keep the Li vapor at a fixed length within the assembly. Given a certain He pressure, the molten Li will begin to vaporize at a certain temperature at which the Li vapor pressure slightly exceeds the He pressure. The center of the oven vaporizes first, and the pressure gradient causes the Li vapor to diffuse outward in the pipe until it hits the cooler He gas. The collisions between the He and the Li efficiently transfer the heat and condense the Li vapor onto a stainless steel mesh, or wick, which runs longitudinally along the inner edge of the pipe. The condensed Li will move back toward the center of the oven on the wick through capillary action. Once the center is reached, the Li is again vaporized and the process starts again. When equilibrium is reached, the vaporized Li resides in the center of the heat-pipe oven with a given density and length. In the oven mode, when the Li and He pressures are in equilibrium, the Li density is determined solely by the pressure of the He buffer gas, and the length of the Li oven is determined by the current in the heater wire. The "buffer zone" in the entrance and exit region containing Li and He creates a ramped-neutral Li profile. This density ramp ultimately leads to focusing of the

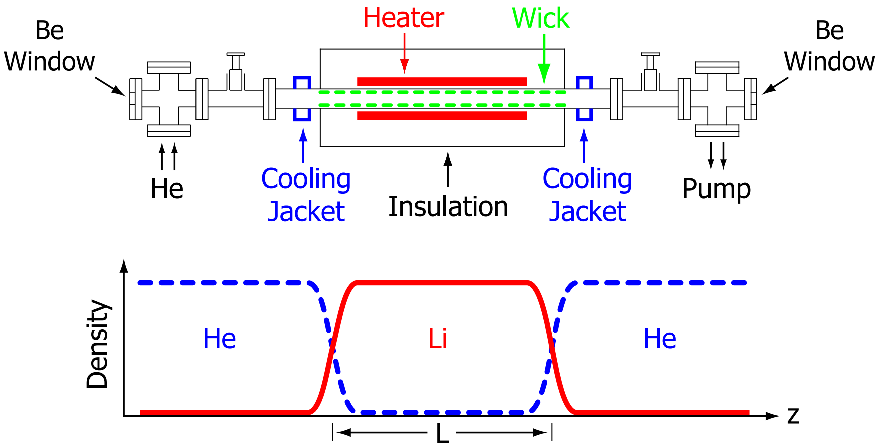

Figure 4.7: Schematic of the Li vapor oven. [3].

electron beam as the beam enters the ionized ramped profile region in the Li. Helium ionization is not of primary importance since the ionization potential of He is 25 eV. However, under certain circumstances, it can become important and produce an additional source of electrons.

The longitudinal temperature profile of the Li vapor $T_{Li}(z)$ was determined prior to the experiment by pulling a thermocouple through the oven. The conversion from temperature to pressure for the Li vapor in this regime where $T_{Li}(z) < 1000K$ was measured empirically by Alcock [37]. The conversion equation is

$$p = 760 * 10^{[5.055-(8023/T_{Li})]} \tag{4.6}$$

where p is the pressure in Torr and T is the temperature of the Li in Kelvin. The vapor density and the longitudinal profile are computed from the pressure using the ideal gas law. Figure 4.8 shows a plot of the measured oven profile (blue *) and a curve fit to the measured profile (green o). The curve fit is simply a flat top for a given length with gaussian edges for $3\sigma_z$ beginning at the entrance and exit of the flat region. The length of the plasma L_p is defined as the full-width at half maximum of the neutral density profile. The length of Figure 4.8 is roughly 11 cm. The curve-fitted oven profile is used to determine electron beam focusing within the ramped-density region of the Li using a beam-envelope model. This will be discussed further in the experimental results of Chapter 5.

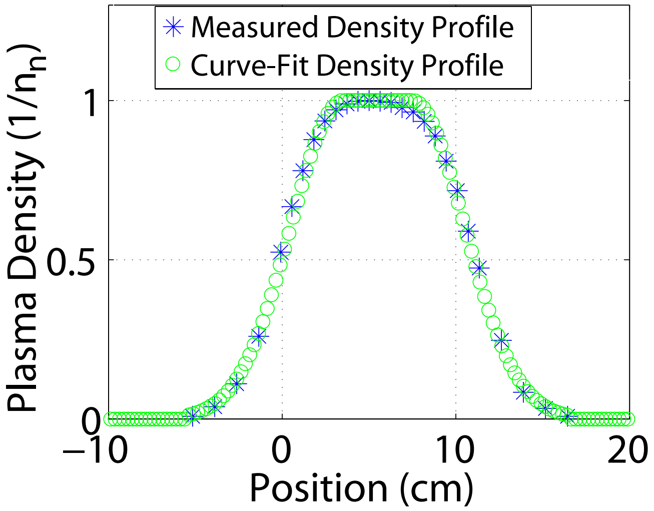

Figure 4.8: Plot showing the measured Li neutral density profile and the curve fit to the measured profile.

4.1.6 Cherenkov Diagnostic

The main diagnostic for the wakefield experiment was the Cherenkov diagnostic. As we shall present, it also provided critical information for the analysis of the positron experiment by giving a direct measurement for the number of electrons in the ion column. As shown in Figure 4.1, after the electron beam exited the plasma, the beam was sent through an imaging spectrometer which consisted of a collection of quadrupoles and dipole magnets. The dipole magnets dispersed the beam in the vertical plane upstream of the Cherenkov diagnostic, creating an energy spectrometer with a dispersion η_y of about 10.5cm. The Cherenkov medium was a 1mm aerogel located about 25 m downstream of the plasma. Since the beam electron velocity is greater than the speed of light in the aerogel, the beam electrons emit Cherenkov radiation. This radiation cone has an opening angle of roughly 7 degrees. A vertical slit of the Cherenkov light cone is intercepted with a mirror immediately downstream of the aerogel. The beam electrons do not contact the mirror. The corresponding light is imaged to a 16-bit Princeton Instruments VersArray CCD camera. The total path length of the Cherenkov light from the aerogel to the camera is roughly 1m. The camera is encased in lead to eliminate spurious signals

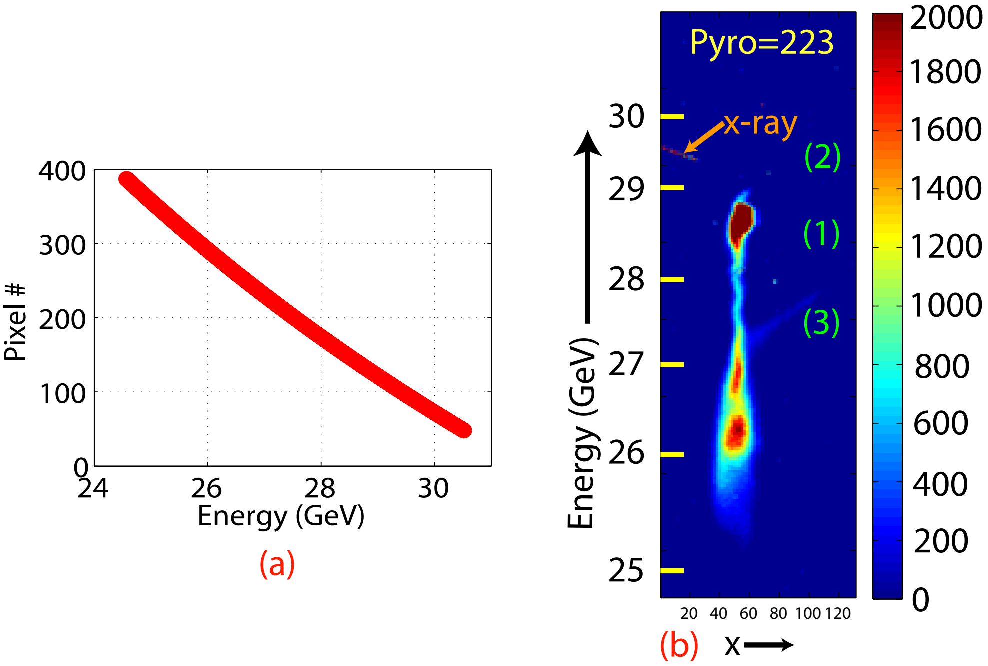

Figure 4.9: (a) Plot showing the calibration of energy/pixel on the Cherenkov diagnostic. (b) Example false-color image on the Cherenkov after the electron beam traversed through the plasma.

on the CCD chip due to the X-ray background in the FFTB.

The energy resolution ΔE of the Cherenkov spectrometer is found using the following equation

$$\Delta E = \frac{\Delta d}{\eta_y} E_o \tag{4.7}$$

where E_o is the energy of the electron, η_y is the dispersion in the vertical plane calculated at 10.5 cm, and Δd is the height of a pixel in the camera image. There are 14.4 pixels/mm giving a view of $\Delta d = 69.4\mu m$ for each pixel. With the dispersion of 10.5 cm, for a 28.5 GeV electron, there is an energy resolution of roughly 18.8 MeV/pixel. The calibration of the Cherenkov diagnostic is shown in Figure 4.9a, and Figure 4.9b gives an example of a Cherenkov image created by an electron beam that has traversed the Li plasma. The large energy spread is due to the energy loss that the electrons in the front of the beam incur when they drive the plasma wake. This wake has been measured to be as large as 40 GeV/m [20].

4.2 Positron Experimental Diagnostics

The second section of this chapter deals with the diagnostics that were developed solely for the positron experiment. Figure 4.10 shows a schematic of the positron experiment.

4.2.1 Photon Collimators

Betatron X-rays were radiated in the plasma of variable length with $L_p = 6 - 30cm$ and variable density $n_p = 1 - 30 \times 10^{16} cm^{-3}$. The X-ray beam travels downstream roughly 25 m where it hits the first of two tungsten (W) collimators. This collimator has a length of 10cm with a 6.35 mm (1/4") longitudinal aperture. The second collimator is 5 m downstream of the first with a length of 10 cm and a 12.7 mm (1/2") longitudinal aperture. These collimators were implemented since the experiment was performed 40m downstream of the plasma due to space constraints in the FFTB. The $\theta = K/\gamma$ divergence of the beam created large X-ray beam spot sizes at the positron experiment, contributing to large amounts of noise on the detectors. These two collimators mitigate this issue. The downstream collimator was encased in a 4" thick lead (Pb) wall with a surface area of roughly $1m^2$. This Pb wall would collect the noise created when the outer photons in the X-ray beam scattered off the first collimator. The result of this collimator setup was a 8mm photon beam at the positron target.

Since the entire photon beam could not be collected, an alignment procedure was performed to guarantee that we were centered on the X-ray photon beam. This method consisted of identifying the position of the peak X-ray signal in both transverse planes on a phosphor that was upstream of the positron target. This phosphor was imaged using an 8-bit Cohu-4900 CCD camera. Figure 4.11a shows an example of an image from this diagnostic. Figures 4.11b,c plot the horizontal and vertical lineouts of the image which clearly show that the peak phosphor signal is centered in the image in both planes.

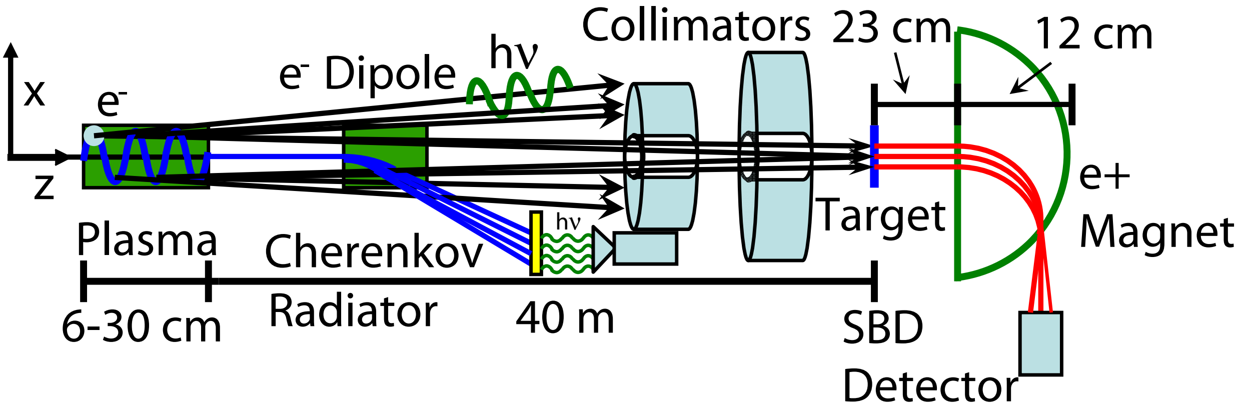
x
z
e-
e- Dipole
hν
Collimators
23 cm
12 cm
e+
Magnet
Target
Plasma
Cherenkov
Radiator
hν
6-30 cm
40 m
SBD
Detector

Figure 4.10: Schematic of the positron experimental setup.

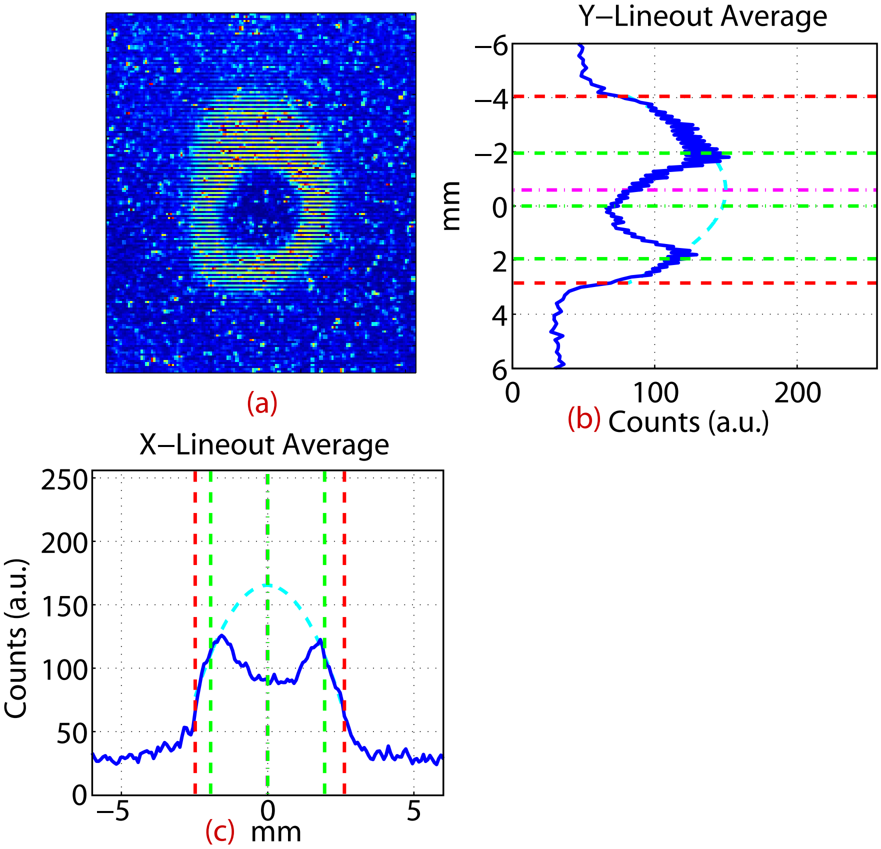

Figure 4.11: (a) Upstream phosphor image of 8mm collimated photon beam before collision with the positron target. A hole was cut in the TRIMAX phosphor to allow a He-Ne laser to propagate through for experimental alignment. (b) X-Lineout of the image. (c) Y-lineout of the image.

4.2.2 Target

A variety of convertor targets were tested in this experiment. EGS4 simulations show that the peak positron yield escaping the target occurs at roughly .5 radiation lengths (X_o). Thus, we chose to use roughly .5X_o of W which equates to a thickness of 1.7mm.

For thin target sources, there have been many studies performed which recommend the use of a low-Z material like Titanium (Ti) for the positron target in a thin target source. The reason being that at thicknesses $< X_o$ the yield tends to be largely material independent [7], but since Ti has a higher heat capacity than W, a Ti target can absorb a higher flux of heat before failure. In the experiment, we used .5X_o of Pb and Ti, along with W. No change in yield was measured. The data presented used the W target, but from the above observation, one can be certain that the results with Ti would have been roughly the same.

The target was placed on a target wheel that could be moved remotely during the experiment. This allowed us to change the target and to remove the target altogether while the beam was running in the FFTB. This allowed for target comparisons and signal-to-noise measurements.

4.2.3 Positron Spectrometer Magnet

Two spectrometer setups were used over the many runs that made up this experiment. The first example given is the spectrometer setup where the majority of the data was taken. The second setup used will be discussed briefly at the conclusion of this section.

For the first spectrometer configuration, the positrons emanating from the rear of the target were imaged in a magnetic spectrometer with an aperture of roughly 3.2cm by 1.2cm. The semi-circular magnet pole pieces were centered using a Helium-Neon laser which was aligned to the X-ray beam vector using X-ray phosphor images immediately upstream and downstream of the positron experimental table. Figure 4.12a shows a schematic of the dipole magnet imaging condition. The object plane

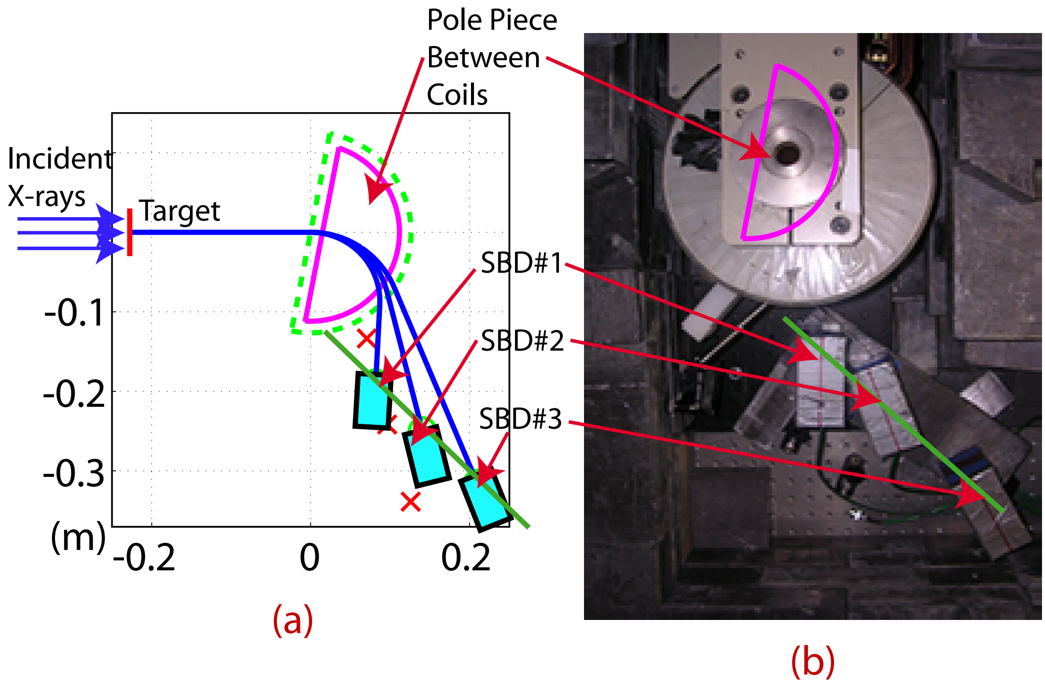

Figure 4.12: (a) Schematic of dipole imaging system for positron spectroscopy. Detectors are located in the Vertical Focal Plane of the positrons to maximize signal. The red x's plot the energy image plane. The 11 degree pole face rotation creates extra vertical focusing. (b) Photo of the region.

was 22.76 cm, and the 11 degree pole face rotation was set to allow for extra vertical focusing to maximize the positron signal. The stigmatic focus was set at a deflection angle of 93 degrees relative to the X-ray beam vector. The red x's in the figure represent the energy image plane. However, we opted to maximize signal instead of maximizing energy resolution. Thus, all three detectors were placed in the vertical focal plane of the spectrometer. The detectors used were 1 mm thick p-type Silicon Surface-Barrier detectors (SBD) with surface areas of $49mm^2$ biased to around -400 V. Three SBDs were placed at angles of 93 (SBD 1), 73 (SBD 2) and 63 (SBD 3) degrees. SBD 1 was periodically moved and replaced with a phosphor with a Xybion-750 intensified camera. The Xybion could verify the location of the positron image plane. Thus, we knew that our vertical positioning of the detectors was correct.

Using a pole gap of 24.4mm, the magnet was capable of producing a uniform 0.68 T magnetic field with 45 Amps of input current. The measured calibration of the magnet for the given pole pieces and gap is shown in Figure 4.13. This peak

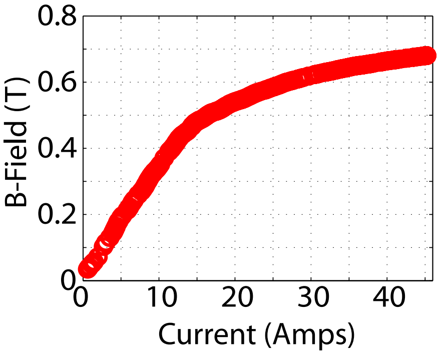

Figure 4.13: Magnet Calibration of B-field (T) versus current (A) with the semi–circular pole pieces and a pole gap of 24.4mm.

magnetic field and imaging condition allowed us to image particles to 17 MeV, 19 MeV, and 21 MeV with SBD 1, SBD 2, and SBD 3, respectively.

The signal on the SBDs is in units of counts d_c. In order to convert d_c to a spectrum, it must be divided by the energy spread on the detector ΔE. Equation 4.7 gives the relation $[\Delta E = (\Delta d/\eta)E_o]$. As the magnetic field is changed, the central energy E_o on each detector also changes. However, the dispersion and the width of the detector Δd remains the same. The dispersion at the three detector positions was 29.4 cm, 36.8 cm and 47.0 cm for the 93 degree (SBD 1), 73 degree (SBD 2) and 63 degree (SBD 3) detectors, respectively, and $\Delta d = 0.7cm$. Thus, as the central energy on the detector increased, the energy spread on the detector also increased, reducing the spectral value relative to a lower energy with the same d_c.

For the final run, we attempted to image higher energy particles by changing the imaging condition. In this imaging condition, the stigmatic focus was set at 84 degrees with detectors at 84 degrees, 59 degrees and 49 degrees. The object plane in this case was 35.73 cm and the magnet pole gap was decreased to 1.27 cm to maximize the magnetic field. The peak magnetic field at 45 Amps was .84 T which gave peak detector energies of 22 MeV, 30 MeV, and 35 MeV for the 84 degree, 59 degree and 49 degree detectors, respectively. The dispersion for these detectors was 26.2 cm, 35.9 cm, and 49.9 cm, respectively. The issue for this setup was signal-to-noise. Since the object and image planes were far longer than the previous setup and the pole gap was half its previous value, the collection efficiency was far lower.

The signal-to-noise was about 10 to 1 in the initial setup. However, in the latter setup, the signal-to-noise ratio was only 3 to 1. Thus, most of the data presented in chapter 5 is from the initial setup above.

4.2.4 Noise Reduction

Noise was a large issue in the FFTB since the SBDs absorb keV X-rays. To mitigate the noise, several shielding techniques were implemented. There was a 4" thick PB hut around the magnet and detectors on the positron experimental table to eliminate the potential of noise from X-ray radiation created in the FFTB. The three detectors were in 2" by 4" by 4" Pb casings to reduce noise created inside the PB hut as shown in Figure 4.10b. The Pb detector casings had a 3/4" hole drilled through the 4" length to allow for the placing of the SBDs. Lead will absorb X-rays only. Charged particles hitting the Pb will create large numbers of keV X-rays. Thus, the inner walls of the hut were lined with 1" of polyethylene. This plastic absorbed stray electrons and positrons created inside the hut before they interacted with the PB walls. These techniques cut the noise in the experiment substantially. From the initial setup, before these noise reduction techniques were utilized, the detectors would saturate at all magnetic field settings. However, the signal-to-noise ratio was roughly 10-to-1 after the noise reduction techniques were implemented. This was measured with the target in with the magnet on relative to the target out with the magnet on. When the magnet was turned off, the signal went to zero. The inner faces of the magnet pole gap were lined with 1/8" plastic to reduce the noise created when electrons and positrons hit the inner pole faces. This is the reason that the ultimate gap was only 12mm as opposed to the 24.4mm stated above. This issue was particularly important to mitigate as noise created when electrons and positrons hit the inner pole faces had a direct line-of-sight to the detectors.

4.2.5 Signal Detection and Calibration

The energy deposition per unit length in Silicon is a known quantity. The value is $\sim 500keV/mm$. Thus, the maximum energy deposited per mm in the silicon chip of the SBD detectors is about 500 keV. These detectors act as positron counters, meaning that any positron above 500 keV will give the same signal. The SBD signals were input into an Ortec 113 preamplifier and sent in RG-58, 50 Ohm BNC cables about 100 m to a 12-bit charge-integrating Philips 6100 Gated Analog-to-Digital convertor (ADC) with a calibration of .125 pC/count. The SBDs were calibrated with a Sr-90 β^- source, and the calibration of the entire system was measured to be 4.5 positrons/count.

CHAPTER 5

Determination of Beam Parameters from Simulations and Experiment

This chapter will present the analysis techniques used to match the measured positron spectrum with the calculated positron spectrum. It begins by discussing the Cherenkov analysis which is used to determine the charge in the ion column and the mean and peak energy loss of the beam to the plasma wake. This analysis is purely experimental. The experimental analysis is supplemented with a QuickPIC simulation [12] to verify that the results are reasonable. A beam envelope model is then used to compute the size of the electron beam as it propagates through the ion column. This is also verified with QuickPIC simulations. These two quantities are ultimately used to calculate the positron spectrum. This chapter will describe the entire theoretical basis for our simulation model. The theoretical fit with the experimental results will be presented in Chapter 6.

Before presenting the calculated fit with the experimental data, it is appropriate to explain the parameters that are known to effect the "spectral shape" and the overall positron yield. This can be split into three categories that are not necessarily uncorrelated: number of electrons radiating in the plasma (N_{bi}), wakefield losses ($\Delta\gamma$), and plasma beam focusing ($\sigma_{i:x,y}$). For our example, we use a plasma density of $n_{pe} = 1 \times 10^{17} cm^{-3}$. We assume a Gaussian electron beam with $N_b = 1.2 \times 10^{10}$ electrons, $\sigma_z = 22.5 \mu m$, and vacuum spot sizes of $\sigma_{x,y} = 11 \mu m$. This $\sigma_{x,y}$ is a realistic assumption for the vacuum radius of the electron beam [4]. The other two values, N_b and σ_z will be justified during the analysis.

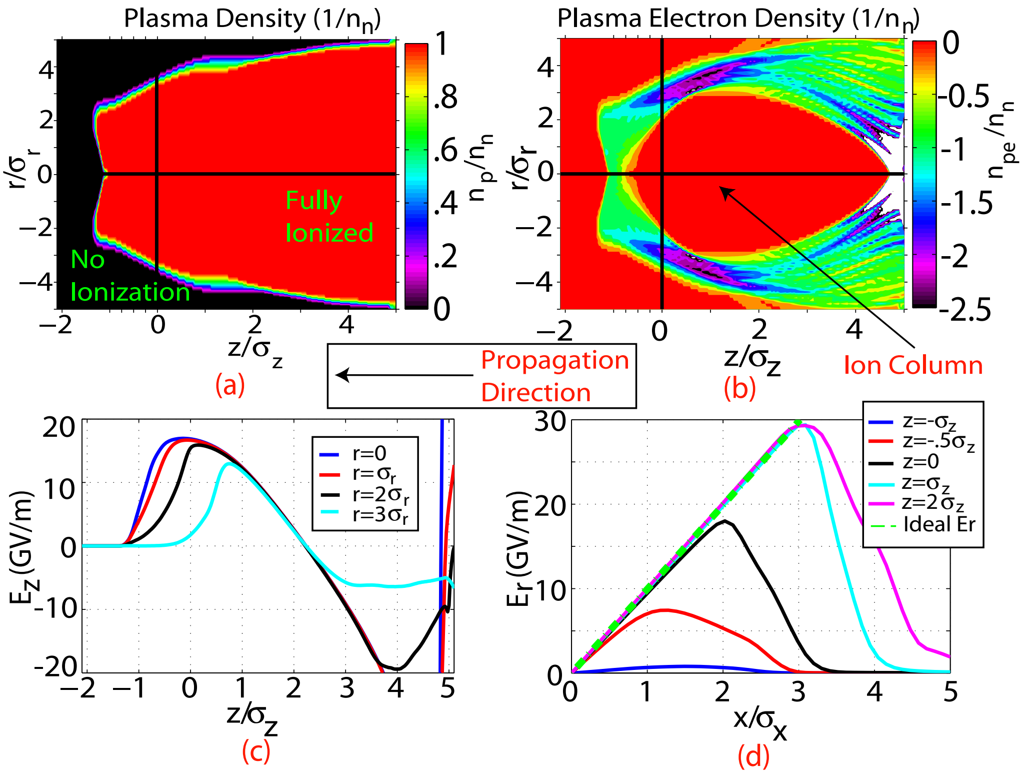

Figure 5.1: QuickPIC simulation of a Gaussian electron beam with $N_b = 1.2 \times 10^{10}$ electrons, $\sigma_r = 11\mu m$, $\sigma_z = 22.5\mu m$ and $n_{pe} = 1 \times 10^{17} cm^{-3}$. (a) Portion of the Li vapor that is ionized. (b) The plasma electron density within the ionized portion of the vapor. (c) The longitudinal electric field (E_z) for four different beam radii. (d) Focusing force (E_r) at six longitudinal positions. All radial units are normalized by σ_r, and all longitudinal units are normalized by σ_z.

5.1 Fraction of the Beam Electrons in the Ion Column

In chapter 2, we have discussed how one might go about estimating the number of electrons that actually reside in the ion column based on the knowledge of LITRACK simulations and the ADK theory of field ionization. However, there is an experimental technique for corroborating this number. The Cherenkov diagnostic provides a great tool for this calculation. As explained in chapter 4, the Cherenkov image of the dispersed electron beam is the main diagnostic used for the determination of energy gain and energy loss. However, it is also an excellent diagnostic for the determination of the charge distribution within the various portions (i.e. energy loss, no energy change and energy gain) of the electron beam.

Before we perform the experimental analysis, it is important to visualize ion column theory. In order to develop a physical simulation model in QuickPIC, there are a few variables that need to be chosen. The Cherenkov analysis gives a mean and peak electron energy loss. This peak electron energy loss value was duplicated in QuickPIC by setting the bunch length to $\sigma_z = 22.5\mu m$. Figure 5.1 is a QuickPIC simulation of the assumed electron beam with $\sigma_{x,y} = 11\mu m$, $\sigma_z = 22.5\mu m$ and $N_b = 1.2 \times 10^{10}$ electrons in a plasma of density $n_{pe} = 1 \times 10^{17} cm^{-3}$. All four plots were created after the beam has fully penetrated the Li. From our analysis in chapter 2, it is clear that field ionization would have taken place, and we should have a fully-developed ion column by this point.

Figure 5.1a plots the ionized portion of the Li from QuickPIC. The black lines denote the center of the electron beam, $z = 0$ and $r = 0$, and the axes are normalized by σ_z and σ_r of the beam. This figure clearly shows that E_{peak} of the electron beam occurs at $r = 1.6\sigma_r$, as this is the radial location where ionization is the farthest forward in the bunch. Full ionization at $r = 1.6\sigma_r$ occurs at $\sim z = -1.2\sigma_z$. However, at $r = 0$ full ionization occurs at $\sim z = +0.1\sigma_z$. This means that at the earliest, we have a pure ion column, defined by equation 2.74 in chapter 2, at $z > +0.1\sigma_z$. Figure 5.1b plots the plasma electron density as a function of radial and longitudinal position. This figure provides the image of the ion column. Within a given radius, a pure ion column is formed when all plasma electrons completely vacate this radius. This occurs at $r \approx +0.8\sigma_z$. It is also important to note that although we have a pure ion column from $\sim r = 0.8 - 3.0\sigma_z$, at each longitudinal position, not all beam electrons reside inside the column. The maximum ion column radius is known to be $r_{i,max} = 2\sqrt{n_b/n_{pe}}$ [38]. For our case, this gives $r_{i,max} = 2.9\sigma_r$. This value is seen at $z \approx \sigma_z$ just beyond where the ion column begins. However, this value continues to decrease as you move toward the rear of the electron beam. Thus, behind $z \approx \sigma_z$ electrons begin to be excluded radially from the ion column. This effect is seen in figure 5.1d which plots the transverse focusing field of the ion column versus longitudinal position in the electron beam. It is clear that the focusing force begins to drop off the ideal case at $r = 2.2\sigma_r$ at $z = 2\sigma_z$. The transverse exclusion of beam electron from the ion column will become less of an issue due to the focusing of the beam from the ramped-density profile (discussed below), but at higher densities, it will still be an issue.

Figure 5.1c plots the plasma wakefield as a function of longitudinal position at various radial positions. It is clear from this plot that the electrons losing the most energy to the wakefield are also the electrons that fully reside in the ion column (i.e. $z \approx \sigma_z$). This energy loss feature of the radiating electrons is used to determine the number of electrons residing in the ion column. We can determine this by looking at the number of electrons that lose energy in the Cherenkov images.

Figure 5.2 gives an example of the spectrum of the beam with and without plasma on the Cherenkov diagnostic before and after median filtering for $n_{pe} = 1\times10^{17}cm^{-3}$. For both cases, the CTR signal is fairly high at 223. For our analysis, we had CTR signals in the range of (-50)-400. In general, the CTR increases with the peak current of the incoming electron beam [3]. The CTR is also correlated to the overall energy lost to the wake. The largest wakes give the largest energy loss (CTR: 400-600), but when synchrotron radiation is desirable, this is the area that we would like to avoid. As we shall see, the X-ray energy radiated by an electron beam in an ion column can be more than an order of magnitude less that that used to drive the plasma wake. This is a problem at high CTR signals as it results in the radiating electron energy γ substantially decreasing as it propagates through the plasma. This decreases the X-ray energy due to the γ^2 dependence on radiated energy. Experimental results in mitigating this issue will be discussed later in this chapter.

To begin the analysis, we need the total number of counts which is proportional to the total number of electrons in the Cherenkov image from the "plasma out" case. We know that most charge is transported effectively from IP0 to the Cherenkov diagnostic at IP2 when the plasma is removed. This will give a calibration of electrons/count on the 16-bit Cherenkov camera. This number will be important for the "plasma in" case where the large divergence at the exit of the plasma creates a loss of some charge before it reaches the Cherenkov diagnostic. First, a background needs to be subtracted from the "plasma out" image (Figure 5.2a). This background was taken by averaging each pixel over 75 shots. The background values ranged from about 250-350 counts. The typical "plasma in" and "plasma out" images after the background subtraction are shown in Figure 5.2. The count range is from 0-2000 as seen in the color bar. The counts at each pixel on the image in both the x-plane (horizontal) and energy-plane (vertical) were summed. This gave a total amount of counts C_c on the Cherenkov camera. For this run (07132cx), the value is about $C_c = 7.9 \times 10^6$. The toroid coil detector which measures the total charge in the beam was N_e at the entrance of the FFTB for this case was $N_e = 1.63 \pm .10 \times 10^{10}$. This gives a calibration of roughly 2063 electrons/camera count. This calibration value will be used to calibrate the total number of electrons losing energy within the ion column.

After the background subtraction, the "plasma in" plots need to be filtered to eliminate the noise caused by x-rays hitting the CCD chip. The Cherenkov camera was shielded with lead, but some x-rays were still able to hit the chip on every shot. Figure 5.2b shows a shot with many x-rays hits. Since the typical pixel value was 0-2000 counts, a few large x-ray hits (like the one marked on 5.2b, for example) on the 16-bit camera can give multiple pixel count values of 65000. When the total counts are summed, this adds a substantial error to the ultimate charge computed. A median filter is used to mitigate this issue. Figure 5.2c shows the same image after a 4 by 4 median filter is applied. It is clear that the most of the x-ray noise is minimized. There is some loss of structure within the main electron beam image. However, the filtering effect in these areas is small in comparison to that around the x-ray hits, leading to an acceptable error.

The median-filtered case "plasma in" image is split into 3 regions as shown in Figure 5.2. Region (1) contains all the electrons when the plasma is out. When the beam propagates through the plasma, roughly 30 percent of the beam electrons are unaffected by the plasma and therefore remain in Region (1). The beam current at these longitudinal positions in the beam is simply too low to cause any appreciable field ionization in Li. LITRACK studies have verified this low current "trunk" on the front of the beam as seen in Figure 2.9a in chapter 2 [20]. This charge propagates through the Li gas before ionization, leading to a large sum of charge not only out of the ion column, but also out of the plasma itself. The upper and lower edges of this region, denoted by the green lines, were chosen from the energy spread of the "plasma out" case as seen in Figure 5.2a. Region (2) is the "Upper" region of the image. These are particles that have been accelerated in the wake driven by the electrons in the front of bunch. For our experimental conditions, fewer than 5 percent of the total number of electrons were ever accelerated. Thus, few electrons appeared in this region. They are largely absent as seen in Figure 5.2c. Region (3) is the energy loss or "Lower" region. These are the electrons that lost energy to the wake and are mostly radiating in the ion column.

The total counts (i.e. charge) is summed in region (1) and (2). This gives the total counts outside of the energy loss region. In the regime where CTR < 200, the charge in region (3) is simply summed by itself. Summing all three regions gives a total number of counts for each shot. However, when CTR > 200, there is a slight loss of electrons. These electrons are so low in energy that they are deflected below the Cherenkov aerogel from the dipole spectrometer. Thus, they never interact with the diagnostic and cannot be seen in the image. For these cases, the total counts from the "plasma out" case was used, and the counts from region (1) and (2) were subtracted from this value to give the total counts in the energy loss region (3). This is the region where the median filtering of the image becomes important. If this filtering was not performed, the image would have an artificially large number of counts in regions (1) and (2). This would result in a smaller amount of charge in region (3), leading to a spurious result.

The shot used in the example had a CTR value of 223. The analysis gives counts in region (1) (Head) of $C_{c1} = 3.03 \times 10^6$, region (2) (Upper) of $C_{c2} = 5.4 \times 10^4$, and region (3) (Lower) of $C_{c3} = 4.09 \times 10^6$. These values correspond to the following number of electrons: $N_{e1} = 6.25 \times 10^9$, $N_{e2} = 1.11 \times 10^7$, and $N_{e3} = 8.44 \times 10^9$, respectively. It is important to note that this analysis is only accurate when relatively few beam electrons are in the accelerating field. Electrons in the rear of the bunch are accelerated. These are also the particles that begin with the lowest energy (i.e. the lowest points on the "plasma out" case in Figure 5.2a). If particles within this region are accelerated, they will move upward from region (1) toward

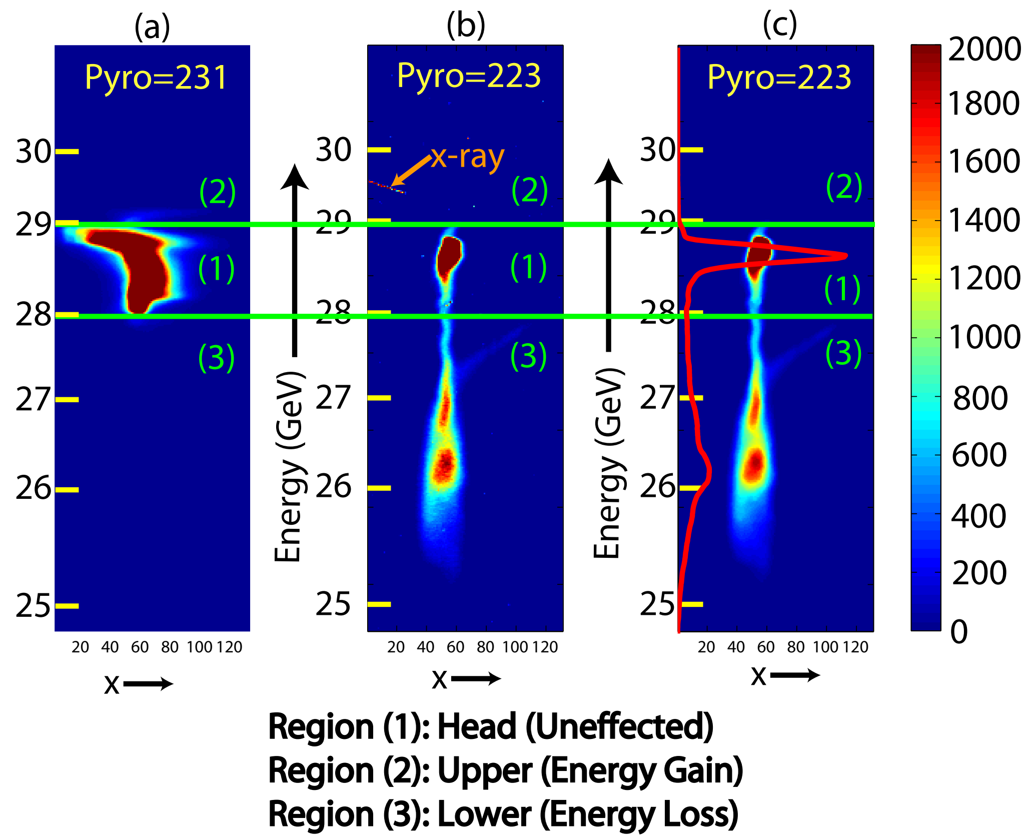

Figure 5.2: Example Cherenkov Image. (a) "Plasma out" case. (b) "Plasma in" case without median filter. (c) Same as (b) with a 4 by 4 median filter. Also, contains a vertical lineout of the beam. The horizontal axis (x) for all plots is the width of the beam. The vertical axis (energy) for all plots gives the energy spectrum of the beam. All images are taken with $n_{pe} = 1 \times 10^{17} cm^{-3}$.

region (2), instead of moving from region (1) to region (3). Even though these particles are in the ion column, they will not be counted since they reside behind the electrons in region (1). However, for our case, it is clear from the previous example that even at high CTR (i.e. 223), only about one percent of the particles are accelerated to energies greater than the maximum energy of the initial beam. These accelerated particles are neglected, even though they may reside in the ion column, adding a small error that is deemed acceptable.

Now that the total amount of charge in the ion column is known, the mean energy of this charge in the energy loss region (3) of the wake can be computed in the following way. The total charge in region (3) was computed using the method listed above. The mean energy of the electrons in region (3) is defined by the vertical pixel where 50 percent of the region (3) charge is above and 50 percent of the region

(3) charge is below. To find this point, you begin at the lower edge of region (1) (the green line near 28 GeV) and sum all x-pixels for a given energy-pixel until the energy-pixel is reached where the sum is equal to $.5C_{c3}$. The energy lineout of the charge is shown as the red line in Figure 5.2c. Each vertical pixel has a specific energy as determined by our Cherenkov calibration. The energy scale is shown on the plots in Figure 5.2. The result gives the mean energy of the electrons in region (3), or, simply put, the mean energy of the particles in the ion column. This gives the second important result. We have calculated the average energy of the ion column electrons after they leave the plasma. Due to the γ^2 dependence on radiated energy, knowing this loss to the wake is imperative for a proper theoretical fit to the experimentally measured spectrum.

Beyond the average energy loss of the ion column electrons, another important result from this analysis is the peak electron beam energy loss. Knowing this number allows for the matching of our beam parameters to QUICKPIC. In linear theory, when the wake is at resonance, defined by $k_p\sigma_z = \sqrt{2}$, the wake amplitude is dependent upon $1/\sigma_z^2$ when at resonance. However, the dependence upon σ_r is weak. Thus, knowing the peak energy loss of the electron beam allows us to match the electron beam with a specific bunch length within QUICKPIC. The 1 percent charge contour is defined as the peak energy loss. This means that the pixel is found where 99 percent of the charge resides at a higher energy. This pixel is determined to be the peak energy loss of the beam.

In order to accurately represent the data, averages must be taken. Bins are created with respect to CTR. All images within each CTR bin are averaged to give a mean and error of the mean value for the charge in the Upper (2), Lower (3) and Head (1) regions. The mean energy of the charge in the Lower region is also averaged for all shots within each CTR bin. These results are similar to those shown using the LITRACK analysis of Figure 2.8b in chapter 2.

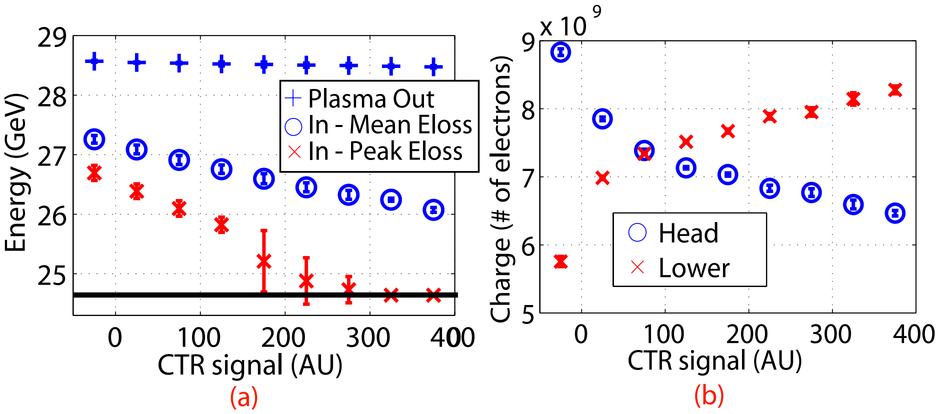

Figure 5.3: Example Cherenkov Analysis. Each point represents a pyro bin of 50. (a) Average electron energy loss in Lower region (wakefield+radiation) versus CTR bin. Also, plotted is the peak energy loss for all electrons versus CTR bin. The black line specifies the lower edge of the Cherenkov diagnostic. (b) Head and Lower charge versus CTR bin. All images are taken with $n_{pe} = 1 \times 10^{17} cm^{-3}$.

5.2 Wakefield Losses

When the plasma wake is driven, energy is transferred from the electrons in the front of the bunch to the wake as seen in Figure 5.1c. As mentioned above, these are also the electrons in the ion column. Thus, there is an additional energy loss for these electrons as they radiate synchrotron energy. Since synchrotron energy loss is proportional to γ^2 as seen in Equation2.69, the wakefield losses can have a substantial effect on the overall positron yield. To give an example, a 28.5 GeV electron traversing a plasma with $n_{pe} = 3 \times 10^{17} cm^{-3}$ and $r_\beta = 10 \mu m$ will radiate $\sim$ 4.3 GeV/m. However, it has been experimentally observed that the same particle will lose $\sim$ 40 GeV/m to the wakefield [20]. The magnitude of this effect cannot be ignored, even at lower densities.

For the data in our example, Figure 5.3 plots the two important results from the experimental Cherenkov analysis. Figure 5.3a shows the average energy loss for the electrons in the region (3) (ion column) (blue o) versus CTR. The data were averaged in CTR bins of 50. It also plots the average energy of the entire electron beam with the "plasma out" (blue +). The average energy loss increases as CTR increases. This is due to the fact that the CTR is directly proportional to the peak current of the electron beam [3]. For a given charge in the bunch N_{bo}, as the CTR increases, the increase in peak current results in a decrease in bunch length σ_z. At resonance, the amplitude of the linear wakefield scales as $1/\sigma_z^2$ [?]. Thus, this increase in wakefield amplitude with CTR is expected. It is important to note that the average energy loss quoted is the total energy loss, defined as the loss to the wakefield and the loss to radiation. As stated above, we know that the majority is lost to the wakefield. In this case, with $n_{pe} = 1 \times 10^{17} cm^{-3}$, eqn.2.69 predicts that an electron at $r_\beta = 10\mu m$ will lose 478 MeV/m. In this example, we would expect an energy loss to radiation of roughly 48 MeV. However, an electron in the CTR bin of 200 experiences a total energy loss (wakefield+radiation) of $\sim$ 2 GeV. This proves the prior point that the majority of the radiation is lost to the wakefield in our current setup. The method of accounting for this effect when fitting the measured spectrum with the computed spectrum will be discussed below. Figure 5.3a also plots the peak electron energy loss (red x) as defined above as the 1 percent charge contour. This value is important as it is duplicated in our QuickPIC simulation to verify that the simulation is matching the experimental conditions.

Figure 5.3b gives the average amount of charge in the Lower (ion column) region of the Cherenkov diagnostic. The data are averaged in CTR bins of 50. It is clear that charge is transferred from the Head region (1) to the Lower region (3) as the CTR increases, as expected, since a higher CTR value equates to a shorter bunch length. This creates a higher density electron bunch which will field-ionize the Li vapor and blow-out the plasma electrons sooner in the bunch [4], resulting in more beam electrons radiating inside the ion column.

5.3 Plasma Beam Focusing

The number of electrons in the ion column and the energy of the electrons clearly effects the total x-ray yield and ultimately the positron yield. The physical size of the radiating portion of the electron beam in the plasma also plays a large role in the ultimate X-ray and position yield. The evolution of $\sigma_{x,y}$ for a Gaussian beam in vacuum and in a plasma is given by the beam-envelope equation [29]

$$\frac{d^2\sigma_{x,y}(z)}{dz^2}+\left[k_\beta^2-\frac{\epsilon_{N:x,y}^2}{\gamma^2\sigma_{x,y}^4(r)}\right]\sigma_{x,y}(r)=0 \tag{5.1}$$

where $\epsilon_{N:x,y}$ is the normalized emittance of the beam in the given transverse plane. This equation can be solved numerically in z to give a vacuum beam and plasma beam profile. To get the vacuum profile, you simply set $n_{pe} = 0$ (i.e $k_\beta = 0$). A model has been written in MATLAB to solve for the electron beam size propagating in vacuum and in plasma [39]. Data was taken at the upstream OTR which is known to be roughly 1.16 m upstream of the plasma entrance. Also, we have an approximate beam size of $\sigma_x = \sigma_y = 10\mu m$ at the plasma entrance as defined by the optics in the FFTB. These results were validated with wire scanners placed at the waist location before the plasma was put into the beamline at FFTB. The focusing conditions were set to create a round beam at the plasma entrance. However, the emittance blow-up due to the $75\mu m$ Be window upstream of the plasma caused the two beam dimensions to focus at different locations. Thus, the Y-waist focuses downstream of the X-waist. Given the distance from the upstream OTR to the plasma entrance and a beam size at the plasma entrance, a $d\sigma_x/dz$ and $d\sigma_y/dz$ can be computed. These values are used to seed the numerical calculation. For the data presented below, we were running with the X-waist approximately 5 cm upstream of the plasma entrance. Thus, the Y-waist would be downstream of this position.

The results of this calculation are shown in Figure 5.4 for the X and Y planes individually. All four figures show a plasma density profile (green dotted line) that was fit to experimental data. This ramped-density on the edge of the plasma profile focuses the beam in both planes before it enters the peak density region of the plasma profile. The majority of the synchrotron radiation is emitted in this peak density region. Thus, this focusing effect reduces the radiated energy substantially due to the radiated synchrotron energy dependence on r^2. This effect is shown for both the X and Y beam planes in Figure 5.4. This model assumes a fully-ionized plasma when the beam enters the ramped plasma region. The plot shows the beam propagation through vacuum (red dotted line) and the beam propagation through a 11cm Li plasma with $n_{pe} = 1 \times 10^{17} cm^{-3}$ (blue solid line). The focusing effect due

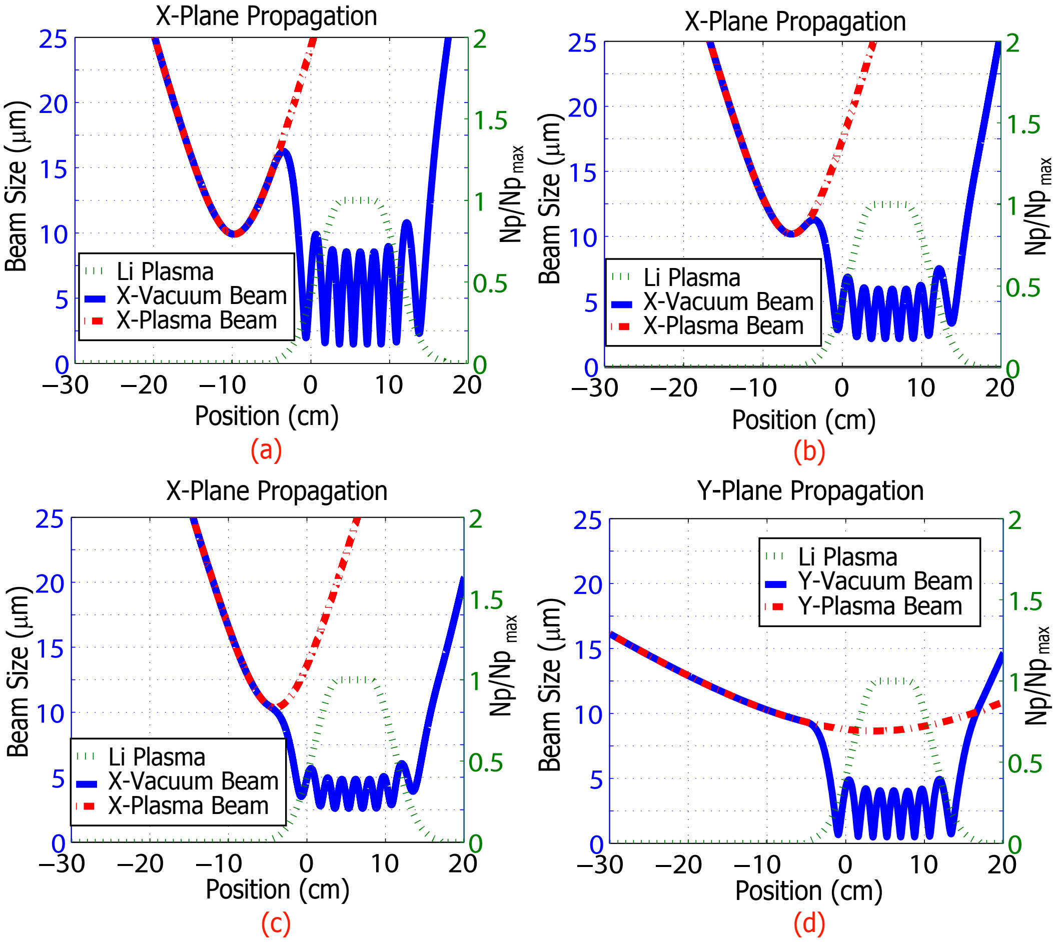

(a) (b) (c) (d)

Figure 5.4: Plot showing vacuum and plasma propagation for both X and Y planes as the beam waist is moved. (a) X-plane propagation with the waist set at $z = -10cm$ leading to a $\sigma_x = 8\mu m$ radiating spot size. (b) X-plane propagation with the waist set at $z = -6cm$ leading to a $\sigma_x = 6\mu m$ radiating spot size. (c) X-plane propagation with the waist set at $z = -3cm$ leading to a $\sigma_y = 5\mu m$ radiating spot size. (d) Y-plane propagation with the waist set at $z = -3cm$ leading to a $\sigma_y = 4\mu m$ radiating spot size. All plots assume a peak density $n_{pe} = 1 \times 10^{17} cm^{-3}$.

to the edges of the plasma is clear by looking at the beam size inside the plasma.

This result is also verified in QuickPIC simulations. Figures 5.5a and 5.5b plot the charge distribution at beam center (z=0) at the peak beam envelope size for both y and x, respectively, within the peak density region of the plasma for the experimental profile of Figure 4.8 in Chapter 4. This figure along with our beam envelope analysis both show that substantial focusing occurs due to the density ramp. This plot is a nominal case with $\epsilon_x = 80mm - mrad$ and $\epsilon_y = 20mm - mrad$ giving $\sigma_x \approx \sigma_y \approx 5\mu m$. If the emittance decreases, σ_x and σ_y will decrease even

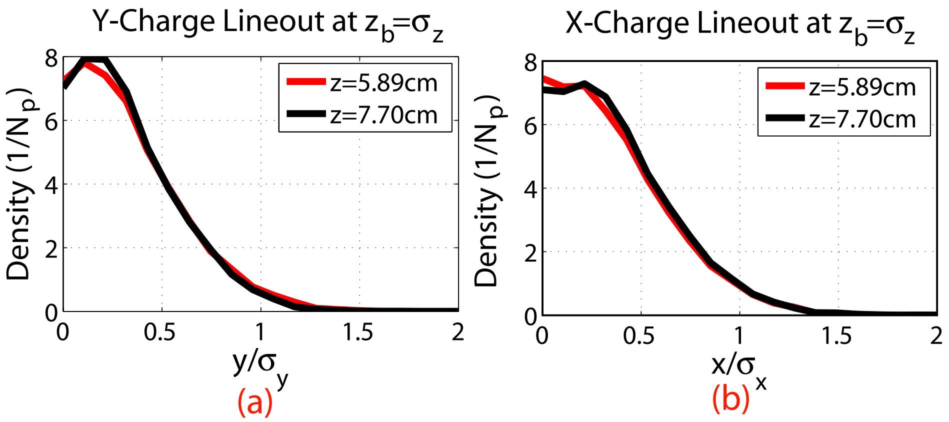

Figure 5.5: QuickPIC simulation showing the beam size within the peak density region of the plasma for the (a) Y-plane and (b) X-plane. Each plot shows the periodicity of the beam envelope by plotting two distributions after $\lambda_\beta/2$. The simulation assumed a Gaussian electron beam with $N_b = 1.2 \times 10^{10}$ electrons, $\sigma_r = 11\mu m$, $\sigma_z = 22.5\mu m$ and $n_{pe} = 1 \times 10^{17} cm^{-3}$.

further, and if the emittance increases, σ_x and σ_y will increase even further. This value is defined as the $\sigma_{i:x,y}$ in our theoretical fits of Chapter 6. As expected, the peak σ_x and σ_y occur after $\approx \lambda_\beta/2 = 1.75cm$ in both planes since the beam envelope will oscillate at twice the frequency of the individual electrons. Figure 5.4 gives another important result. Figure 5.4a,b,c give σ_x of the electron beam within the central peak region of the plasma where the majority of the synchrotron X-rays are radiated. During the experiment, the electron beam waist was moved in intervals of 5cm. It was difficult to determine the beam location to a precision of greater than that distance. However, these three plots show how the central radiating beam σ_x changes by moving the X-waist upstream and downstream only 3cm. Figure 5.4a shows the X-waist location at -10 cm, and it gives a central beam $\sigma_x = 8\mu m$. Figure 5.4b shows the X-waist location at -6 cm, and it gives a central beam $\sigma_x = 6\mu m$. Figure 5.4c shows the X-waist location at -3 cm, and it gives a central beam $\sigma_x = 5\mu m$. Figure 5.4d shows the Y-waist location at 0 cm, and it gives a central beam $\sigma_y = 4\mu m$. Due to the fact that $\beta_y \approx 7\beta_x$, σ_y within the plasma had little dependence on Y-waist position. Thus, only the X-waist change was studied.

These unmeasurable changes in the X-waist location lead to large changes in

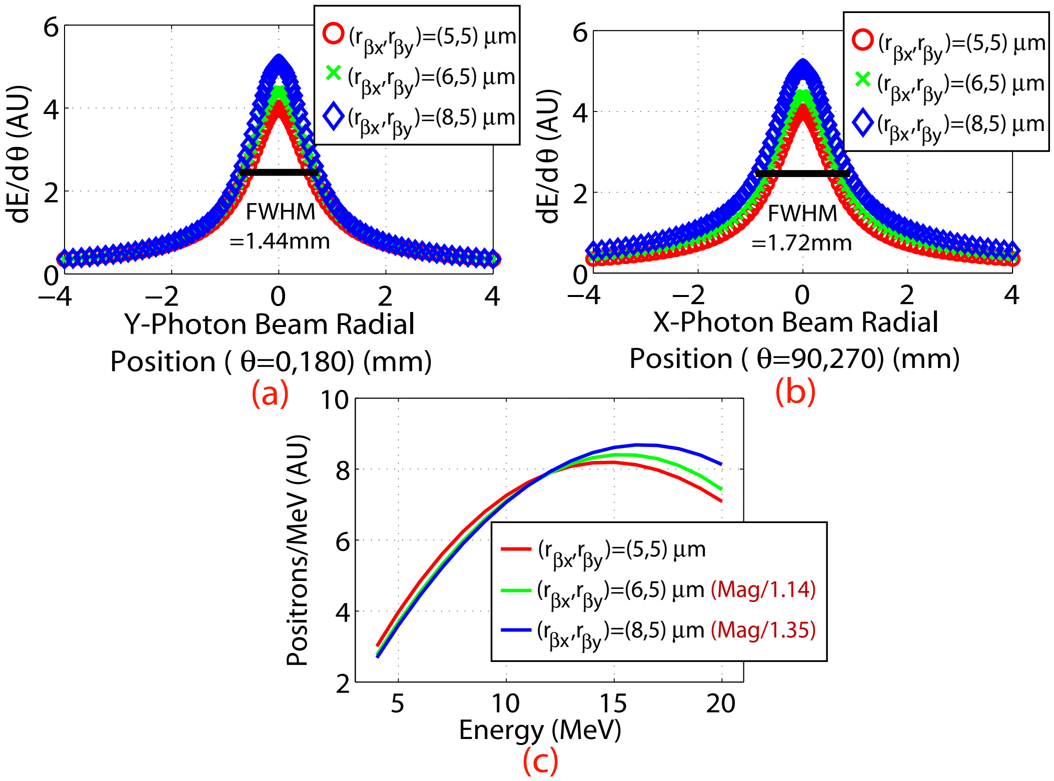

Figure 5.6: Plot showing the radiated energy versus radius for (a) Y-plane ($\theta = 0^o$ and 180^o) and (b) X-plane ($\theta = 90^o$ and 270^o). Each has three cases plotted; case 1 $[(\sigma_x, \sigma_y) = (5,5)\mu m]$, case 2 $[(\sigma_x, \sigma_y) = (6,5)\mu m]$, and case 3 $[(\sigma_x, \sigma_y) = (8,5)\mu m]$. (c) Positron yield for all three cases. The last two are divided by 1.14 and 1.35 respectively to show the similarity of the spectral "shapes". The relative yield for case 1 = 1.0, case 2 = 1.13, and case 3 = 1.37. All cases assumes a peak density $n_{pe} = 1 \times 10^{17} cm^{-3}$.

σ_x of the electron beam within the plasma. Due to the r_β^2 dependence on the radiated energy, one would expect these changes to have a large effect on the total radiated X-ray energy and the overall positron yield. This fact is demonstrated in the simulation in Figure 5.6. Three cases are plotted where the Y-waist location is kept constant while the X-waist location and the subsequent σ_x in the peak density region of the plasma is changed. The three cases are equivalent to the cases plotted in Figure 5.4a,b,c with $\sigma_x = 5\mu m$,$6\mu m$ and $8\mu m$ and with $\sigma_y = 5\mu m$. Figure 5.6a plots a lineout in the Y-plane whereas Figure 5.6b is a lineout in the X-plane. The orientation is clear since the FWHM of Figure 5.6a is $\approx 1.44mm$ while that of Figure 5.6b is $\approx 1.72mm$ for the case where $\sigma_x = 8\mu m$ and $\sigma_y = 5\mu m$. This result is expected since the photon angular divergence is proportional to K/γ, and $K_x > K_y$. When the total radiated energy is integrated, we find the total radiated energy for case 1 $[(\sigma_x, \sigma_y) = (5, 5)\mu m]$, case 2 $[(\sigma_x, \sigma_y) = (6, 5)\mu m]$, and case 3 $[(\sigma_x, \sigma_y) = (8, 5)\mu m]$ are 1.00, 1.10, 1.26, respectively. Thus, theoretically, a difference of only 6cm in the X-waist location should lead to a 26 percent increase in the total radiated energy at the target at this location relative to the plasma entrance. Figure 5.6c shows the simulated positron spectrum between 4-20 MeV for these cases. It is clear from the plot that although the "shape" of the spectrum does not change, the overall amplitude, and thus positron yield, can change substantially. The overall positron yield from 4-20 MeV for case 1, 2 and 3 is 1.00, 1.13 and 1.37, respectively. Thus, with all other beam parameters kept constant, a small change of $\sigma_x = 5 - 8\mu m$ should lead to a 37 percent increase in the positron yield at our detectors in this energy range. It is in fact the yield that puts the largest constraint on fitting the measured spectrum with the computed spectrum. Knowing this, both the yield and the spectral "shape" are used to fit the data with theory.

It is important to note that if large radial changes in the peak density region were being made, and all other parameters were held constant, we would see massive fluctuations in the overall positron yield. However, the above analysis does not account for field ionization and the radial extent of the ion column. Given the same σ_z and N_b, the ion column will always have the same peak radius for a gaussian beam. This radius is defined by [38]

$$r_{i,max} = 2\sigma_r \sqrt{\frac{n_b}{n_{pe}}} \tag{5.2}$$

However, the beam density n_b is defined by

$$n_b = \frac{N_b}{(2\pi)^{3/2}\sigma_r^2\sigma_z} \tag{5.3}$$

When these equations are combined, we find that

$$r_{i,max} \approx \frac{1}{2}\sqrt{\frac{N_b}{\sigma_z n_{pe}}} \tag{5.4}$$

This means that an increasing beam radius will not only create ionization later in the bunch, but less of it's particles will reside in the ion column transversely since the peak radius of the ion column $r_{i,max}$ will stay constant. Since these large changes in the positron yield are not observed experimentally, we must assume that the maximum positron yield is limited more by field ionization (i.e. the number of electrons in the ion column) and $r_{i,max}$ than by the radius of the beam inside the plasma. This hypothesis is supported by Figure 5.7. This figure shows that the incoming beam density in the edges of the plasma determines the longitudinal position of field ionization since all four plots have roughly the same location of initial ionization. Figure 5.7a shows that for our ramped neutral density profile, at $n_{pe} = .01 n_{p,max}$, the longitudinal position of the ionization front has already been determined. Since the electron beam is moving at roughly the speed of light, we know that even as the electrons in the ionized portion of the Li focus down to a smaller beam size, the ionization front cannot move forward. Thus, it is the initial beam density at the location where the electron beam first hits the Li vapor that determines the number of particles in the ion column and thus the position yield.

At first glance, one could deduce that Figure 5.1b and Figure 5.1d show that we have less than 50 percent of our Gaussian beam (i.e $N - b < 6 \times 10^9$) in a pure ion column since it is not until nearly $z = \sigma_z$ that we have a pure ion column. Even at $z = 0$, there is a large focusing force, but the plasma electrons in the center reduce the field. Thus, the beam at this longitudinal position can be approximated as a Gaussian beam with a smaller radius in a pure ion column. However, this issue is

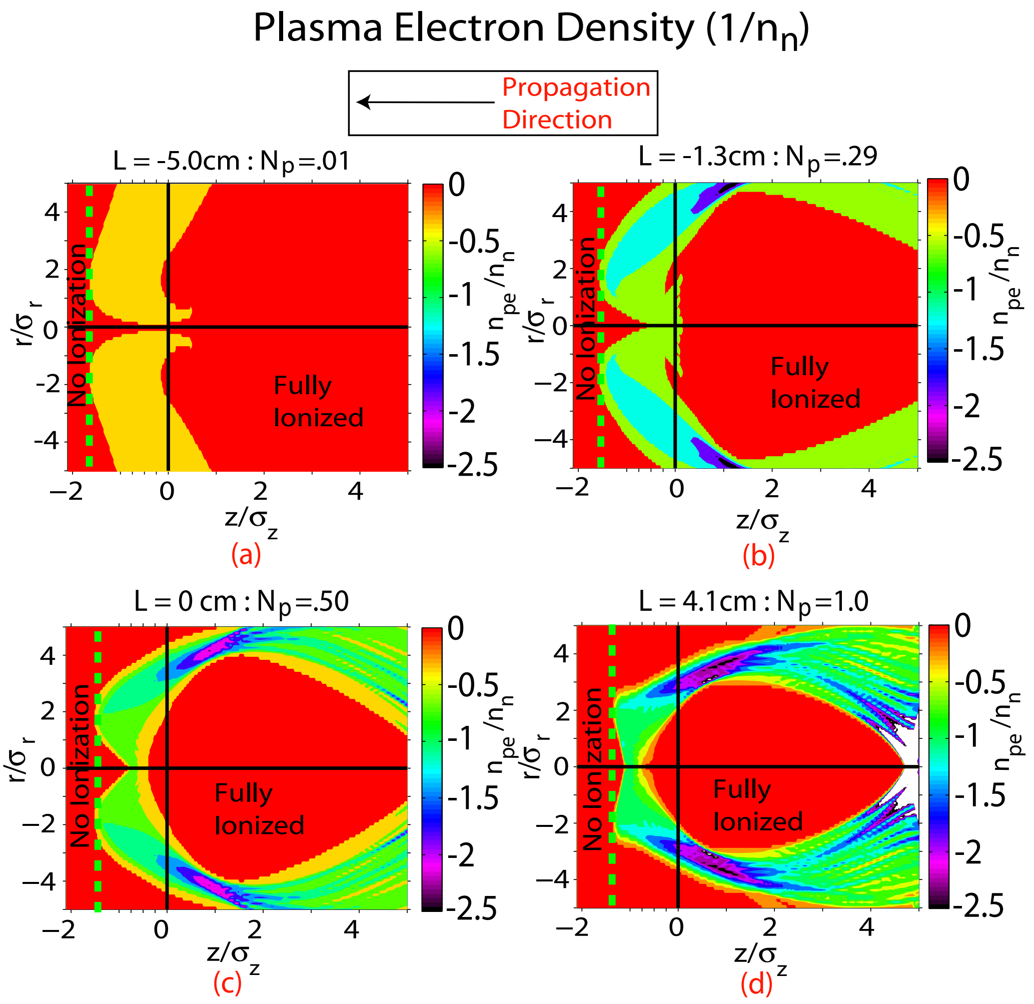

Figure 5.7: Plots showing the plasma electron density from a QuickPIC simulation with an experimental ramped neutral density profile, (positions and neutral density are defined relative to those in Figure 5.4), with a Gaussian electron beam with $N_b = 1.2 \times 10^{10}$ electrons, $\sigma_r = 11\mu m$, $\sigma_z = 22.5\mu m$ and $n_{pe} = 1 \times 10^{17} cm^{-3}$. The plasma electron distribution at (a) $z = -5.0cm$ and $n_{pe} = .01 n_{p,max}$, (b) $z = -1.3$ and $n_{pe} = .29 n_{p,max}$, (c) $z = 0.0cm$ and $n_{pe} = .5 n_{p,max}$, and (d) $z = 4.1cm$ and $n_{pe} = n_{p,max}$. All cases assumes a peak density $n_{p,max} = 1 \times 10^{17} cm^{-3}$.

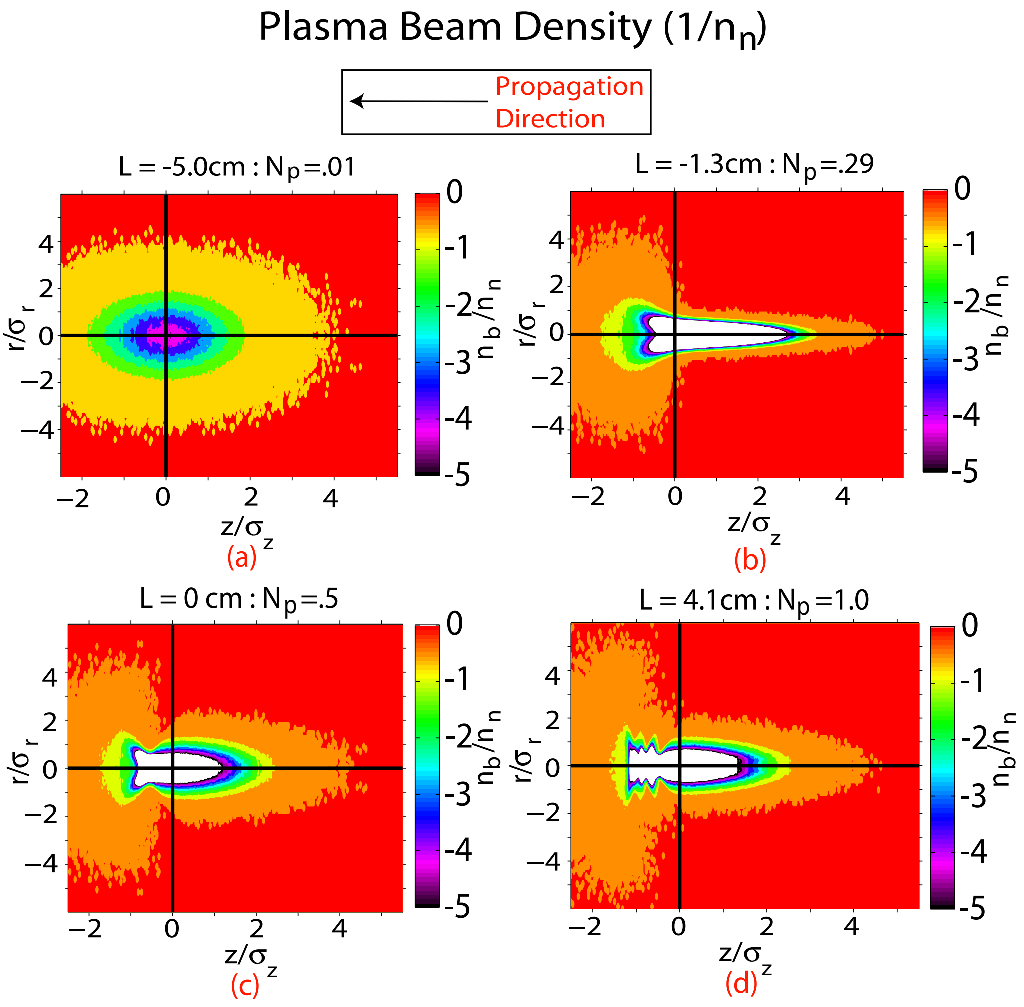

Figure 5.8: Plot showing the beam density from a QuickPIC simulation (same as Figure 5.7) with an experimental ramped neutral density profile, (positions and neutral density are defined relative to those in Figure 5.4), with a Gaussian electron beam with $N_b = 1.2 \times 10^{10}$ electrons, $\sigma_r = 11\mu m$, $\sigma_z = 22.5\mu m$ and $n_{pe} = 1 \times 10^{17} cm^{-3}$. The plasma electron distribution at (a) $z = -5.0cm$ and $n_{pe} = .01 n_{p,max}$, (b) $z = -1.3$ and $n_{pe} = .29 n_{p,max}$, (c) $z = 0.0cm$ and $n_{pe} = .5 n_{p,max}$, and (d) $z = 4.0cm$ and $n_{pe} = n_{p,max}$. All cases assumes a peak density $n_{p,max} = 1 \times 10^{17} cm^{-3}$.

mitigated by the focusing of the beam due to the ramped-plasma density profile. Once the beam begins to focus, the electric field of the beam increases, removing more plasma electrons from the inner radii of the plasma column, thus, moving the "pure" ion column threshold farther upstream in the electron bunch. This result is also illustrated in Figure 5.7. Figure 5.8 shows the beam profile at the same times as the four plots in Figure 5.7. Figure 5.8 clearly shows the beam focusing within the plasma density ramp, and as the focusing takes place, the pure ion column is moving forward. This is denoted in the change of the pure ion column from $\approx z = 0$ in Figure 5.7b to $\approx z = -.5\sigma_z$ in Figure 5.7d. This accounts for the difference that is produced from the density ramp case versus the "step-function" plasma profile illustrated in Figure 5.1.

From this analysis, we know that the X-ray energy and the ultimate positron yield is dependent upon N_{bi}, γ, and $\sigma_{i:x,y}$. From the lack of spectral changes when incoming beam parameters were changed, we must claim that these four parameters are interchangeable. For example, as we change the X-waist location, we are changing the beam size within the plasma, but we are also changing the longitudinal position of the field ionization threshold while the ion column radius remains constant. The electron beam may get larger, but less electrons are in the ion column, longitudinally and transversely. Thus, comparing multiple runs is very difficult, and care must be taken to guarantee that the initial conditions of the data sets are understood to be similar.

CHAPTER 6

Results

6.1 Introduction

In this chapter, the experimentally measured positron spectra and the total positron yield as a function of various experimental parameters are presented. Wherever possible, we have compared the experimental data with theory. We find that the calculated spectrum matches well with the experimentally measured spectrum. The change of the positron yield versus CTR signal (i.e. bunch length), plasma density, and the electron beam waist location will also be discussed. The matching of the experimental data with theory gives confidence that one can scale this simulation model to optimally design a positron source based on X-ray radiation produced from electron betatron motion within a plasma wiggler.

Table 6.1 lists the various "null-tests" that were performed to confirm that the signal detected on the surface barrier detectors (SBDs) when the plasma was in, the convertor target was in, and the e^+/e^- spectrometer magnet was on, were indeed due to pair-production by betatron X-rays produced in the plasma. The magnet "on" setting refers to imaging 10 MeV positrons. The signal-to-noise ratio between the plasma in and plasma out cases was roughly 2000. This gives confidence that the detector signal was produced by betatron X-rays emitted in the plasma. A typical signal-to-noise ratio of roughly 7, between the convertor target in and convertor target out cases, was obtained when the beam propagated through the plasma and the e^+/e^- spectrometer magnet was on. This provides proof that the target was creating the detected signal. The small signal detected when the target was out was likely due to scattering of particles and photons within the spectrometer setup.

Plasma	Positron Target	Magnet	Signal (AU)
OUT	OUT	OFF	1
OUT	OUT	ON	1
OUT	IN	OFF	1
OUT	IN	ON	1
IN	OUT	OFF	50
IN	IN	OFF	50
IN	OUT	ON	300
IN	IN	ON	2000

Table 6.1: This table lists the relative scaling for all different positron data cases. Magnet "on" assumes that 10 MeV positrons are being detected. The plasma density is $n_{pe} = 1 \times 10^{17} cm^{-3}$.

6.2 Positron and Electron Measured Spectra Agreement

During the pair production process, a photon decays into a positron and an electron. Although most of the data presented in this chapter is positron data, by reversing the polarity of the magnetic spectrometer, a few data sets were taken to ensure that there was a similar electron spectrum. This symmetry verifies that the target was producing the positrons. Figure 6.1a shows typical electron and positron spectra. For this case, electron data was taken immediately following a positron run to minimize the effects of linac variations. The two spectra virtually overlap for energies greater than 7 MeV. However, in the 4-7 MeV energy range, the number of positrons/MeV exceeds that of the electrons. This is thought to be due to a CTR energy during the positron run that was closer to the optimal value for the production of X-rays. Thus, the electron beam in the positron case radiated more X-rays during these shots than that for the electrons, creating a higher yield. This is shown in figure 6.1b. It will be shown later in this chapter that the peak positron yield occurs near a CTR energy of 300 for this plasma density of $n_{pe} = 1 \times 10^{17} cm^{-3}$. It drops on either side of this value. Thus, for the 3.5, 4.5 and 5.5 MeV bins, figure 6.1b shows that the positron data had CTR energies of 410, 330, and 360, respectively, near

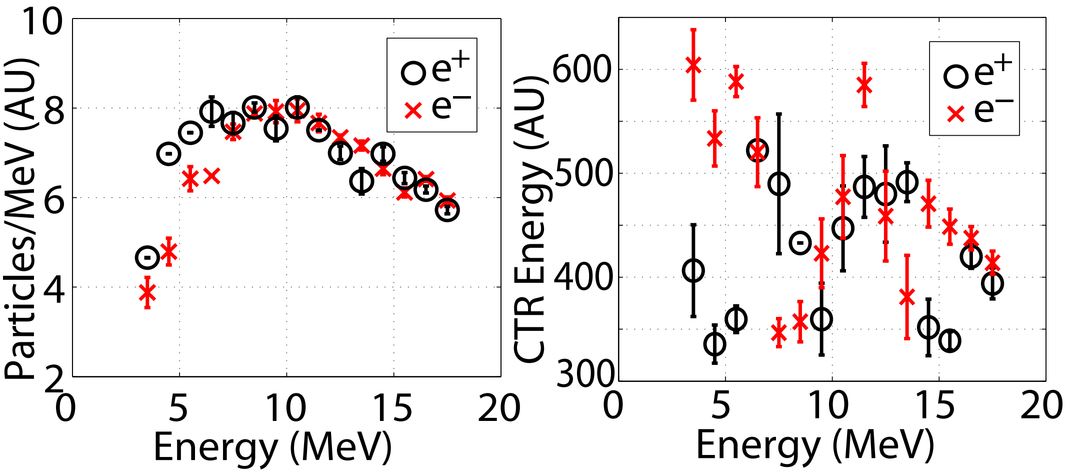

Figure 6.1: (a) Measured spectra for both electrons (e^-) and positrons (e^+) for $n_{pe} = 1 \times 10^{17} cm^{-3}$ with averages taken in 1 MeV energy bins. (b) CTR energy ($1/\sigma_z$) for the electrons and positrons for the same 1 MeV energy bins.

the optimum for yield. Whereas, for the same bins for the electron data had CTR energies of 610, 530, 590, respectively. This deviation of the electron beam from the optimal CTR energy in the electron detection case, led to the decrease in electron yield versus positron yield for the same energy bins. However, the agreement at high energies is excellent. This result shows that the W target was producing the pairs detected in this experiment. For the remainder of the results chapter, only positron data will be shown.

6.3 Comparison of Measured Positron Spectrum with Theory

The measured positron spectrum was compared with theory for the following plasma densities: $n_{pe} = 1 \times 10^{17} cm^{-3}$, $n_{pe} = 6.4 \times 10^{16} cm^{-3}$ and $n_{pe} = 3.3 \times 10^{16} cm^{-3}$. The length of the full-width at half-maximum (FWHM) of each oven profile is plotted in Figure 6.2. Since $\lambda_\beta \propto \sqrt{n_{pe}}$, this length is important for determining the number of saddle-points that should be considered in the simulation.

The first case considered has a density of $n_{pe} = 1 \times 10^{17} cm^{-3}$. It is important to note the parameters that are known. First, figure 6.2 shows that the FWHM of the

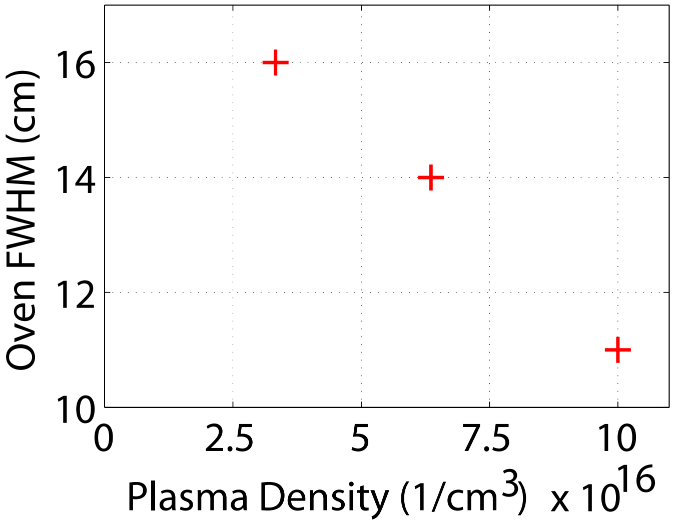

Figure 6.2: (a) Li Oven Full-width at Half Maximum (FWHM) for the oen cases discussed in this chapter.

Li plasma is 11 cm for this case. Second, factor in the number of particles that lost energy and are therefore radiating in the ion column from the Cherenkov images recorded during the experiment. For the data set of interest, the mean CTR signal was ≈ 85. From Figure 6.4b, we see that this correlates to $N_{bi} \approx 7.2 \times 10^9$. Third, from the same Cherenkov analysis, the average energy loss of the electrons within the ion column is known. From figure 6.4a, at the same CTR signal, this gives an energy loss of ≈ 2 GeV. Fourth, the energy of the incoming electrons from the X-ray spectrometer which was $E_{beam} \approx 28.5$ GeV.

Wire scanners were used to find the beam waist, and it was computed in vacuum to be $\sim 10\mu m$ in each plane. The X-waist location was $z \approx -5cm$ and the Y-waist location was $z \approx 0cm$. In figures 6.3a and 6.3b plot the variation of the beam spot size $(\sigma_{i:x,y})$, respectively as the electron beam propagates through the plasma. Each electron has two saddle-points per wavelength. Thus, the number of beam envelope oscillations gives the number of saddle-points. The X-ray spectrum at all six saddle-points is computed with their respective densities of $n_{pe} = 4.5$, 9, 10, 10, 10, $7.5 \times 10^{16} cm^{-3}$. The energy at each saddle-point is discretely calculated from the energy loss as a function of length that was experimentally measured using the Cherenkov spectral images. Thus, at each saddle-point, we subtract the appropriate

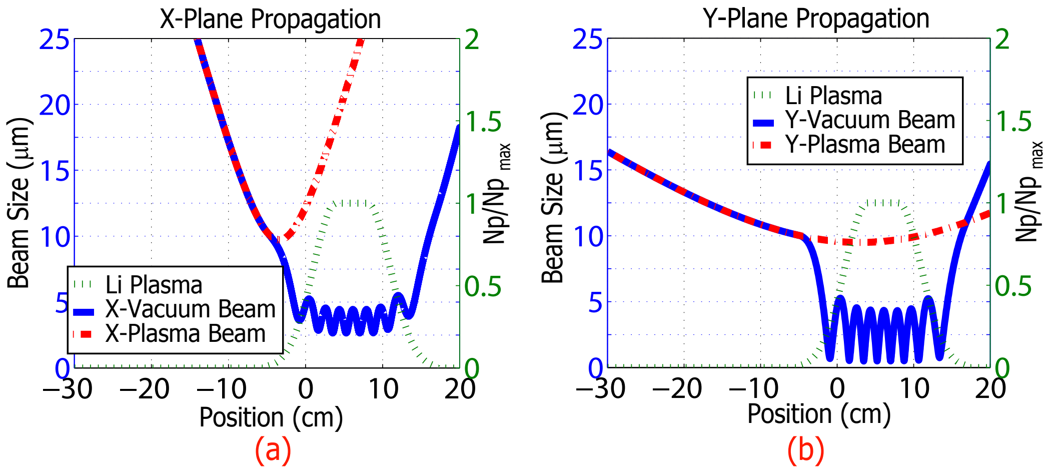

Figure 6.3: Plot showing vacuum and plasma propagation for both X and Y planes as the beam waist is moved. (a) X-plane propagation with the waist set at $z = -5cm$ leading to a $\sigma_x = 4\mu m$ radiating spot size. (b) X-plane propagation with the waist set at $z = 0cm$ leading to a $\sigma_x = 4\mu m$ radiating spot size. This assumes $n_{p,max} = 1 \times 10^{17} cm^{-3}$.

loss gradient multiplied by the distance traversed in the plasma. To get the proper match, an energy loss of 25 GeV/m needed to be assumed. This is somewhat larger than the average of 20 GeV/m. However, from figures 5.1c and 5.1d in chapter 5, we know that the majority of the radiating electrons are in the region of peak energy loss. Also, some electrons beyond $r = 2.5\sigma_r$ may be cut out of the ion column due to the collapse of the column near and immediately upstream of beam center (i.e. z=0). This could easily make up the difference between the energy loss used and the average that was computed.

For the second and third cases, with $n_{pe} = 6.4 \times 10^{16} cm^{-3}$ and $n_{pe} = 3.3 \times 10^{16} cm^{-3}$, the same analysis was performed as the one illustrated and described above. Figures 6.4c and 6.4d plot the average energy loss and the ion column charge for the $n_{pe} = 6.4 \times 10^{16} cm^{-3}$ case versus CTR signal. This case had a mean CTR signal of ≈ 175. Thus, the ion column charge was $N_{bi} \approx 8.2 \times 10^9$ with a mean energy loss of 1.9 GeV over a $FWHM = 14$ cm. Figures 6.4e and 6.4f similarly show the average energy loss and the ion column charge for the $n_{pe} = 3.3 \times 10^{16} cm^{-3}$ case. This case had a mean CTR signal of ≈ 300. Thus, the ion column charge was $N_{bi} \approx 8.25 \times 10^9$ with a mean energy loss of 1.7 GeV over a $FWHM = 16$ cm. Table 6.2 compiles all of the inferred parameters from the various analysis discussed

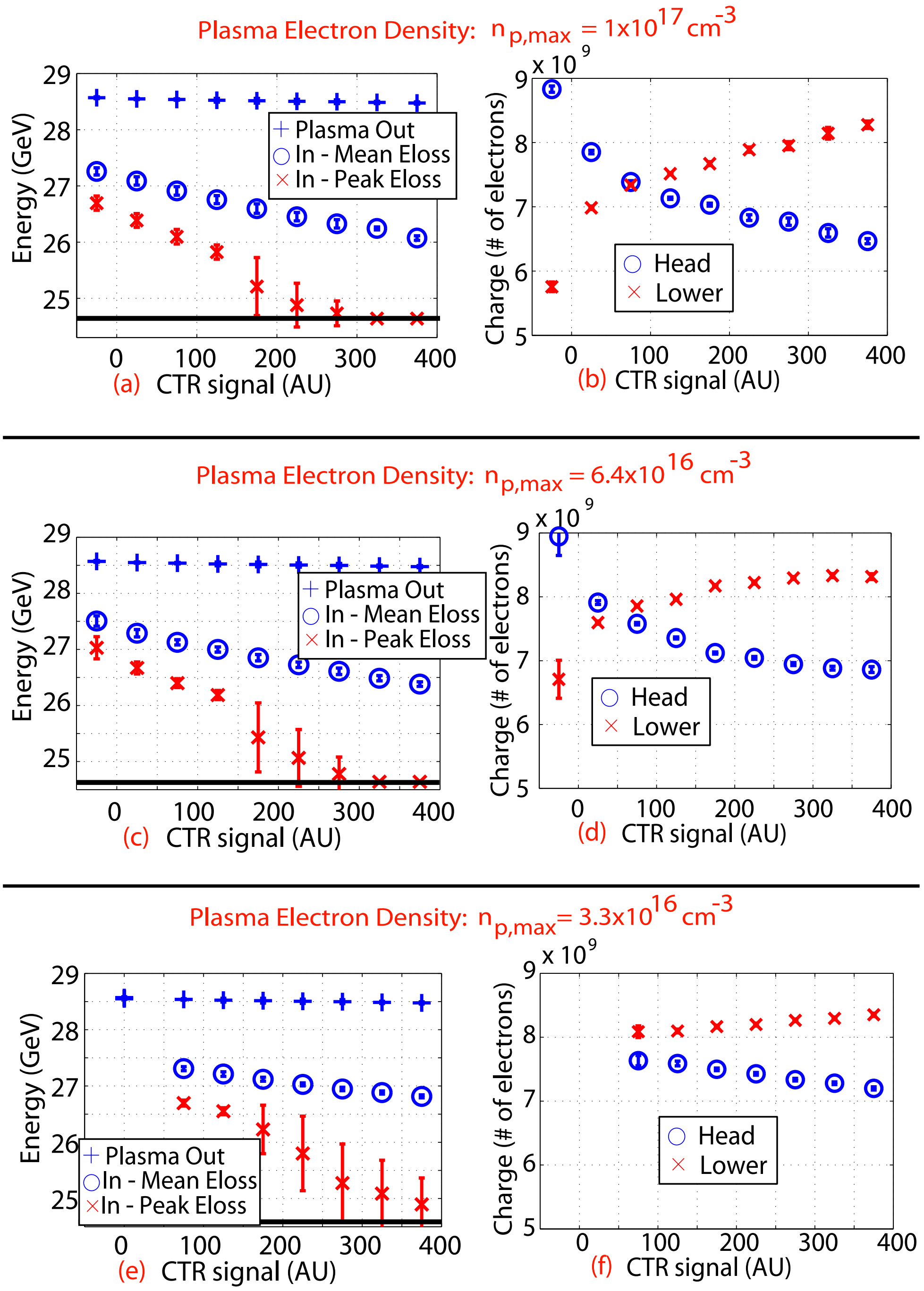

Figure 6.4: (a)(c)(e) The average energy with plasma out (blue +), the average energy loss in the Lower region with plasma (blue circle), and the peak energy loss with plasma defined by the 1 percent charge contour (red x) versus CTR signal for $n_{pe} = 10$, 6.36, and $3.33 \times 10^{16} cm^{-3}$, respectively. (b)(d)(f) The charge in region (1) of the bunch (Head) and in region (3), the radiating portion of the bunch (Lower) versus the CTR signal for $n_{pe} = 10$, 6.36, and $3.33 \times 10^{16} cm^{-3}$, respectively..

Case	1	2	3
Density (cm^{-3})	1×10^{17}	6.4×10^{16}	3.3×10^{16}
Oven FWHM (cm)	11	14	16
Saddle-Points	6	6	5
Average CTR signal	~ 85	~ 175	~ 300
Ion Column Charge	7.2×10^9	8×10^9	8.25×10^9
Ion Column Radius (μm)	4	5	7
Wakeloss (GeV/m)	25	15	11

Table 6.2: This table lists the pertinent simulation parameters for each of the cases in figure 6.5.

in chapter 5. These are the parameters used for the calculated curve fits. Note that the energy loss for a given CTR signal increases with plasma density as expected.

Figures 6.5a, 6.5b and 6.5c show the theoretically computed spectra versus the experimentally measured spectra using the parameters listed in table 6.2 for the $n_{pe} = 1 \times 10^{17} cm^{-3}$, $n_{pe} = 6.4 \times 10^{16} cm^{-3}$ and $n_{pe} = 3.3 \times 10^{16} cm^{-3}$ cases, respectively. The agreement for the $n_{pe} = 1 \times 10^{17} cm^{-3}$ and $n_{pe} = 6.4 \times 10^{16} cm^{-3}$ cases is excellent. The $n_{pe} = 3.3 \times 10^{16} cm^{-3}$ case is not as perfect. This is probably due to the low signal at the lower densities. This creates a lower signal-to-noise ratio which in turn makes each "noise" signature more damaging to the overall measurement.

To understand the fluctuations seen in figures 6.5a, 6.5b and 6.5c, an understanding of the method of data taking is necessary. Within each data set, there were generally 400 shots taken at 1 Hz. Thus, there were 400 seconds for beam variations to occur. Above we mentioned that the parameters affecting the radiated X-ray energy and the ultimate position yield are N_{bi}, γ and $\sigma_{i:x,y}$. However, the greatest impact is due to N_{bi} and γ since field ionization and ion column physics will limit the longitudinal and radial extent of the radiating electrons. These variations are clearly seen in Figure 6.5. For example, the 18 and 19 MeV bins in the $n_{pe} = 6.4 \times 10^{16} cm^{-3}$ of figure 6.5b deviate from the theory curve. This is due to an increased CTR energy (i.e. shorter σ_z and therefore a larger energy loss) at these

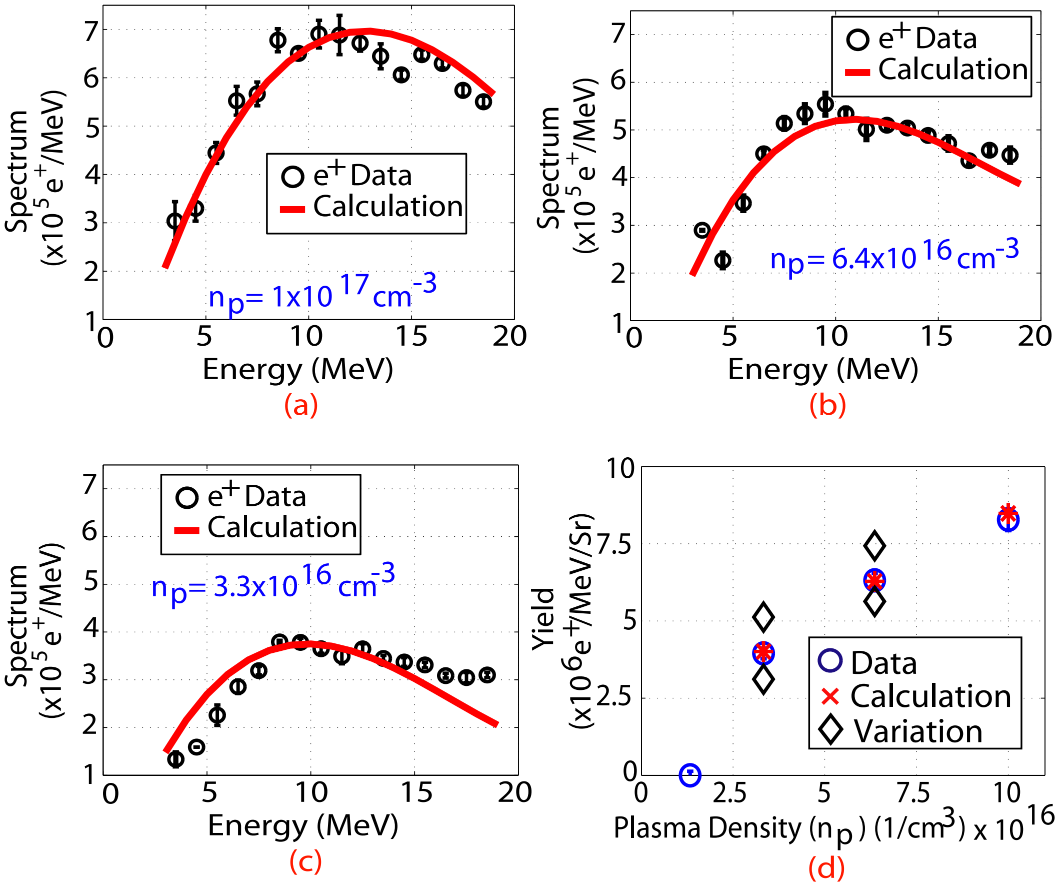

Figure 6.5: (a) Measured and calculated positron spectrum for $n_{pe} = 1 \times 10^{17} cm^{-3}$. (b) Measured and calculated positron spectrum for $n_{pe} = 6.4 \times 10^{16} cm^{-3}$. (c) Measured and calculated positron spectrum for $n_{pe} = 3.3 \times 10^{16} cm^{-3}$. (d) Integrated positron yield in the 4-20 MeV energy range versus the plasma density. The "variation" in the calculated value corresponds to the yield obtained using an rms electron beam spot size of $\pm 0.5 \mu m$ compared to its value used for the point marked by the red "x" (calculation).

values. This created more X-ray radiation, and thus positrons, for these two bins. The 16 and 17 MeV bins in the $n_{pe} = 3.3 \times 10^{17} cm^{-3}$ of figure 6.5c case have the same issue. These variations are common since the linac is in constant fluctuation. The optimal CTR energy will be discussed later in the chapter.

6.4 Density Vs. Yield

A pertinent scaling law that is important to address is the plasma density versus integrated positron yield. This measurement was performed at $n_{pe} = 1.33$,3.33,6.36 and $10 \times 10^{16} cm^{-3}$. The results are plotted in figure 6.5d along with the theoretically computed yield. In an ideal world (i.e. an electron beam propagating through a uniform ion column), the total X-ray yield should scale as n_{pe}^2. EGS4 simulations predict that given the same beam conditions (N_b, γ and $\sigma_{i:x,y}$) the positron yield in the measured range of 4-20 MeV should scale as n_{pe}^2. However, it is clear from the plot that this is not the case. The QuickPIC simulation and beam envelope model can address this difference. The deviation from the ideal scaling law can be attributed to three issues. First, as mentioned earlier, the ramped density profile of the plasma will create a lens. The lower density cases will ultimately lead to a larger transverse beam size within the plasma due to the n_{pe} dependence of the transverse focusing force. The beam envelope model predicts $\sigma_{i:x,y} = (4, 4)\mu m$, $\sigma_{i:x,y} = (5, 5)\mu m$, and $\sigma_{i:x,y} = (8, 8)\mu m$ for the $n_{pe} = 10, 6.36$ and $3.33 \times 10^{16} cm^{-3}$ cases, respectively. In general, we have argued that the large beam radius does not lead to a larger positron yield since the electron beam is already on the outer edge of the ion column. This is true when comparing two cases with the same plasma density. However, since the maximum ion column radius scales as $n_{pe}^{-1/2}$ for a Gaussian beam [38], the lower plasma density cases can have the same distribution of beam electrons in the ion column with a larger $\sigma_{i:x,y}$. Thus, the r_β^2 dependence is a factor between two cases with different densities. This is illustrated using QuickPIC simulations in figures 6.6a, 6.6c and 6.6e for our $n_{pe} = 10, 6.36$ and 3.33×10^{16} cases, respectively. These show plasma electron density contours for our three cases with the peak density region of the plasma profile shown in figure 6.3. The green arrow on each plot shows the maximum ion column radius $\sigma_{i,max}$ which scales as $1/\sqrt{n_{pe}}$ as discussed above. Perhaps the easiest way to visualize the ion column radius is to observe the focusing field relative to the pure ion column. Figures 6.6b, 6.6d and 6.6f plot the transverse electric field computed in QuickPIC as a function of transverse position at various longitudinal locations. The green dotted line on the plots shows the field of a pure ion column. Thus, $\sigma_{i,max}$ can be determined for each density as the point where the ion column electric field begins to deviate from the pure ion column. These radial locations are $x = 2.9\sigma_x$, $x = 3.6\sigma_x$ and $x = 4.8\sigma_x$ for the $n_{pe} = 10, 6.36$ and 3.33×10^{16} cases, respectively. Thus, the smaller focusing force in the ramped-density region of the plasma combined with the larger ion column as the density decreases will increase $\sigma_{i:x,y}$ of the beam within the peak density region of the plasma, resulting in a higher positron yield than that predicted by the n_{pe}^2 scaling.

Second, as the density increases, the ion column continues to encroach on the beam until outer beam electrons begin to leave the focusing region, eliminating x-ray radiation from these otherwise large-radius contributors. This can be observed in the longitudinal region of $z = (-.5\sigma_z) - 0$. Since the ionization front is in roughly the same location, the decreasing $\sigma_{i,max}$ will decrease the radial extent of the ion column at every location. Thus, near the front of the column, some loss of electrons is expected as the density increases. Third, the wake losses increase with density, further decreasing the positron yield. It is important to note that although the plasma density has changed for these cases, the ionization front has remained in the same location. This is expected since field ionization is not neutral density dependent, but rather beam density dependent.

Given the above information, a theory curve can be plotted on Figure 6.5d. The theoretical yield is found by integrating the spectral curves in figures 6.5a, 6.5b and 6.5c from 4-20 MeV. The ideal case plotted in figures 6.5a, 6.5b and 6.5c is denoted by the red "star". The "variation", denoted by the black "diamonds", in the calculated value corresponds to the yield obtained using an rms electron beam spot size of $\pm 0.5\mu m$ compared to its value for the ideal case marked by the red

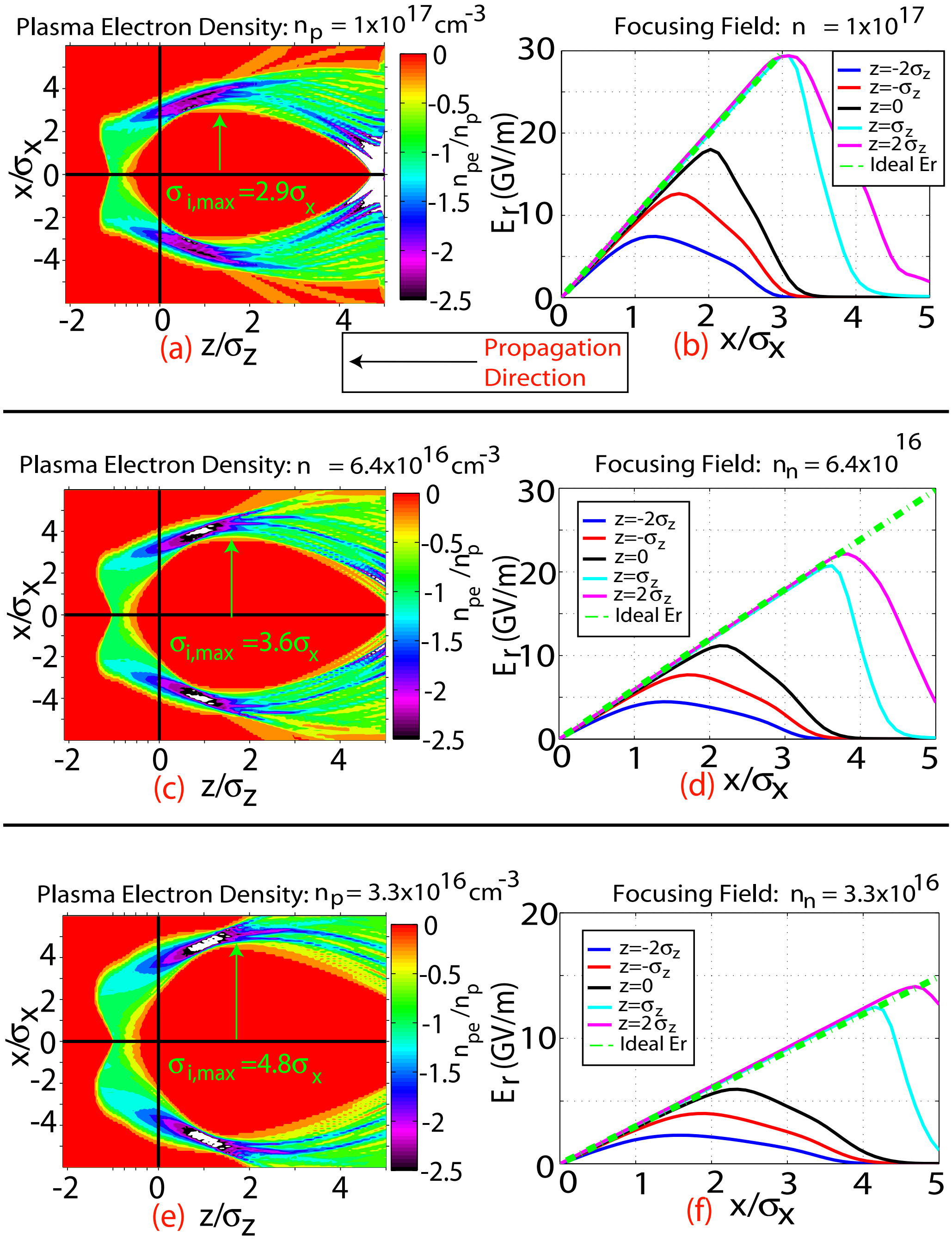

Figure 6.6: (a)(c)(e) QuickPIC simulation showing the plasma electron density contours for the $n_{pe} = 10$, 6.36, and $3.33 \times 10^{16} cm^{-3}$ cases, respectively. (b)(d)(f) Lineout of the QuickPIC simulation at various longitudinal locations showing the focusing force as a function of radius. The pure ion column case is also plotted for reference (green dotted line). The simulation assumes a gaussian beam with $N_b = 1.2 \times 10^{10}$ electrons, $\sigma_{i:x,y} = 11\mu m$ and $\sigma_z = 22.5\mu m$.

"star". The agreement between theory and measured data is excellent.

There are two aspects of the curve fits that are important in figure 6.5. First, there is the shape of the curve. This represents how well the theory fits the data. For the $n_{pe} = 1 \times 10^{17} cm^{-3}$ and the $n_{pe} = 6.4 \times 10^{16} cm^{-3}$ cases, the curve fits almost perfectly on top of the data at all energies. As mentioned above, the $n_{pe} = 3.3 \times 10^{16} cm^{-3}$ is not as great since it overshoots from 4-8 MeV and undershoots from 16-19 MeV. Second, there is the integrated yield. Clearly, the $n_{pe} = 1 \times 10^{17} cm^{-3}$ and the $n_{pe} = 6.4 \times 10^{16} cm^{-3}$ cases will have the same theoretical yield as the measured yield, but in this case the $n_{pe} = 3.3 \times 10^{16} cm^{-3}$ case does also. This shows that the spectral fit and the total yield are both important for determining the goodness of the theory. Changes in γ, r_β and N_{bi} can all effect the shape of the curve, and thus both plots must be shown when attempting to validate the experimental results with the simulation model.

6.5 Positron Spectral Variation

To show the sensitivity of the curve fit, we plot three different cases for $n_{pe} = 3.33 \times 10^{16} cm^{-3}$ in figure 6.7. This gives confidence that our model is working correctly and it also shows that the model is within an acceptable error. Small changes in r_β will effect the overall yield substantially. Figures 6.7a, 6.7b and 6.7c plot the theoretical positron yield versus the measured yield (same for all three plots) for a radius in the peak density region of the plasma of $\sigma_{i:x,y} = 7.5 \mu m$, $\sigma_{i:x,y} = 8.0 \mu m$ and $\sigma_{i:x,y} = 8.5 \mu m$, respectively. This gives another view of the spectral shape and yield sensitivity to small, unmeasurable changes in $\sigma_{i:x,y}$. With only a 4 percent change in $\sigma_{i:x,y}$, the poor curve fits are apparent, as they deviate from the amplitude of the good fit of figure 6.7b. These data offer "variation error bars" for the density scaling plot of figure 6.5d. The variation in the computed yield for the $n_{pe} = 3.33 \times 10^{16} cm^{-3}$ and $n_{pe} = 6.36 \times 10^{16} cm^{-3}$ cases are shown as black diamonds on the plot. This is designed to show the sensitivity of the positron amplitude to the experimental parameters (as long as $r_{i,max} > 3\sigma_{i:x,y}$). As mentioned earlier, note that the spectral shape does not change much, but it is generally the

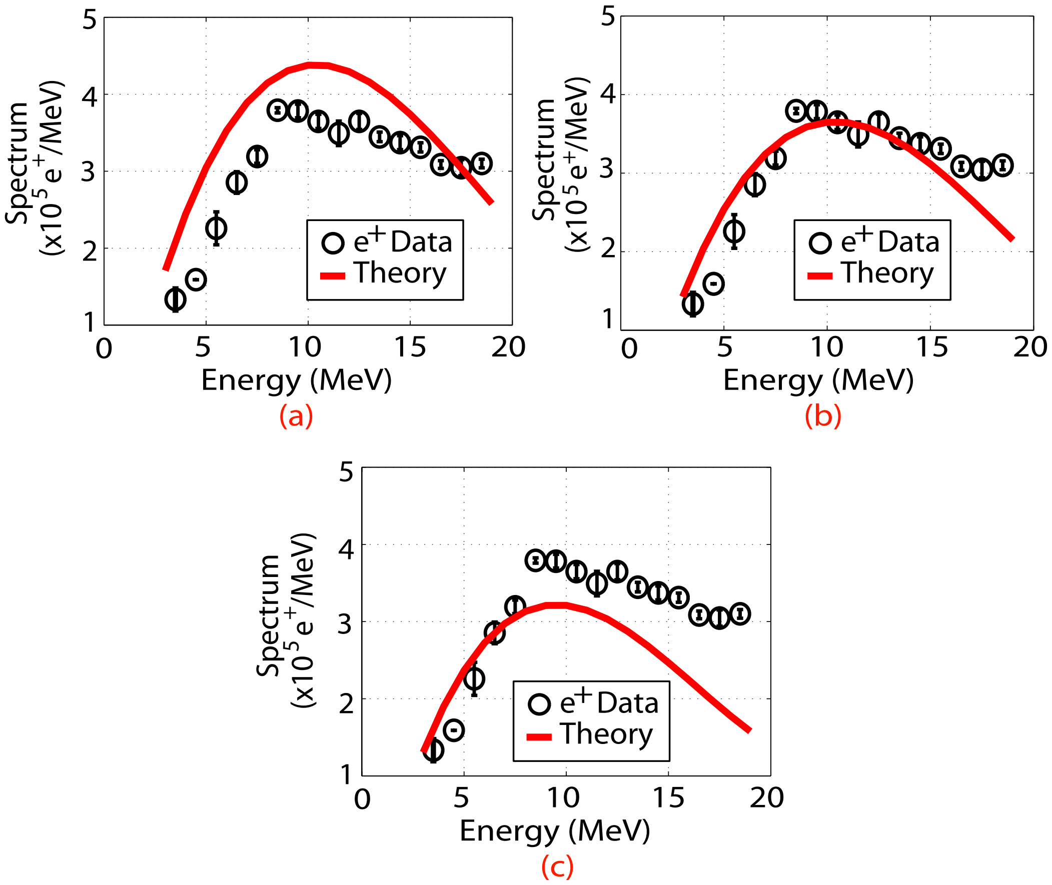
(a) (b) (c)

Figure 6.7: Measured and calculated positron spectrum for $n_{pe} = 3.33 \times 10^{16} cm^{-3}$. (a) Curve fit with $\sigma_{i:x,y} = 7.5\mu m$. (b) Curve fit with $\sigma_{i:x,y} = 8.0\mu m$. (c) Curve fit with $\sigma_{i:x,y} = 8.5\mu m$. All other parameters are equal between the cases.

amplitude that has the large variations as parameters are changed.

6.6 Yield vs. CTR Signal

To quantify the dependence of positron yield on the CTR signal, the following analysis was performed. With $n_{pe} = 1 \times 10^{17} cm^{-3}$, a total of 2800 shots were taken over our positron spectral range of 4-20 MeV. This data was averaged in CTR bins of 100. The amount of data taken allowed for accurate representation of the spectrum at the different CTR values. The Cherenkov energy loss analysis was performed and the result is shown in figure 6.8a. As expected, the number of electrons in the "lower" region (i.e. ion column) increases as the CTR signal increases. It is known that a higher CTR signal means a shorter bunch length which results in ionization and plasma blow out sooner in the bunch.

Figure 6.8b plots the experimentally measured positron yield from 4-20 MeV and the mean beam energy loss to the wakefield in the Lower Cherenkov region versus the CTR signal for the plasma density profile shown in Figure 6.3. The yield peak at the CTR signal of 200 is expected from the Cherenkov data. Initially, at a CTR value of 0, the positron yield is low. This is expected since we have a low amount of charge in the ion column. If you look at the proportion of yield for CTR bins of 0,100 and 200. There is a relative yield of 1.0, 1.18 and 1.40, respectively. Figure 6.8a shows that the increase in the charge in the ion column for the three cases is 1.0, 1.11, and 1.15, respectively. If the radiated X-ray energy and the positron yield were solely dependent upon the charge in the ion column, we would expect the charge increase to be 1.0, 1.18 and 1.40 due to the linear relationship between radiated energy and charge. However, this is not what is experimentally measured because the Cherenkov diagnostic cannot measure the individual radii of the electrons. With the low CTR signal, we have a longer bunch length. This leads to a smaller $r_{i,max}$ from the $1\sqrt{\sigma_z}$ dependence in equation 5.4 in chapter 5. The claim can be made that not only are there less particles in the ion column, but many of the $r_\beta > 2.5\sigma_r$ electrons may reside outside of the ion column. From figure 5.7d in chapter 5, we see that at full ionization the $z = -.5\sigma_z - 0$ electrons are barely in the ion column. This ion column will shrink proportional to $1/\sqrt{(\sigma_z)}$. Thus, we can expect that many $r_\beta > 2.5\sigma_r$ electrons will not reside in the column at the lowest CTR signal, eliminating many high energy radiators. Thus, the yield is artificially low. This effect is even greater since the average energy loss is 1.0, 1.21 and 1.45 respectively, which lowers the yield of the CTR bins of 100 and 200 relative to the CTR bin of 0.

The ion column effect will decrease as the CTR signal increases. Thus, beyond the CTR signal of 200, the charge in the ion column saturates and the yield begins to drop due to the losses to the wakefield. In other words, the increase in $r_{i,max}$ which increases the number of particles in the ion column can no longer keep up with the increasing energy loss of the radiating electrons to the wake. The relative yield between the CTR cases of 200, 300 and 400 is 1.0, .88 and .84, respectively.

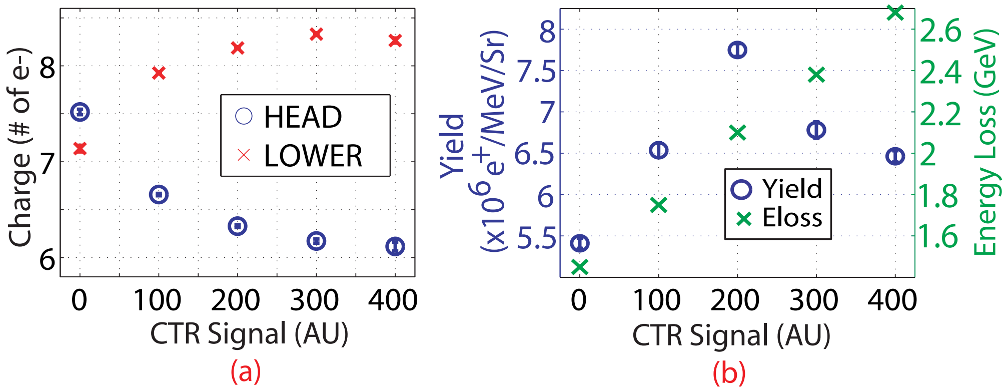

Figure 6.8: (a) The charge in region (1) (Head) of the bunch, and in region (3) the radiating portion of the bunch (Lower) versus the CTR signal. (b) The integrated positron yield in the 4-20 MeV energy range versus CTR signal for $n_{pe} = 1 \times 10^{17} cm^{-3}$. Also plotted is the average beam energy loss for the radiating electrons within the 11cm plasma (wake+radiation).

This drop is solely due to the energy loss to the wakefield. The CTR signal is increasing and σ_z of the beam is decreasing, leading to a larger wakefield. Since the charge in the ion column remains constant, the yield drops.

The fact that the different CTR bins have different electron beam distributions in the ion column creates a daunting task when attempting to fit this curve to theory. There are too many unmeasurable parameters continuously changing, making the theoretical fit unreasonable. However, qualitatively, the plasma physics surrounding the yield changes is understood.

In a later run, three different Li column lengths were used: 13 cm, 22.5 cm, and 30.5 cm at a higher density $n_{pe} = 2.73 \times 10^{17} cm^{-3}$. Figure 6.9 plots the measured integrated positron yield from 27-30 MeV versus CTR signal for the three oven lengths listed above. Note that this is a relative CTR signal and it is not correlated to that shown in figure 6.8 (i.e. different experimental setup). At low CTR signal, there is a large difference between the three oven cases. However, at high CTR signal, there is a reduced difference between the 13 cm and 22.5 cm cases, but there is no difference between the 22.5cm and 30.5 cm cases. This is due to energy loss to the wakefield. The wakefield at high CTR signals could not be measured since it was so large that most electrons losing energy were deflected below the measurement

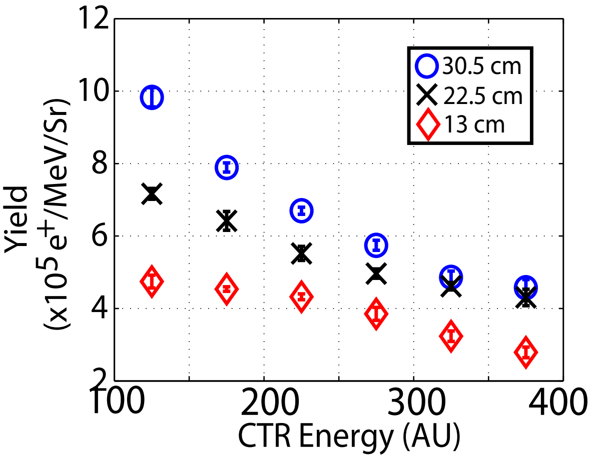

Figure 6.9: Integrated positron yield in the 27-30 MeV energy range versus CTR signal for 3 different plasma lengths with $n_{pe} = 2.7 \times 10^{17} cm^{-3}$. Note that the CTR signal bins are different from those in figure 6.8. The data was taken with different experimental setups.

range of the Cherenkov diagnostic and were not collected. However, we know that the γ^2 dependence plays a large role at this density since the energy loss is about 40 GeV/m. Eventually, with these wakefields, the electron energy reduces to where ω_c of the spectrum is at or below 1 MeV. At this point, the radiation no longer contributes to the positron spectrum.

Another important result can be taken from figure 6.9. The energy loss calculation for this data was more challenging because for the majority of the cases the mean position of the energy loss was physically below the measurement range of the Cherenkov diagnostic. However, for the CTR energy of 175 case, the energy loss could be measured. Table 6.3 lists the relative parameters between the three oven length cases at the CTR energy of 175. The energy loss for this CTR bin was 3.1 GeV, 3.8 GeV, and 4.7 GeV for the 13 cm, 22.5 cm, and 30.5 cm cases, respectively as illustrated in figure 6.9. This can be used to estimate the theoretical change in yield between the three cases. If little energy was lost to the wake, the increase in yield would scale linearly with the length. There is also electron beam radiation loss to the synchrotron X-rays, but this value is not important as the wakeloss exceeds the radiation loss by an order of magnitude at this plasma density, except for a few large radius contributors. The relative yield is 1.0, 1.47, and 1.84 between the

Case	1	2	3
Plasma Length (cm)	13	22.5	30.5
Wakeloss (GeV)	3.1	3.8	4.7
Average Beam Energy (GeV)	26.95	26.6	26.15
Estimated e^+ Yield	1.0	1.55	1.97
Measured e^+ Yield	1.0	1.47	1.87

Table 6.3: This table lists the plasma length, measured wakeloss, calculated e^+ yield, and the measured e^+ yield for the 175 CTR bin from figure 6.9.

three cases as shown in table 6.3. Since the yield is a function of γ^2, the expected difference in yield can be calculated using the wakeloss. The average energy of the beam within each length is the initial beam energy of 28.5 GeV minus half of the wakeloss for that length. This gives average energies of 26.95 GeV, 26.60 GeV, and 26.15 GeV for the 13 cm, 22.5cm and 30.5 cm cases, respectively. The is another effect that contributes to the yield for these cases. The length of the oven is defined by the FWHM of the Li oven profile. However, since the density is large in these cases at $n_{pe} = 2.73 \times 10^{17} cm^{-3}$, the length of the oven is actually a bit longer since saddle-points occur even on the edges of this high-density plasma. The beam envelope code verifies this claim. Thus, the length for each oven is actually about 3 cm longer. To get the relative yield, the wakeloss and the length are taken into account. The yield has a γ^2 and L_p dependence. Thus, we would expect the relative yields to be $[26.95^2 * (13 + 3)]$=11621 (AU), $[26.6^2 * (22.5 + 3)]$=18403 (AU) and $[26.15^2 * (30.5 + 3)]$=22908 (AU) for the 13 cm, 22.5 cm and the 30.5 cm ovens, respectively. This gives calculated relative yields of 1.0, 1.55 and 1.97, respectively. These are very similar to the 1.0, 1.47 and 1.84 measured relative yields quoted in table 6.4. The calculated scaling does shows that the data are within the range of acceptable errors.

6.7 Waist vs. Yield

We have discussed the scaling laws with density n_{pe}, the number of electrons in the ion column N_{bi}, the electron energy γ, and the radius of the electron oscillating inside the peak density region of the plasma $\sigma_{i:x,y}$. Another method of verifying the N_{bi} and γ dependence is shown in figure 6.10. This figure plots the charge distribution in the head [region (1)] and lower [region (3)] regions for five different X-waist locations with $n_{pe} = 6.36 \times 10^{16} cm^{-3}$, and it also plots the measured integrated positron yield from 4-20 MeV for each of the five waist locations. Since $\beta_y \gg \beta_x$, the Y-waist change led to small changes in the overall yield. Thus, the Y-waist remained fixed while data was taken. The nominal waist locations where the analysis of this chapter took place were with the X-waist set at $z = -5$ cm and the Y-waist set at $z = 0$ cm relative to the plasma entrance. Figure 6.10c represents this location and is denoted by X-waist=0.0cm and Y-waist=0.0cm. All X-waist positions are relative to this point. The negative X-waist locations mean that the waist was moved upstream of the plasma entrance and the positive waist locations mean that the X-waist was moved downstream of the plasma entrance. As expected, the charge distribution in figure 6.10c is closely correlated to those presented in figure 6.4 which plots data at the same waist location.

For the analysis, the orange lines were placed on figures 6.10a-6.10e to show the average CTR energy for that data set. This is important since the CTR energy affects the σ_z of the beam which determines the wakefield driven in the plasma. When the waist is moved from the nominal waist locations of figure 6.10c in either direction, the charge in the ion column decreases. At the X-waist position of +30cm of figure 6.10e, the ion column charge is nearly 30 percent less than the peak charge of figure 6.10c. This loss of charge in the ion column is expected since our small β_x leads to an increased vacuum beam size of the electron beam before it enters the ramped-density profile of the plasma. This change in the beam size in the X-plane was illustrated in figure 5.4 in chapter 5. The larger beam size leads to a lower peak current (larger σ_z) which causes ionization to occur later in the bunch, decreasing the number of electrons radiating in the ion column. Due to the decrease in N_{bi},

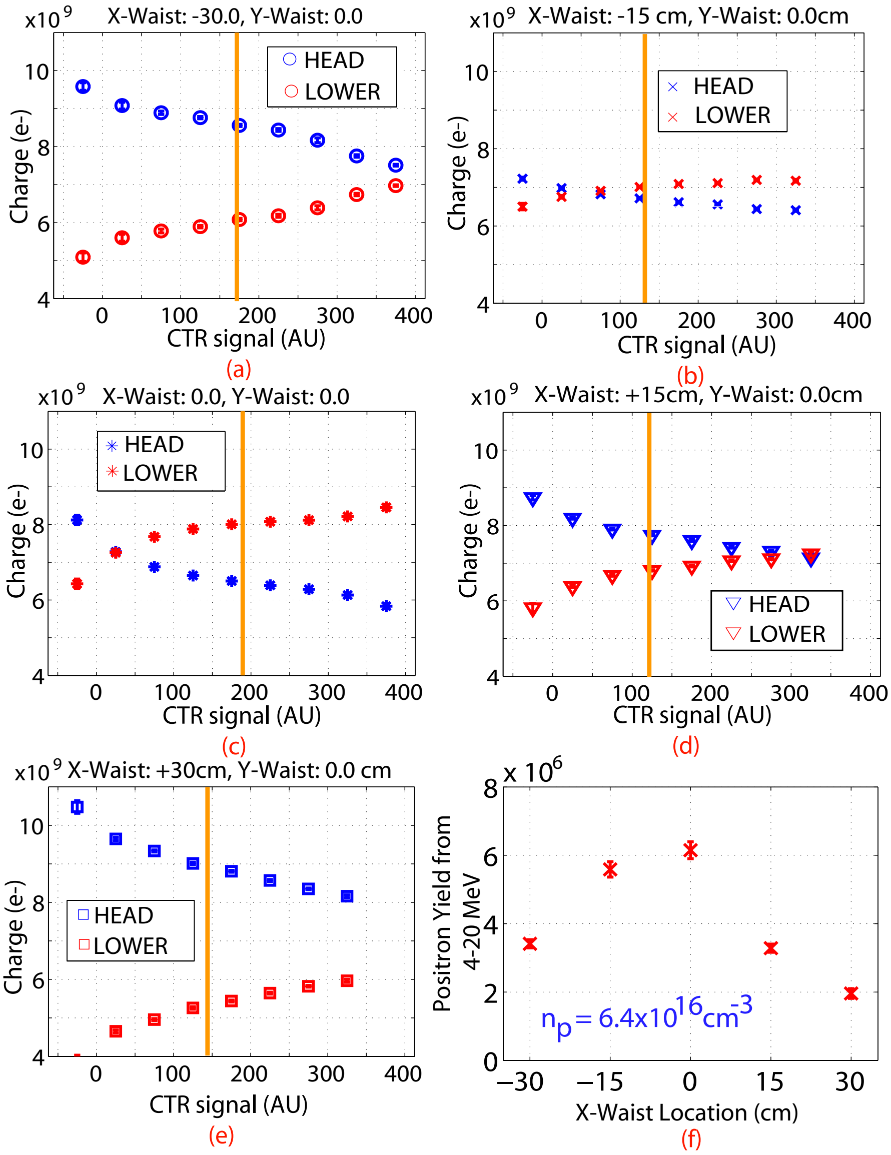

Figure 6.10: Plot of the experimentally measured charge in the ion column using the Cherenkov analysis versus X-waist locations of (a) -30 cm, (b) -15 cm, (c) the nominal 0 cm, (d) +15 cm and (e) +30 cm. The orange line denotes the average CTR energy for each run. (f) The measured integrated positron yield from 4-20 MeV for the five X-waist locations plotted in (a)-(e).

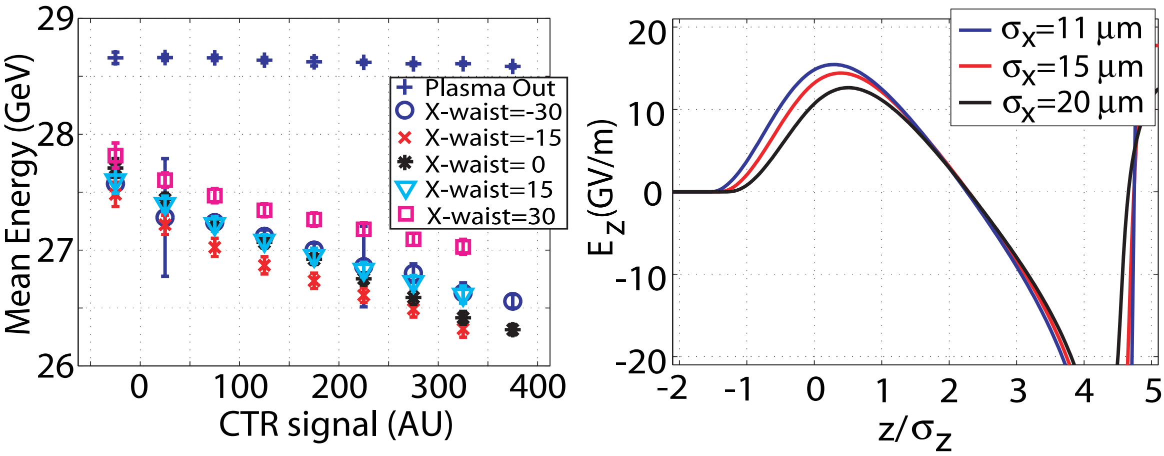

(a) (b)

Figure 6.11: (a) Plot of the average beam energy without plasma (blue +) and the average energy loss with plasma for the 5 previously listed cases. All data was taken with $n_{p,max} = 6.4 \times 10^{16} cm^{-3}$. (b) A QuickPIC simulation with $n_{pe} = 6.4 \times 10^{16} cm^{-3}$,$N_b = 1.2 \times 10^{10}$, $\sigma_y = 11\mu m$ and $\sigma_z = 22.5\mu m$, showing the change of the longitudinal wakefield as σ_x of the beam is varied (i.e. as the X-waist is changed).

the total integrated positron yield will drop on either side of the peak as observed in figure 6.10f. In general, the amplitude of the wakefield does not change with σ_r [38]. However, for large changes in σ_r, there is a small, but measurable, effect on the wakefield driven in the plasma. The average energy loss for the N_{bi} electrons for all five X-waist locations is plotted in figure 6.11a. It is clear that the average energy loss does change between the cases. The QuickPIC simulation in figure 6.11b verifies that this is expected. The simulation shows the on-axis longitudinal wakefields for three cases with $n_{pe} = 6.4 \times 10^{1}6cm^{-3}$,$N_b = 1.2 \times 10^{1}0$, $\sigma_y = 11\mu m$ and $\sigma_z = 22.5\mu m$. The value of σ_x was varied from $11\mu m$, $15\mu m$, and $20\mu m$ for the three cases, respectively. The change in the on-axis longitudinal wakefield between the $11\mu m$ and $20\mu m$ cases is about 20 percent. However, this effect is still far less than the scaling of the wakefield to σ_z of the bunch.

Table 6.4 compares the pertinent parameters that effect the positron yield for the five X-waist cases plotted in figure 6.10. The total integrated positron yield will scale as N_{bi} if all variables are kept constant (n_{pe},γ,r_β). However, table 6.4 shows that this is clearly not the only important scaling. For example, the X-waist=0 cm and the X-waist=-15 cm cases have a 9 percent change in yield. At first glance, it may appear obvious to assume that the change in yield is due solely to N_{bi} which changes by 12 percent between the two cases. The wakeloss increases by 20 percent in the X-waist=-15cm case. However, since the difference in energy between the two cases is only 0.3 GeV (i.e. 1.9-1.6 GeV), or only 1 percent of the 28.5 GeV beam energy, this will only lower the positron yield slightly for the X-waist=-15cm case relative to the X-waist=0 cm case. Since the X-waist has been pulled upstream, σ_x of the electron beam will be larger when it enters the ramped density region of the plasma. This will decrease N_{bi}, as observed, but it will also lead to a larger σ_x in the peak density region of the plasma for the electrons that do reside in the ion column. Thus, there is a smaller N_{bi} and a larger wakefield in the X-waist=-15 cm case, decreasing the yield. Yet, there is a larger σ_x inside the peak density region of the plasma, increasing the yield. Recall from figure 5.6 in chapter 5 that an increase of 37 percent in theoretical yield was shown when the beam radius increased from $\sigma_x = 5\mu m$ to $\sigma_x = 8\mu m$ while σ_y remained constant. All three of these scaling laws will combine to give the 9 percent decrease in yield observed between these two cases.

When the X-waist is now moved further upstream to -30cm, the σ_x of the beam is so large that the ionization occurs much later in the beam. This results in a smaller N_{bi}, as measured to be 25 percent less than the nominal case. This further decreases the yield relative to the X-waist=0 case.

If the X-waist is moved upstream of the plasma entrance, as for the X-waist=-15 cm and -30 cm cases, the ionization front in the plasma is determined by the initial contact with the Li vapor. When the longitudinal position within the electron bunch is reached where the peak radial electric field is greater than 6 GV/m (the ionization potential of Li, see chapter 2), the Li vapor will ionize and the electrons downstream of this longitudinal position in the bunch will focus down due to the ramped density profile of the plasma. The electrons upstream of this ionization front will never ionize the Li vapor because they have already propagating through the vacuum waist and are now defocusing. However, when the waist is moved downstream into the plasma as in the X-waist=+15 and +30 cases, a different effect will result. Ionization occurs initially at the longitudinal position in the beam where the beam radial electric field exceeds 6 GV/m, as in the previous case. However, the electrons upstream of this position continue to focus in the Li vapor since the vacuum waist is within the Li vapor profile. Thus, as the upstream electrons focus, the 6 GV/m threshold for field ionization will move forward in the bunch. Eventually, many of these focusing electrons will ionize the Li vapor upstream of the initial ionization front, adding more electrons to the ion column. These electrons will lose less energy because they have not propagated in plasma for the same distance as those in the rear of the bunch whose radial electric field ionized the Li vapor immediately. This result is observed in the table 6.4. When the X-waist=+30 cm, the beam has a higher average CTR signal than the case a 0 cm. A higher CTR should translate to a larger wake and more energy loss. Instead, the X-waist=+30 cm case has a smaller average average wakeloss of 1.3 GeV relative to the 1.6 GeV average wakeloss of the X-waist=0cm case. Ultimately, this means that these electrons upstream of the initial ionization front, that continue to focus once in the Li vapor, experience less plasma length in the ion column than the electrons in the rear of the bunch. This manifests itself in our physical model as less saddle-points for these upstream electrons, and thus less radiation.

With this analysis, it is expected that the X-waist=-15 and X-waist=+15 cases would have large differences in their overall yield, even though they have roughly the same number of electrons in the ion column.

Another important point can be taken from the ion column charge distribution. The radiated energy scales as r_β^2. Thus, if this was the entire theory, we would expect that the Xwaist=+-30cm cases would have the highest positron yields even though there are less electrons in the ion column. After all, even if the ionization front is later, the r_β^2 dependence is more dominant than the linear dependence on charge and will lead to an increase in positron yield. Instead, we see a 50-75 percent reduction in yield on either side of the peak. This is due to the ion column radius.

X-waist (cm)	CTR average	Wakeloss (GeV)	N_{bi}	Relative e^+ Yield
-30	173	1.7	6.0×10^9	.55
-15	187	1.9	7.1×10^9	.91
0	135	1.6	8.0×10^9	1
$+15$	122	1.5	6.8×10^9	.53
$+30$	147	1.3	5.4×10^9	.32

Table 6.4: This table lists the pertinent scaling values for the five X-waist positions discussed at $n_{pe} = 6.4 \times 10^{16} cm^{-3}$. The table lists the average CTR energy for each case. The wakeloss, N_{bi} and relative e^+ yield are quoted from this average CTR energy value for each case.

It was stated above in equation 5.4 that the ion column radius is not a function of σ_r, but rather a function of σ_z and n_{pe}. Thus, as σ_r increases at the entrance to the plasma, and as σ_r inside the ion column increases, $r_{i,max}$ stays exactly the same. This leads to more electrons being excluded from the ion column transversely. The beam may be larger inside the peak density portion of the plasma, but most of the large radius electrons are outside of the ion column, and are not contributing to the X-ray radiation and the overall positron yield.

6.8 Conclusion of Results

Many data sets have been presented to show the scaling laws for the radiated X-ray energy and the ultimate positron yield in a plasma wiggler. It can be concluded from the above analysis that the strongest dependence for the positron yield resides on the charge in the ion column N_{bi} and the electron energy γ which is correlated to the energy loss to the wakefield. The r_β^2 dependence is great in theory for increasing the positron yield, however, the ion column radius is purely a function of σ_z, N_b and n_{pe}. A larger beam will exclude electrons longitudinally and transversely from the ion column, rendering the r_β^2 dependence neutral.

The results show good agreement with theory. Thus, we can be confident that this model can be extended to design a positron source using optimized parameters.

Sources can still be developed with the correct set of experimental parameters that maximize the ion column radius while minimizing the wake. These parameters will be discussed in the next chapter.

CHAPTER 7

Future Work

In this thesis, a new mechanism for producing positrons, namely a thin target positron source that is driven by betatron radiation produced in an ion column, has been proposed and experimentally demonstrated. The experiments were carried out parasitically to the Plasma Wakefield Accelerator (PWFA) experiment. As such, the beam and plasma parameters were varied in a narrow window about their optimum values for the PWFA experiment. In this chapter, we discuss how in the future a more optimized positron production experiment might be performed. The previous chapter discussed the three major factors that effected the positron yield: the number of particles in the ion column N_{bi}, the energy of the radiating electron γ (i.e the effect of the wakefield loses), and the radius $\sigma_{i:x,y}$ of the beam. However, it was stated that increasing $\sigma_{i:x,y}$ can be rendered insignificant if the radius of the ion column $r_{i,max}$ is not large enough to support the electrons at the larger radius. If a positron source is to be designed by this method, we will need to optimize it using the scaling laws that we have learned from running a variety of QuickPIC cases along with the synchrotron model used in tandem with EGS4.

7.1 Source Optimization

For the parameter optimization, we are assuming a 3-D Gaussian electron beam. The total charge N_b and the spatial dimensions (σ_x, σ_y, σ_z) of the beam will be given for each case. All cases in this chapter are azimuthally independent. Thus, both σ_x and σ_y will be referred to as σ_r.

It is important to note what is needed if this system is to be upgraded into a positron source. We need a plasma source with a short or no density ramp since this ramped profile will focus the electron beam to a smaller spot size, decreasing the X-ray and positron yields. Also, we need the largest radius ion column possible with the largest beam possible (recall from chapter 5 that $r_{i,max} \propto (N_b, 1/n_{pe}, 1/\sigma_z)$), and the smallest peak wake energy loss $E_{z,peak}$ possible with an ionization front that is as far forward as possible. If the ionization front is far enough forward in the beam and the plasma wavelength λ_p is small enough, one could have particles between $1 - 3\sigma_z$ that are radiating *and* accelerating. This would create a group of electrons that radiate X-rays while gaining more energy from the wake. This will be discussed further below.

The current scaling laws that are known are the total radiated synchrotron energy per unit distance $dW/dz \propto (n_{pe}^2, \gamma^2, r_\beta^2)$ and the critical energy of the radiated spectrum $E_c \propto (n_{pe}, \gamma^2, r_\beta)$. A typical low-K, magnetic wiggler positron source is described by Flottmann [7]. In this scheme, a 150 GeV electron beam is sent through a 35 m long wiggler, creating 370 photons/electron with an average photon energy of 10 MeV. This system will collect about 1.5 positrons/electron with positrons in the energy range of 2-20 MeV. Thus, the goal of this source design exercise is to create a comparable thin target source with a 1 m plasma that will yield $\approx 1 - 2$ positrons/beam electron with positron energies from 2-20 MeV.

7.1.1 Charge in the Gaussian Beam

One parameter that is simple to adjust experimentally is the beam charge N_b. Figure 7.1 shows the longitudinal and the transverse focusing fields of a 3-D Gaussian beam with $\sigma_r = 15\mu m$ and $\sigma_z = 22.5\mu m$ for three different charge cases: $N_b = 1 \times 10^{10}$, $N_b = 2 \times 10^{10}$ and $N_b = 4 \times 10^{10}$. The longitudinal fields are plotted for the $r = 0$, $r = \sigma_r$, $r = 2\sigma_r$ and $r = 3\sigma_r$ radii, and the transverse focusing fields are plotted for $z = -\sigma_z$, $z = -.5\sigma_z$, $z = 0$, $z = \sigma_z$ and $z = 2\sigma_z$. The ideal electric field E_r of a pure ion column is also plotted for reference. Note that $z = 0$ denotes the center of the electron beam and $\sigma_z < 0$ denotes the front portion of the electron beam.

Figure 7.1a shows that the $N_b = 1 \times 10^{10}$ case has the smallest wakefield. This is good for radiated X-ray energy per electron. However, figure 7.1b shows why this case is totally impractical for a positron source. The pure ion column is never larger than $\sim 1.5\sigma_r$. Thus, we have already eliminated most of our high energy radiators. The $N_b = 2 \times 10^{10}$ case of figures 7.1c and 7.1d suffer from the same issue. The ion column is not fully developed, even though it moves out to $\sim 2\sigma_r$ in this case. The $N_b = 4 \times 10^{10}$ case of figures 7.1e and 7.1f is the most promising of the three. The peak wakeloss has increased to 41 GeV/m, but this is located at $z = 0$ where the pure ion column only extends out to $\sim 2\sigma_r$. The pure ion column exists only beyond $z = \sigma_z$. At this longitudinal position from $z = 1 - 3\sigma_z$, the wakefield moves from 32 GeV/m of energy loss to 15 GeV/m of energy gain. Thus, the electrons in the pure ion column are losing far less energy than the peak energy loss, and some are even gaining energy.

This figure gives the first scaling law for a 3-D Gaussian beam. As shown in figures 7.1a, 7.1c and 7.1e, the peak energy loss for the $N_b = 1 \times 10^{10}$, $N_b = 2 \times 10^{10}$ and $N_b = 4 \times 10^{10}$ cases is 21.2 GeV/m, 31.7 GeV/m and 42.7 GeV/m, respectively. This gives a peak wake energy loss scaling of $E_{z,peak} \propto \sqrt{N_b}$.

7.1.2 Bunch Length

Another parameter that is simple to adjust experimentally, but is not easy to measure when the electron beam is less than 100 fs long is the bunch length σ_z. Figure 7.2 shows the longitudinal and the transverse focusing fields of a 3-D Gaussian beam with $\sigma_r = 15\mu m$ and $N_b = 4 \times 10^{10}$ for three different bunch lengths: $\sigma_z = 22.5\mu m$, $\sigma_z = 27.5\mu m$ and $\sigma_z = 32.5\mu m$. This figure plots the same longitudinal and transverse positions as figure 7.1.

The strongest dependence on $E_{z,peak}$ depends on σ_z. Figures 7.2a, 7.2c and 7.2e have bunch lengths of $\sigma_z = 22.5\mu m$, $\sigma_z = 27.5\mu m$ and $\sigma_z = 32.5\mu m$, respectively. These cases have $E_{z,peak}$ values of 42.7 GeV/m, 35 GeV/m and 29.2 GeV/m, respectively. This gives a scaling of $E_{z,peak} \propto 1/\sigma_z$.

It is clear from figures 7.2b, 7.2d and 7.2f that a $\sigma_r = 15\mu m$ case is not optimal for generating betatron photons as many of the electrons do not reside in the pure ion column. The $\sigma_z = 22.5\mu m$ case of figures 7.2a and 7.2b give the most optimal

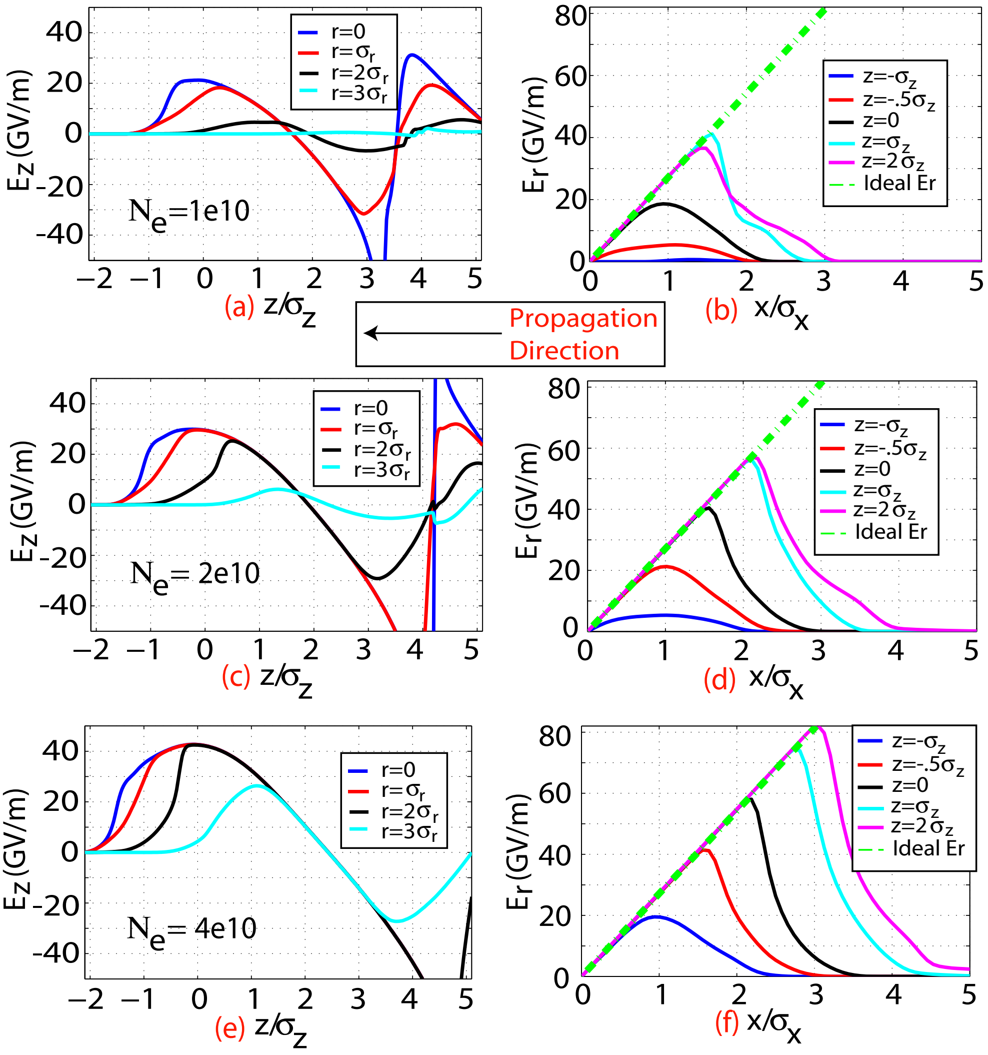

Figure 7.1: Plots the longitudinal and transverse fields in a field ionized plasma plasma of density $n_{pe} = 2 \times 10^{17} cm^{-3}$ from a $\sigma_r = 15\mu m$ and $\sigma_z = 22.5\mu m$ electron beam with three different N_b values. (a) Longitudinal fields for $N_b = 1 \times 10^{10}$. (b) Transverse fields for $N_b = 1 \times 10^{10}$. (c) Longitudinal fields for $N_b = 2 \times 10^{10}$. (d) Transverse fields for $N_b = 2 \times 10^{10}$. (e) Longitudinal fields for $N_b = 4 \times 10^{10}$. (f) Transverse fields for $N_b = 4 \times 10^{10}$.

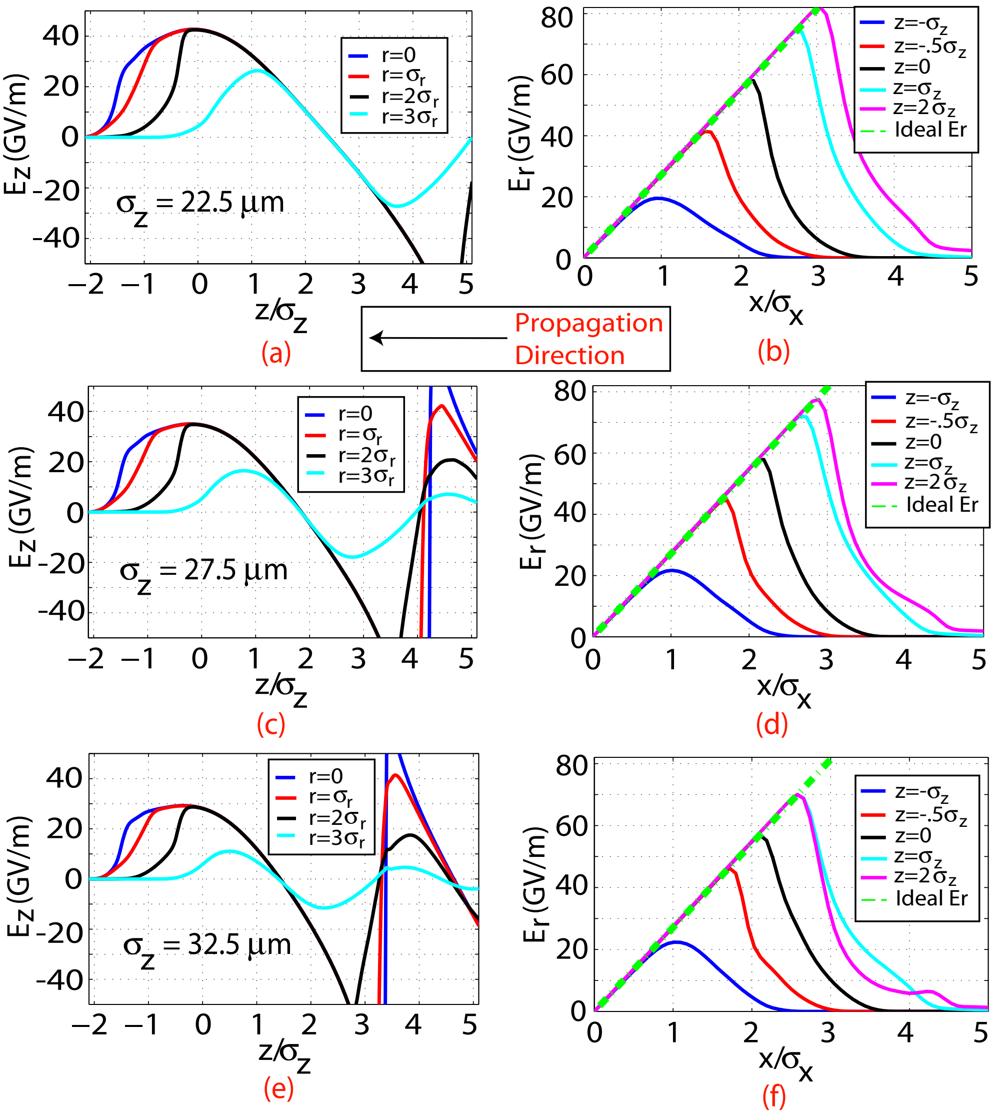

Figure 7.2: Plots the longitudinal and transverse fields in a field ionized plasma of density $n_{pe} = 2 \times 10^{17} cm^{-3}$ with a $N_b = 4 \times 10^{10}$ electron beam with $\sigma_r = 12\mu m$ and three different σ_z values. (a) Longitudinal fields for $\sigma_z = 22.5$. (b) Transverse fields for $\sigma_z = 22.5$. (c) Longitudinal fields for $\sigma_z = 27.5$. (d) Transverse fields for $\sigma_z = 27.5$. (e) Longitudinal fields for $\sigma_z = 32.5$. (f) Transverse fields for $\sigma_z = 32.5$.

ion column where the pure ion column exists at longitudinal positions where $z > \sigma_z$. However, the two problems that exist are the significant energy loss to the wake of $E_{z,peak} = 42.7$ GeV/m, and the fact that almost all electrons in the ion column are in the energy loss region. The wake passes from a decelerating field to an accelerating field at $z \approx 2.5\sigma_z$. Thus, there is too much energy loss in this case to design a 1 m long plasma source. A 28.5 GeV electron at $r = 15\mu m$ at $z = 0$ will radiate $\approx$ 4.3 GeV/m of synchrotron energy with a critical energy $E_c \approx 50$ MeV. However, we see that the same electron is in the peak energy loss region and will lose $E_{z,peak} \approx 43$ GeV/m to the wake. Also, the radiation energy loss and the E_c scale as γ_2. Thus, as the electron loses energy to the wake, the radiated energy and the critical energy of the X-ray spectrum decrease very quickly, leading to a small amount of MeV photons. The $\sigma_z = 32.5\mu m$ case of figures 7.2e and 7.2f still does not give a great result. Although electrons with $z > 1.5\sigma_z$ now reside in the accelerating and radiating portion of the ion column, many electrons are outside of the ion column since $r_{i,max} < 2.5\sigma_r$.

7.1.3 Plasma Density

The final wake dependence that is explored is the dependence on plasma density n_{pe}. The previous cases proved that $\sigma_r = 15\mu m$ is too large for a practical source, and that σ_z should be large to minimize $E_{z,peak}$. The plasma density plots of figure 7.3 shows the longitudinal and the transverse focusing fields of a 3-D Gaussian beam with $\sigma_r = 12\mu m$ and $\sigma_z = 35\mu m$ for four different plasma densities: $n_{pe} = 1 \times 10^{17} cm^{-3}$, $n_{pe} = 1.5 \times 10^{17} cm^{-3}$, $n_{pe} = 2 \times 10^{17} cm^{-3}$ and $n_{pe} = 3 \times 10^{17} cm^{-3}$. The longitudinal and transverse fields are plotted at the same positions as the previous two cases.

The scaling of $E_{z,peak}$ with n_{pe} is rather weak. Figure 7.3a, 7.3c, 7.3e and 7.3g have density values of $n_{pe} = 1 \times 10^{17} cm^{-3}$, $n_{pe} = 1.5 \times 10^{17} cm^{-3}$, $n_{pe} = 2 \times 10^{17} cm^{-3}$ and $n_{pe} = 3 \times 10^{17} cm^{-3}$, respectively. These cases have $E_{z,peak}$ values of 21 GeV/m, 23.5 GeV/m, 25.1 GeV/m and 27.2 GeV/m, respectively. This gives a scaling of $E_{z,peak} \propto \sqrt[4]{n_{pe}}$.

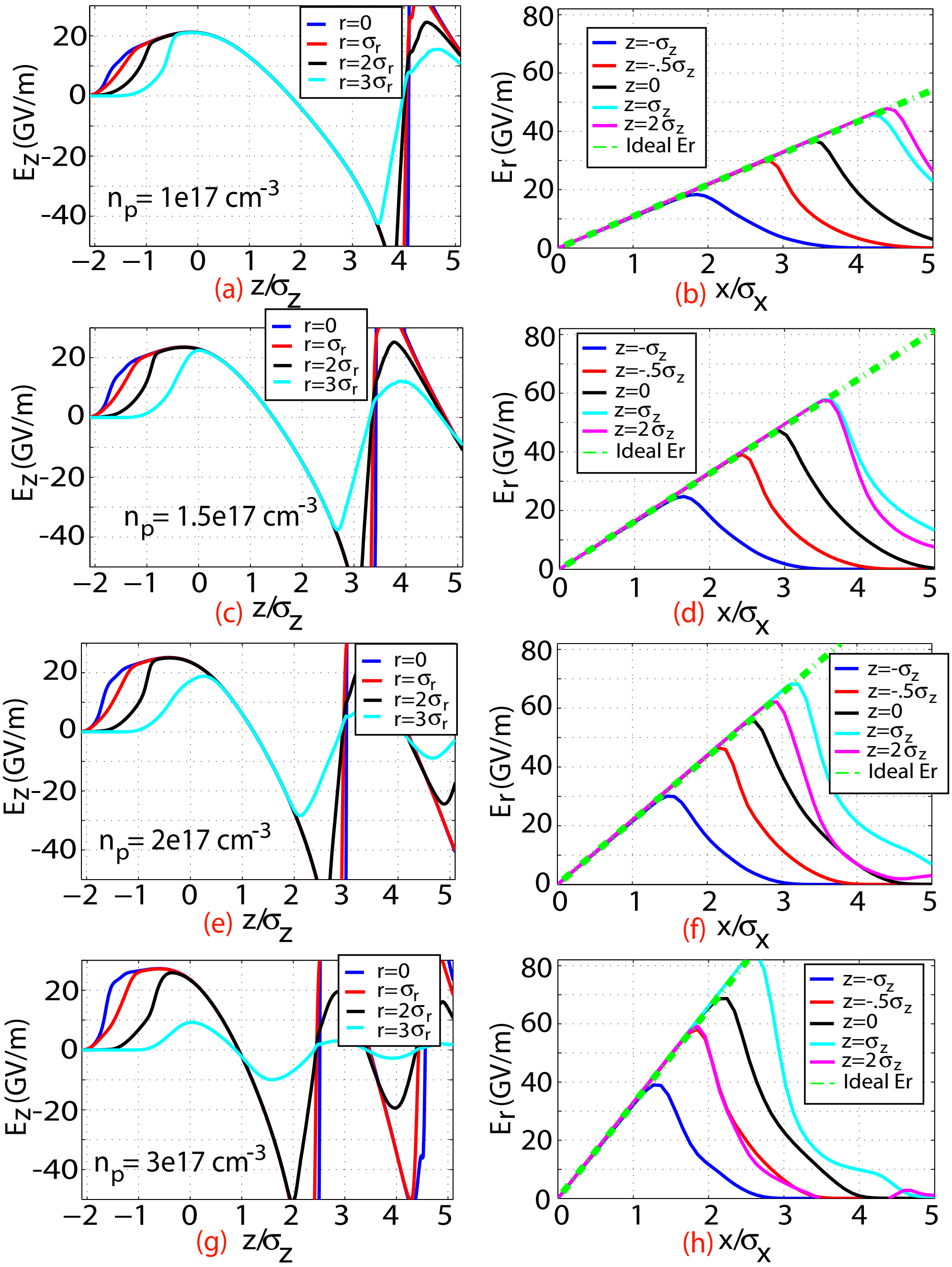

Figure 7.3: Plots the longitudinal and transverse fields in a field ionized with four different n_{pe} values with a $N_b = 4 \times 10^{10}$ electron beam with $\sigma_r = 12\mu m$ and $\sigma_z = 35\mu m$ values. (a) Longitudinal fields for $n_{pe} = 1 \times 10^{17} cm^{-3}$. (b) Transverse fields for $n_{pe} = 1 \times 10^{17} cm^{-3}$. (c) Longitudinal fields for $n_{pe} = 1.5 \times 10^{17} cm^{-3}$. (d) Transverse fields for $n_{pe} = 1.5 \times 10^{17} cm^{-3}$. (e) Longitudinal fields for $n_{pe} = 2 \times 10^{17} cm^{-3}$. (f) Transverse fields for $n_{pe} = 2 \times 10^{17} cm^{-3}$. (g) Longitudinal fields for $n_{pe} = 3 \times 10^{17} cm^{-3}$. (h) Transverse fields for $n_{pe} = 3 \times 10^{17} cm^{-3}$.

All density cases up to $n_{pe} = 3 \times 10^{17} cm^{-3}$ place a large portion of the $r = 3\sigma_r$ electrons in the pure ion column. For the $n_{pe} = 3 \times 10^{17} cm^{-3}$ case of figure 7.3h, we see that there are no $r = 3\sigma_r$ electrons in the ion column. However, for the $n_{pe} = 2 \times 10^{17} cm^{-3}$ case of figure 7.3f, all $r = 3\sigma_r$ electrons beyond $z = \sigma_z$ reside in the ion column. The $n_{pe} = 2 \times 10^{17} cm^{-3}$ seems to be ideal with the $\sigma_r = 12\mu m$ case shown here. However, this will not necessarily give the best positron yield. Recall from dW/dz that a $r = 8\mu m$ electron with $n_{pe} = 3 \times 10^{17} cm^{-3}$ is equivalent to a $r = 12\mu m$ electron with $n_{pe} = 3 \times 10^{17} cm^{-3}$. Furthermore, since $E_c \propto r$, the critical energy will be substantially lower for the $n_{pe} = 3 \times 10^{17} cm^{-3}$ case with $r = 8\mu m$. The average number of photons radiated per electron is found by dividing dW/dz by E_c. Thus, with E_c being lower, we have more photons being radiated. There is a concern that E_c will drop too low for a practical source since it is desired to have large amounts of 10-30 MeV photons. This is not an issue for our case since E_c for an $r = 8\mu m$ electron with $n_{pe} = 3 \times 10^{17} cm^{-3}$ is still $\sim 40MeV$.

There are two other reasons why the $n_{pe} = 3 \times 10^{17} cm^{-3}$ case is preferred. First, it is clear from figures 7.3e and 7.3g that $E_{z,peak}$ is 2 GeV higher for the $n_{pe} = 3 \times 10^{17} cm^{-3}$ case than for the $n_{pe} = 2 \times 10^{17} cm^{-3}$ case. However, the $n_{pe} = 3 \times 10^{17} cm^{-3}$ case is still better since $dW/dz \propto n_{pe}^2$ while $E_{z,peak} \propto \sqrt[4]{n_{pe}}$. Second, the ionization front for each case will have the same longitudinal position since ionization is purely a function of the beam electric field (see chapter 2). However, the smaller λ_p for the $n_{pe} = 3 \times 10^{17} cm^{-3}$ case will have two effects that will enhance the radiated X-ray energy. Since the wake is more longitudinally compact from the lower λ_p, the position of $E_{z,peak}$ has moved forward as seen in figure 7.3g. Thus, $E_{z,peak}$ in the $n_{pe} = 2 \times 10^{17} cm^{-3}$ case resides around $z = 0$, or the location where most electrons reside, but for the $n_{pe} = 3 \times 10^{17} cm^{-3}$ case, $E_{z,peak}$ resides closer to $z = -.75\sigma_z$, removing electrons from the peak energy loss region. Also, the shorter λ_p will bring more radiating electrons into the accelerating portion of the wake. The $n_{pe} = 2 \times 10^{17} cm^{-3}$ case of figure 7.3e transitions from a decelerating wake to an accelerating wake at $z \approx 1.2\sigma_z$. However, the $n_{pe} = 3 \times 10^{17} cm^{-3}$ case of figure 7.3g makes the transition to an accelerating wake at $z = .9\sigma_z$. For our 3-D Gaussian beam this places extra 7 percent of the total beam electrons in the

Parameter	*Scaling*
Radiation Energy Loss (dW/dz)	(γ^2 , n_{pe}^2 , r_β^2)
Critical Energy (E_c)	(γ^2 , n_{pe} , r_β)
Number of Photons ($[dw/dz]/E_c$)	(n_{pe} , r_β)
Maximum Ion Column Radius ($r_{i,max}$)	($\sqrt{N_b}$, $1/\sqrt{n_{pe}}$, $1/\sqrt{\sigma_z}$)
Peak Energy Loss ($E_{z,peak}$)	($\sqrt{N_b}$, $\sqrt{n_{pe}}$, $1/\sigma_z$)

Table 7.1: This table shows the scaling laws for various plasma parameters using a 3-D Gaussian electron beam in QuickPIC.

accelerating portion of the wake. It is true that for the $n_{pe} = 3 \times 10^{17} cm^{-3}$ case of figure 7.3g the ion column concludes at $r \approx 2.5\sigma_z$ whereas the $n_{pe} = 2 \times 10^{17} cm^{-3}$ case of figure 7.3e concludes at $r \approx 3\sigma_z$, removing electrons from the ion column for the $n_{pe} = 3 \times 10^{17} cm^{-3}$ case. This is however a welcomed trade, since 7 percent of the beam electrons reside in the longitudinal range of $z = (.9 - 1.2)\sigma_z$ while only 0.5 percent reside in the longitudinal range of $z = (2.5 - 3)\sigma_z$.

7.1.4 Scaling Laws

In table 7.1, we list the scaling laws derived from theoretical considerations of from QuickPIC simulations that take into account field ionization.. These are the parameters that need to be optimized for a source.

7.1.5 Experimental Observation of this Accelerating Effect

The technique of placing the radiating electrons in the accelerating portion of the wake will lead to X-ray and therefore positron yield enhancement. The question arises of why this enhancement was not observed in the experiment. The answer is simply that we were not set up to see this effect at the densities where data was taken. This fact is illustrated in Figure 7.4. Figure 7.4a plots the longitudinal fields at various radial positions for the $n_{pe} = 1 \times 10^{17} cm^{-3}$ case that was fit to experimental data in chapter 5. Figure 7.4b plots the transverse focusing fields at various longitudinal beam positions for the same case, and figure 7.4c plots the plasma density contours for this case. As stated in chapter 2, this case assumes a $\sigma_r = 11\mu m$, $\sigma_z = 22.5\mu m$ and $N_b = 1.2 \times 10^{10}$. It was matched to the data by matching the peak energy loss of the simulation with that experimentally measured on the Cherenkov diagnostic. Figures 7.4d, 7.4e and 7.4f plot the same variables described above for a $\sigma_r = 15\mu m$, $\sigma_z = 22.5\mu m$ and $n_{pe} = 2 \times 10^{17} cm^{-3}$ with $N_b = 4 \times 10^{10}$ case. For the $n_{pe} = 1 \times 10^{17} cm^{-3}$ case, the transition from a decelerating wake to an accelerating wake does not occur until $z \approx 2.3\sigma_z$ whereas the transition from a decelerating to accelerating wake in the $n_{pe} = 2 \times 10^{17} cm^{-3}$ case occurs at $z = 1.2\sigma_z$. This places about .1 percent of the total beam electrons in the accelerating portion of the ion column for the $n_{pe} = 1 \times 10^{17} cm^{-3}$ case while placing 11.4 percent of the total beam electrons in the accelerating portion of the wake for the $n_{pe} = 2 \times 10^{17} cm^{-3}$ case.

7.2 A Possible Source Design

From the above parameter discussion, we conclude that an "ideal" case would have parameters in the range of a 3-D Gaussian beam with $N_b = 4 \times 10^{10}$ electrons with $\sigma_r = 9\mu m$, $\sigma_z = 35\mu m$, and $n_{pe} = 3 \times 10^{17} cm^{-3}$. Figure 7.3h shows that a $\sigma_r = 9\mu m$ electron beam could be supported in the ion column driven in a plasma of this density with $\sigma_z = 35\mu m$. A schematic of such a source is shown in figure 7.5. The source uses a 1-m Cs plasma with a $0.5X_o$ W target that resides 2-m downstream from the exit of the plasma. This distance between the plasma exit and the target gives enough space for a dipole magnet to be installed that would deflect the electrons away from the target, eliminating critical thermal failure issues.

Three cases will be run at $n_{pe} = 3 \times 10^{17} cm^{-3}$ with the parameters listed above. The initial energy of the beam γ has little effect on the longitudinal and transverse dynamics in the plasma. Thus, we can use figure 7.3g for the three case with $E_{beam} = 30$ GeV, $E_{beam} = 40$ GeV and $E_{beam} = 50$ GeV. Figure 7.3g plots the wakeloss in each longitudinal portion of the electron beam. Thus, to achieve an

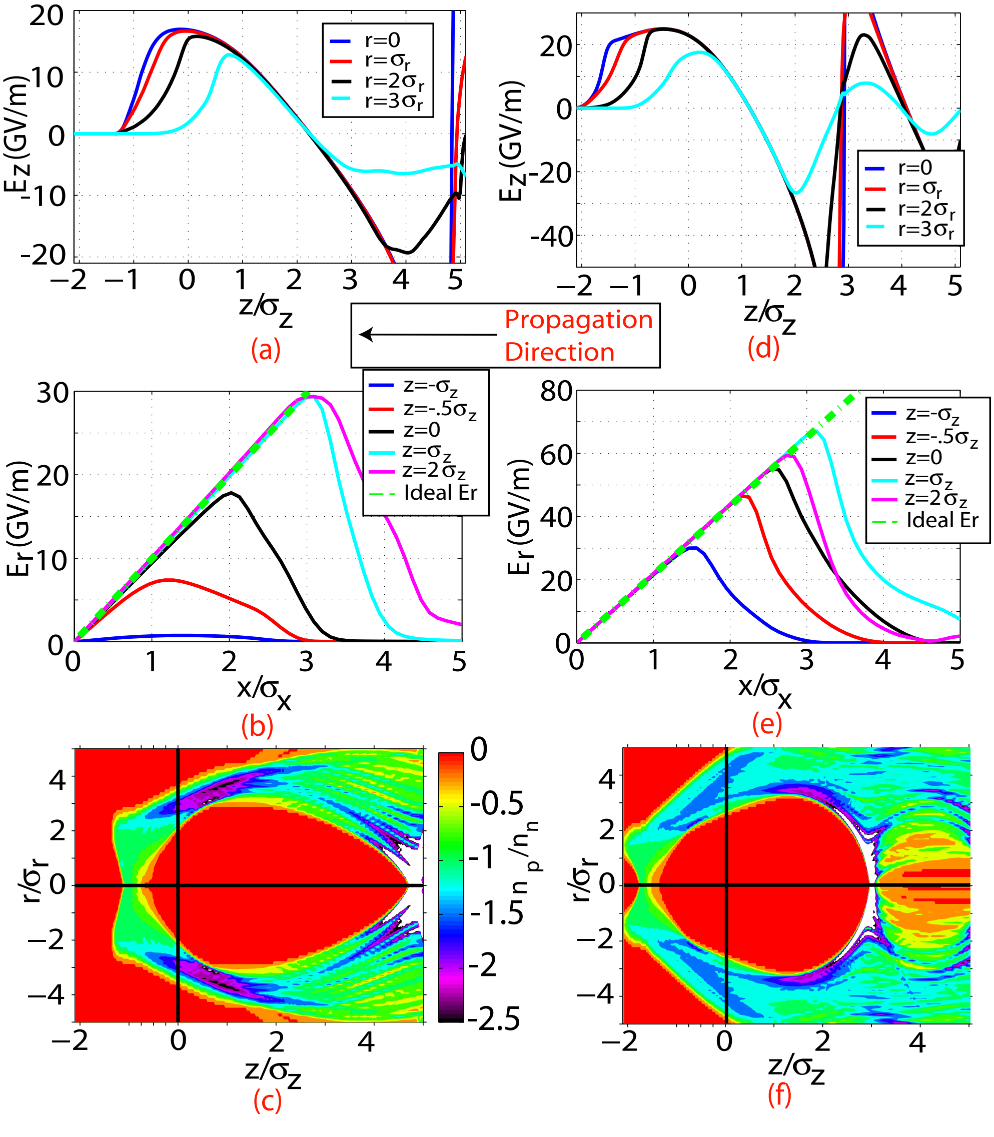

Figure 7.4: Plots the (a) longitudinal fields, (b) transverse fields and (c) plasma density contours for a plasma with $n_{pe} = 1 \times 10^{17} cm^{-3}$ and an electron beam with $N_b = 1.2 \times 10^{10}$, $\sigma_r = 11\mu m$ and $\sigma_z = 22.5\mu m$. Plots the (a) longitudinal fields, (b) transverse fields and (c) plasma density contours for a plasma with $n_{pe} = 2 \times 10^{17} cm^{-3}$ and an electron beam with $N_b = 4 \times 10^{10}$, $\sigma_r = 12\mu m$ and $\sigma_z = 35\mu m$.

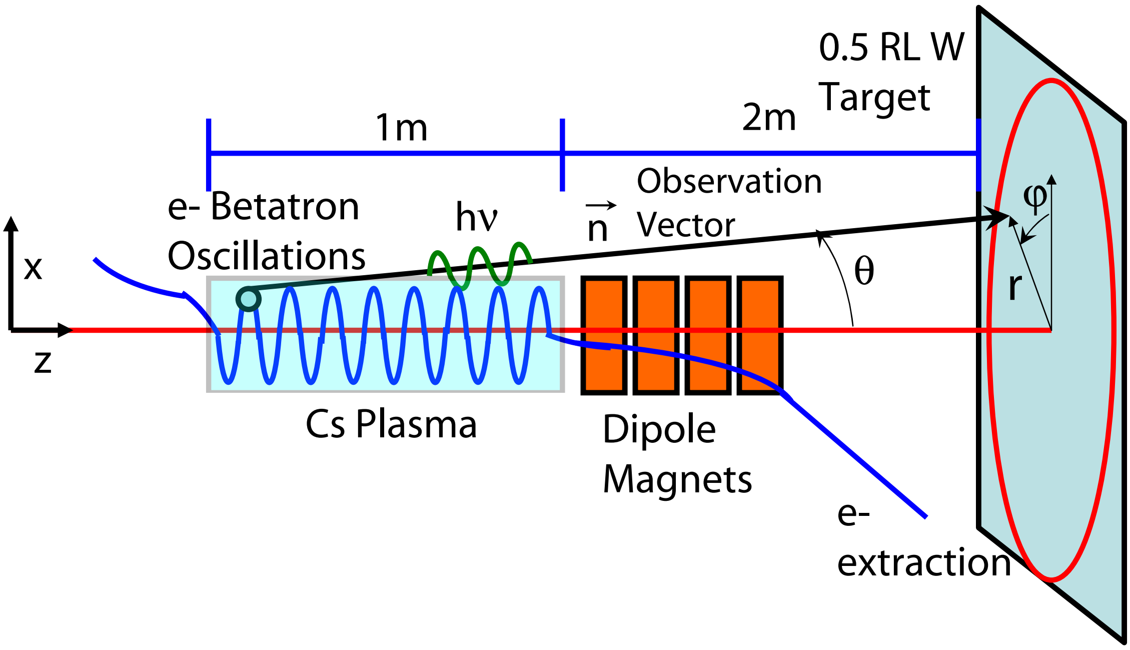

Figure 7.5: Schematic showing the proposed positron experiment.

accurate simulation, the Gaussian beam will be split into 5 longitudinal bins of width $dz = .5\sigma_z$. These bins will begin at $z = -\sigma_z$ since few electrons reside in an ion column upstream of this position. Within each bin, the number of electrons $N_{bi,x}$ will be computed from a 3-D Gaussian shape, and the wakeloss will be given by the average between the two edges of the bin. Table 7.2 gives the values for the 5 bins. The bin from $1 - 2\sigma_z$ is made into one bin to eliminate numerical integration errors that occur at high beam energies (i.e. $E_{beam} >\sim 70$ GeV). The bin with $z > 2\sigma_z$ is excluded because these electrons no longer reside in the ion column. Note that we can use the case from figures 7.3g and 7.3h since σ_r has little effect on the longitudinal wake, and it has no effect on the ion column radius. The results of the three source simulations are shown in figure 7.6. Figure 7.6a shows the yield for the three different E_{beam} cases for 1-50 MeV. The typical positron collection system will collect positrons up to 30 MeV. Thus, many of the 30-50 MeV positrons will be lost in a source with the current collection optics. Figure 7.6b plots the integrated positron yield for each E_{beam} case. It is clear that the $E_{beam} = 50$ GeV case gives the best yield at all energies. Table 7.3 gives the output values of the average electron

Bin	$N_{bi,x}$	Wakeloss (GeV/m)	$(r_{i,max}/\sigma_r)$
$(-1) - (-.5)\sigma_z$	5.99×10^9	27	2.1
$(-.5) - 0\sigma_z$	7.66×10^9	25	2.6
$0 - .5\sigma_z$	7.66×10^9	18	3.0
$.5 - 1\sigma_z$	5.99×10^9	7	3.0
$1 - 2\sigma_z$	5.40×10^9	-12.5	3.0

Table 7.2: This table gives the values for the 5 bins in our positron source calculation with a 3-D Gaussian beam with $N_b = 4 \times 10^{10}$ electrons with $\sigma_r = 9\mu m$, $\sigma_z = 35\mu m$ and $n_{pe} = 3 \times 10^{17} cm^{-3}$. Negative wakeloss is an accelerating field.

radiation ($\Delta\gamma$), the average photon energy and the average number of photons per beam electron for each individual longitudinal bin in the simulation. It is logical to assume that a small average photon energy of $\sim$ 20 MeV would be desired since this is the range where the positrons can be collected easily. However, this is not the case because the high E_{beam} case gives the largest yield at all energies. This is due to the e^+/e^- energy cross-section for pair production (see chapter 3). Table 7.3 also plots the average number of e^+/beam e^- for each case. This is the ultimate comparison used for positron sources. It is clear that the $E_{beam} = 30$ GeV and $E_{beam} = 40$ GeV cases have yields that are too low for a realistic linear collider application. However, the $E_{beam} = 50$ GeV case has promise, as it collects 0.23 e^+/beam e^- from 1-30 MeV and 0.44 e^+/beam e^- from 1-50 MeV. This result does not include the flux concentrator used in positron systems. This concentrator is a solenoid magnet that converts transverse momentum to longitudinal [6]. This generally adds about a factor of 3 to the yield. Thus, with the flux concentrator, the $E_{beam} = 50$ GeV positron source would theoretically collect about *0.69*e^+/beam e^- from 1-30 MeV and *1.32*e^+/beam e^- from 1-50 MeV. These are very respectable numbers that fall within the initial goal of 1-2 e^+/beam e^-.

It is clear from figure 7.6a that many positrons are created above the 50 MeV limit. If a system could be devised to collect these high energy positrons ($>$ 30 MeV) more efficiently, the yield would be increased substantially. A higher collection

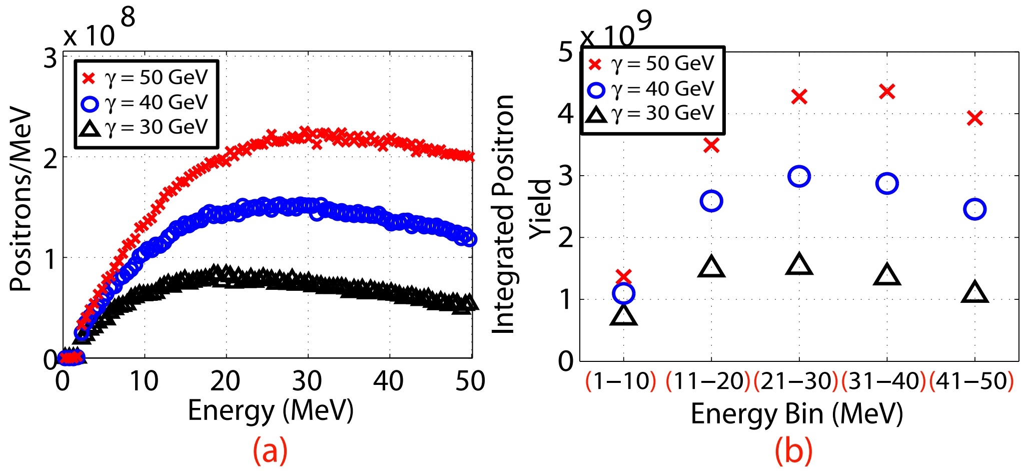

Figure 7.6: (a) The positron spectrum from 1-50 MeV for the three different initial beam energy cases of E_{beam} = 30 GeV, E_{beam} = 40 GeV and E_{beam} = 50 GeV. (b) The number of positrons within each 10-MeV energy bin for the same three E_{beam} values.

energy limit is not a possibility for a low-K magnetic undulator, since the undulator will not create many photons above 20 MeV [7].

Another important scaling law to consider is with n_{pe}. The energy loss to synchrotron radiation scales as n_{pe}^2, γ^2 and r_β^2. However, at a lower n_{pe}, the ion column is larger and $E_{z,peak}$ decreases. Table 7.4 gives the 6 bin values for a $n_{pe} = 2 \times 10^{17} cm^{-3}$ case with the $E_{beam} = 50 GeV$ and $\sigma_r = 9 \mu m$ as before. The results of the simulation as compared to the E_{beam} = 50 GeV case with $n_{pe} = 3 \times 10^{17} cm^{-3}$ are shown in figure 7.7. It is clear that again the $n_{pe} = 3 \times 10^{17} cm^{-3}$ case with E_{beam} = 50 GeV is superior at all energies. This is expected since within this regime the ion column increase scales as $1/\sqrt{n_{pe}}$ and $E_{z,peak} \propto 1/\sqrt[4]{n_{pe}}$. These scaling laws are far less than the n_{pe}^2 scaling of synchrotron radiation from betatron motion. Table 7.5 lists the output from both cases. Even though it is less, the $n_{pe} = 2 \times 10^{17} cm^{-3}$ case still gives impressive numbers.

Another important issue to note is the radiated energy lost due to the $\theta = K/\gamma$ divergence of the photon beam. Since this assumes the SLAC collection design downstream of the target, the photon beam can only be 2mm in radius. However, at these densities and energies, the actual beam is about 7-10mm in radius. When the total radiated power is compared with the radiated power within the 2mm

Beam Energy (GeV)	30	40	50
Average e^- Energy Loss (MeV)	935.4	2023	3343
Average Photon Energy (MeV)	14.2	22.9	34.9
Photons/Beam e^-	65.8	88.2	95.9
e^+/Beam e^- (1-30 MeV)	.09	.17	**.23**
e^+/Beam e^- (1-50 MeV)	.15	.30	**.44**

Table 7.3: This table gives the output from the simulation considering three different beam energies of $E_{beam} = 30$ GeV, $E_{beam} = 40$ GeV and $E_{beam} = 50$ GeV. All cases assume a 3-D Gaussian beam with $N_b = 4 \times 10^{10}$ electrons with $\sigma_r = 9\mu m$, $\sigma_z = 35\mu m$ and $n_{pe} = 3 \times 10^{17} cm^{-3}$.

Bin	$N_{bi,x}$	$Wakeloss (GeV/m)$	$IonColumnRadius$ (r_i/σ_r)
$(-1) - (-.5)\sigma_z$	5.99×10^9	24	2.1
$(-.5) - 0\sigma_z$	7.66×10^9	25	3.0
$0 - .5\sigma_z$	7.66×10^9	18	3.0
$.5 - 1\sigma_z$	5.99×10^9	12.5	3.0
$1 - 1.5\sigma_z$	3.67×10^9	-2	3.0
$1.5 - 2.5\sigma_z$	2.42×10^9	-15	3.0

Table 7.4: This table gives the values for the 6 bins in our positron source calculation with a 3-D Gaussian beam with $N_b = 4 \times 10^{10}$ electrons with $\sigma_r = 9\mu m$, $\sigma_z = 35\mu m$ and $n_{pe} = 2 \times 10^{17} cm^{-3}$. Negative wakeloss is an accelerating field.

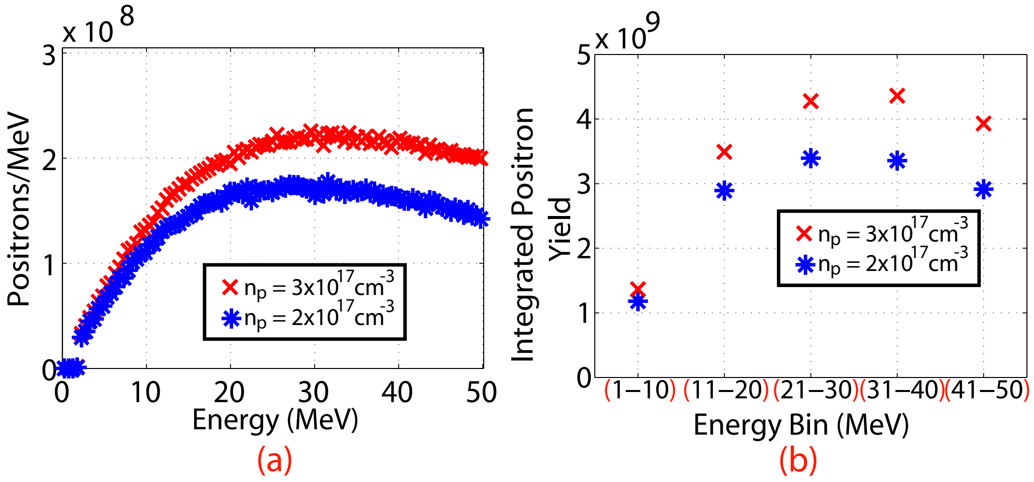

Figure 7.7: (a) The positron spectrum from 1-50 MeV for the densities $n_{pe} = 2 \times 10^{17} cm^{-3}$ and $n_{pe} = 3 \times 10^{17} cm^{-3}$ with an initial beam energy cases of $E_{beam} = 50$ GeV. (b) The number of positrons within each 10-MeV energy bin for the same two densities.

Density cm^{-3}	2×10^{17}	3×10^{17}
Average e^- Energy Loss (MeV)	2325	3343
Average Photon Energy (MeV)	27.8	34.9
Photons/Beam e^-	65.8	83.8
e^+/Beam e^- (1-30 MeV)	.19	**.23**
e^+/Beam e^- (1-50 MeV)	.34	**.44**

Table 7.5: This table gives the output from the simulation for the densities $n_{pe} = 2 \times 10^{17} cm^{-3}$ and $n_{pe} = 3 \times 10^{17} cm^{-3}$ with an initial beam energy cases of $E_{beam} = 50$ GeV. All cases assume a 3-D Gaussian beam with $N_b = 4 \times 10^{10}$ electrons with $\sigma_r = 9 \mu m$, $\sigma_z = 35 \mu m$.

acceptance radius, the total power is $\sim 2-3$ times larger than that accepted. This means that if one could accept a larger source diameter this would increase the positron yield.

7.3 Conclusion

In this chapter, we have considered a range of beam and plasma parameters to increase the positron yield in future experiments. Using densities that have been experimentally demonstrated with the current SLAC collection optics, about 1.3 e^+/ beam e^- could be collected with a 1-m long Cs plasma with $n_{pe} = 3 \times 10^{17} cm^{-3}$, $N_b = 4 \times 10^{10}$, $E_{beam} = 50$ GeV, $\sigma_r = 9\mu m$ and $\sigma_z = 35\mu m$. This is a respectable number and gives incentive to further explore this source design. All of the above parameters have assumed a constrained collection system. Thus, with a larger radial collection system, the full benefit of the high-K wiggler could be realized.

CHAPTER 8

Conclusion

A new method for generating positrons has been proposed using betatron X-rays emitted by a high-K plasma wiggler. The plasma wiggler is an ion column produced by the head of the beam when the peak beam density exceeds the plasma density. The radial electric field of the beam blows out the plasma electrons, transversely, creating an ion column. The focusing electric field of the ion column, in turn, causes the beam electrons to execute betatron oscillations about the axis of the ion column. This betatron motion can give rise to synchrotron radiation in the 1-50 MeV range, if the beam energy and the plasma density are high enough. A significant amount of electron energy can be lost to radiated X-ray photons. These photons strike a thin ($.5X_o$), high-Z target and create e^+/e^- pairs.

The thesis began by deriving the equations for betatron emission from electrons oscillating in an ion column. Two methods were explored. The first involved solving the Lienard-Wiechert potentials using the betatron trajectories and computing the X-ray spectrum in the far-field. However, it was found that because of the harmonic structure in the X-ray spectrum, this method was impractical for computing the X-ray spectrum emitted by the electrons using a single processor for the plasma densities of interest (i.e. $\sim 10^{17} cm^{-3}$). Thus, the saddle-point method was utilized. The saddle-points of the electron trajectory are defined as being near the location of maximum off-axis displacement and minimum radius of curvature. For a given wavelength, there are two saddle-points, and it is at these locations that most of the synchrotron radiation is emitted. Thus, by Taylor-expanding around these locations along the betatron trajectory, the X-ray spectrum can be computed with relative ease.

The theory of radiation emission was followed by the theory of positron production within a solid target. At first glance, it may appear that the broadband photon source created by a high-K plasma wiggler would not be best suited for a positron source where 1-30 MeV positrons are desired. However, the pair production cross-sections and the energy distributions of the created pairs show that a broadband source with the proper plasma density and collection system design can enhance the positron yield relative to the narrow-band low-K magnetic undulator positron sources that have been proposed.

This method of positron production was explored experimentally using the ultra-short electron bunches ($\sim 25\mu m$) available at the Final Focus Test Beam (FFTB) at the Stanford Linear Accelerator Center (SLAC). Since the UV energy required to photo-ionize a uniform $n_p > 1 \times 10^{17} cm^{-3}$ plasma column was impractical with current excimer lasers, field ionization was used to ionize the Li vapor. The ultra-short electron bunches had radial electric fields that exceeded the 6 GV/m field ionization threshold of Li. Field ionization gives the additional advantage of a self-guided electron beam within the plasma, eliminating difficult alignment issues that were encountered in previous experiments with lower plasma densities and longer bunch lengths.

After propagating through the plasma, the electrons were sent through an imaging system and dispersed in energy using a magnetic spectrometer. This spectrometer also separated the beam electrons from the betatron X-ray photon beam. The betatron X-rays were propagated 40 m downstream of the plasma, collimated with two Tungsten (W) collimators, and collided with a 1.7 mm ($.5X_0$) thick W target to produce e^+/e^- pairs. The resulting pairs were imaged up to an energy of 30 MeV in a magnetic spectrometer. The positrons and electrons were detected using 1mm Silicon Surface Barrier detectors (SBDs) with effective surface areas of 49 mm^2. Although the majority of data was taken with positrons, the magnet polarity was switched at one point to verify that the electron spectrum was similar as would be expected from pair production in a convertor target.

It was determined that there are three important parameters that effect the X-ray photon yield and thus the positron yield. These variables are the number of beam electrons radiating in the ion column (N_{bi}), the energy of the radiating electrons (γ_b), and the rms size of the electron beam ($\sigma_{i:x,y}$) when it is radiating in the peak density region of the plasma. The values of these three parameters are different when the plasma is present compared to their values when the beam propagates in vacuum. The first two variables were measured using the 16-bit images from the Cherenkov diagnostic that measured the energy spectrum of the electrons leaving the plasma column. By measuring the number of electrons that lost energy, N_{bi} could be determined, and by computing the average energy of those electrons, the average beam energy (γ_b) could be computed. The lithium plasma column has approximately Gaussian density ramps on either side of the uniform density region in the center. Since the ramped plasma density profile focuses the electron beam down to $\sigma_{i:x,y}$ before the peak density region of the plasma where it radiates the majority of its synchrotron energy, a beam envelope model was implemented using the vacuum electron beam sizes and emittances measured during the experiment. These three parameters were used to compare the experimentally measured yields with a computational model that was developed using the saddle-point method described above in tandem with the Electron-Gamma-Shower4 Code (EGS4) which tracks the interactions of particles and photons in matter. The agreement was excellent for the three densities of interest. The positron yield as a function of CTR energy (which is proportional to the inverse of the bunch length) and plasma length were also measured. Each giving results that were in good agreement with theory.

Since the experiments were performed in a parameter range that was optimized for the Plasma Wakefield Accelerator experiment (where the electron beam σ_z was approximately half the plasma wavelength), it was found that at the highest densities (where this condition was satisfied) there was a significant loss of beam energy to the wakefield. Therefore, in chapter 7, we have designed a positron experiment with beam and plasma parameters specifically optimized for maximizing the positron yield. It is found that a Gaussian beam of 4×10^{10} electrons with $\sigma_r = 9\mu m$ and $\sigma_z = 35\mu m$ and energies of 50 GeV propagating through a 1 m Cs plasma of density $3\times10^{17} cm^{-3}$ will give an average of about $0.44e^+$/ beam e^- with energies in the range of 1-50 MeV. With the aid of the current SLAC flux concentrator, the calculated yield would probably be tripled to $1.32e^+$/ beam e^-. This is a highly respectable number that compares favorably to the current low-K magnetic wiggler designs.

References

[1] H.A. Olsen J.W. Motz and H.W. Koch. "Pair Production by Photons." *Rev. Mod. Phys.*, **41**:581–639, 1969.

[2] H. Bethe. *Proc. Cambridge Phil. Soc.*, **30**:524, 1934.

[3] C.D. Barnes. *Longitudinal Phase-Space Measurements and Application to Beam-Plasma Physics.* Stanford University, 2006.

[4] C.L. O'Connell. *Plasma Prioduction Via Field Ionization.* Ph.D Thesis, Stanford University, 2005.

[5] H. Wiedemann. *Undulator and Wiggler Radiation, edited by Chao and Tigner in Handbook of Accelerator Physics and Engineering.* World Scientific Publishing Co. Pte. Ltd., 1998.

[6] S. Ecklund. "SLAC Linear Collider Design Handbook." *Stanford Linear Accelerator Center, SLAC-TN-714*, 1984.

[7] K. Flottmann. *Conversion of Undulator Radiation, edited by Chao and Tigner in Handbook of Accelerator Physics and Engineering.* World Scientific Publishing Co. Pte. Ltd., 1998.

[8] E-166 collaboration. "Undulator Based Production of Polarized Positrons: A Proposal for the 50 GeV Beam in the FFTB." *Stanford Linear Accelerator Center, SLAC-TN-04-018*, 2003.

[9] J. Frisch. "Design Considerations for a Compton Backscattering Positron Source." In *1997 Proceedings of the Workshop on New Kinds of Positron Sources for Linear Colliders*, 1997.

[10] T. Takahashi. "Positron Production in Single Crystals by 1.2 GeV Channeling Electrons." In *1997 Proceedings of the Workshop on New Kinds of Positron Sources for Linear Colliders*, 1997.

[11] S. Wang *et al.* "X-ray Emission from Betatron Motion in a Plasma Wiggler." *Phys. Rev. Lett.*, **88**:135004, 2002.

[12] C. Huang. In *Advanced Accelerator Concepts: Eleventh Workshop*, pp. 433–439, 2004.

[13] E. Esarey et al. "Synchrotron Radiation from Electron Beams in Plasma Focusing Channels." *Phys. Rev. E*, **65**:056505, 2002.

[14] G.I. Budker. In *Proceedings of the CERN Symposium on Hugh Energy Accelerators and Pion Physics*, pp. 68–75, 1956.

[15] J.D. Jackson. *Classical Electrodynamics, 3rd Edition.* John Wiley and Sons, Inc., 1999.

[16] I. Kostyukov et al. “X-ray Generation in an Ion Channel.” *Phys. Plasmas*, **10**:4818–4828, 2003.

[17] M.V. Ammosov N.B. Delone and V.P. Krainov. “Tunnel Ionization of Complex Atoms and of Atomic Ions in an Alternating Electric Field.” *Sov. Phys. JETP*, **64**:1191–1194, 1986.

[18] D.L. Bruhwiler et. al. “Particle-In-Cell Simulations of Tunnel Ionization Effects in Plasma Wakefield Accelerators.” *Phys. Plasmas*, **1**:2022, 2003.

[19] K.Bane and P.Emma. “Litrack: A Fast Longitudinal Phase Space Tracking Code with Graphicl User Interface.” In *In Proceedings of the 2005 Particle Accelerator Conference*, 2005.

[20] M. J. Hogan et al. “Multi-GeV Energy Gain in a Plasma Wakefield Accelerator.” *Phys. Rev. Lett.*, **95**:054802, 2005.

[21] D. Griffiths. *Introduction to Quantum Mechanics.* Prentice Hall, 1995.

[22] M. Thornton. *Classical Dynamics of Particles and Systems, 4th Edition.* Saunders College Publishing, 1995.

[23] J.D. Bjorken and S.D. Drell. *Relativistic Quantum Mechanics.* McGraw-Hill, Inc., 1964.

[24] T. Das. *Relativistic Quantum Mechanics of Electrons.* Harper and Row, Publishers, Inc., 1973.

[25] W. Heitler. *The Quantum Theory of Radiation, 3rd Edition.* Oxford University Press, 1954.

[26] B. Rossi. *High-Energy Particles.* Prentice-Hall, Inc., 1952.

[27] H. Bethe and W. Heitler. *Proc. Roy. Soc.*, **146**:83, 1943.

[28] J.C. Butcher and H. Messel. *Nucl. Phy.*, **20**:15, 1960.

[29] C. Joshi *et al.* “High Energy Density Plasma Science with an Ultra-Relativistic Electron Beam.” *Phys. Plasmas*, **9**:1845, 2002.

[30] P. Muggli et al. “Photo-Ionized Lithium Source for Plasma Accelerator Applications.” *IEEE Trans. Plas. Sci.*, **27**:791–799, 1999.

[31] J. Seeman et al. “SLC Energy Spectrum Monitor Using Synchrotron Radiation.” *SLAC-PUB-3945*, 1986.

[32] R. Carr and H. Wiedemann. *Other Radiation Sources, edited by Chao and Tigner in Handbook of Accelerator Physics and Engineering.* World Scientific Publishing Co. Pte. Ltd., 1998.

[33] P. Kung et al. “Generation and Measurement of 50-fs (rms) Electron Pulses.” *Phys. Rev. Lett.*, **73**:967–970, 1994.

[34] P. Muggli et al. “Coherent Transition Radiation to Measure the Slac Electron Bunch Length.” In *In Proceedings of the 2005 Particle Accelerator Conference*, 2005.

[35] R. Ischebeck et al. “Bunch Length Measurements Using Coherent Transition Radiation.” In *In Proceedings of the 2005 Particle Accelerator Conference*, 2005.

[36] C.R. Vidal. “Heat-Pipe Oven: A New, Well-Defined Metal Vapor Device for Spectroscopic Measurements.” *Journal of Applied Physics*, **40**:3370, 1969.

[37] C.B. Alcock. “Vapor Pressure Equations for the Metallic Elements: 298-2500K.” *Canadian Metallurgical Quarterly*, **23**:309, 1994.

[38] W. Lu et. al. “Limits of Linear Plasma Wakefield Theory for Electron or Positron Beams.” *Phys. Plasmas*, **12**:063101, 2005.

[39] K.A.Marsh *et al.* “Beam Matching to a Plasma Wakefield Accelerator Using a Ramped Density Profile at the Plasma Boundary.” In *In Proceedings of the 2005 Particle Accelerator Conference*, 2005.